

Washington University in St. Louis
Washington University Open Scholarship

Engineering and Applied Science Theses &
Dissertations

McKelvey School of Engineering

Summer 8-15-2017

Studies in Pressurized Oxy-Combustion: Process Development and Control of Radiative Heat Transfer

Akshay Gopan

Washington University in St. Louis

Follow this and additional works at: https://openscholarship.wustl.edu/eng_etds



Part of the [Chemical Engineering Commons](#), and the [Oil, Gas, and Energy Commons](#)

Recommended Citation

Gopan, Akshay, "Studies in Pressurized Oxy-Combustion: Process Development and Control of Radiative Heat Transfer" (2017). *Engineering and Applied Science Theses & Dissertations*. 313.
https://openscholarship.wustl.edu/eng_etds/313

This Dissertation is brought to you for free and open access by the McKelvey School of Engineering at Washington University Open Scholarship. It has been accepted for inclusion in Engineering and Applied Science Theses & Dissertations by an authorized administrator of Washington University Open Scholarship. For more information, please contact digital@wumail.wustl.edu.

WASHINGTON UNIVERSITY IN ST. LOUIS

School of Engineering & Applied Science

Department of Energy, Environmental, and Chemical Engineering

Dissertation Examination Committee:

Richard L. Axelbaum, Chair

Pratim Biswas

Benjamin M. Kumfer

Jeffrey N. Phillips

Patricia Weisensee

Brent Williams

Ligang Zheng

Studies in Pressurized Oxy-Combustion:

Process Development and Control of Radiative Heat Transfer

By

Akshay Gopan

A dissertation presented to
The Graduate School
of Washington University in
partial fulfillment of the
requirements for the degree
of Doctor of Philosophy

August 2017
St. Louis, Missouri

© 2017, Akshay Gopan

Table of Contents

List of Figures	vi
List of Tables	x
Acknowledgments	xi
Abstract of the Dissertation	xv
Chapter 1 Introduction	1
1.1 World Fossil Energy Scenario	1
1.2 Carbon Dioxide: Capture, Utilization, and Sequestration	3
1.3 Oxy-Combustion.....	5
1.4 Pressurized Oxy-Combustion	10
1.5 Reducing Flue Gas Recycle in Oxy-Combustion	12
1.6 Scope of the Dissertation	13
Chapter 2 Staged, Pressurized Oxy-Combustion	15
2.1 Introduction.....	15
2.2 Process Summary	16
2.2.1 Fuel-staged oxy-combustion	16
2.2.2 Process description	18
2.3 Modeling Approach and Key Assumptions	20
2.3.1 Operating pressure.....	23
2.3.2 Radiant and convective heat exchanger	24
2.3.3 Direct contact column (DCC) and integrated pollutant removal	24
2.3.4 CO ₂ purification unit (CPU).....	27
2.3.5 Other considerations.....	28
2.4 Results and Discussions of Process Modeling	30
2.4.1 Auxiliary load comparison	33
2.4.2 Heat integration and net plant efficiency	33
2.4.3 Efficiency improvements breakdown.....	34
2.5 Economic Analysis	35
2.6 Conclusions.....	37

Chapter 3 Parametric Analysis of Staged, Pressurized Oxy-Combustion	39
3.1 Introduction.....	39
3.2 Operating Pressure	41
3.3 Fuel Moisture Content	47
3.4 Flue Gas Recycle Ratio.....	51
3.5 Process Intensification and Advanced Rankine Cycles	52
3.6 Conclusions.....	55
Chapter 4 Introduction to Burner and Boiler Design for Low-Recycle Pressurized Oxy-Combustion.....	57
4.1 Introduction.....	57
4.2 Boiler Design Considerations	58
4.2.1 Radiative trapping	62
4.3 Burner and Boiler Constraints	65
4.4 Conclusions.....	67
Chapter 5 Burner Design and the Effect of Mixing.....	68
5.1 Introduction.....	68
5.2 Process Modification—Reduction in the Number of Stages	68
5.3 Burner Design	70
5.4 CFD Methods.....	74
5.5 Results and Discussion	75
5.5.1 Low-recycle SPOC boiler—base design.....	75
5.5.2 Parametric study of important design parameters	79
5.6 Conclusions.....	87
Chapter 6 Operational Flexibility of SPOC Boilers	88
6.1 Introduction.....	88
6.2 CFD Methods and Simulation Conditions.....	90
6.3 Effect of Turndown.....	91
6.4 Modified Boiler Design	93
6.4.1 Wall rings	94
6.4.2 Larger boiler diameter with wall-rings.....	98
6.5 Conclusions.....	102

Chapter 7 Soot in Tri-axial Flames	104
7.1 Introduction.....	104
7.2 Soot inception limits—C/O Ratio and Kinetic Temperature Limits.	105
7.3 Tri-axial Burke-Schumann Flame Model	107
7.4 Comparison of Normal and Tri-axial Burke-Schumann Flame.....	113
7.5 Experimental Methods	115
7.6 Experimental Results	118
7.7 Conclusions.....	119
Chapter 8 Summary and Recommendations for Future Work.....	120
8.1 Process Development.....	121
8.2 Burner and Boiler Development	123
8.3 Recommendations for Future Works	125
References	127
Appendix A Computational Fluid Dynamics (CFD) Sub-Model Selection Criteria	145
Appendix B Effects of inert-placement (Z_{st}) on soot and radiative heat flux in turbulent diffusion flames	148
B.1 Introduction.....	150
B.2 Experimental Methods	153
B.2.1 Reactor	153
B.2.2 Experimental Conditions.....	155
B.2.3 Measurement Instruments	157
B.3 Results.....	160
B.4 Discussion.....	164
B.5 Conclusions.....	168
B.6 Acknowledgements.....	169
Appendix C Burke-Schumann Model Formulation for Tri-Axial Flames.....	170
Appendix D Effects of biomass moisture content on volatile flame length during co-firing with coal.....	175
D.1 Introduction.....	177
D.2 Experimental Methods	179
D.2.1 Reactor	179

D.2.2 Gas Sampling	180
D.2.3 Volatile Flame Length—Measurement Technique	181
D.2.4 Particle Sampling	183
D.3 Analytical Methods	184
D.4 Results and Discussion	186
D.4.1 Coal and biomass properties	186
D.4.2 Volatile Flame Length and Breakthrough	187
D.4.3 Analytical Results	190
D.5 Conclusions	192
D.6 Acknowledgements	193
Curriculum Vitae	194

List of Figures

Figure 1-1. Fuel share of world total primary energy supply for the year 2014. ¹ Peat and oil shale are aggregated with coal; ² Includes geothermal, solar, wind, heat, etc. Adapted from [4].	1
Figure 1-2. Energy use and per capita income of selected countries. Source: [5]	2
Figure 1-3. Schematic of an oxy-coal combustion power plant. Image source: Alstom	6
Figure 2-1. Depiction of the staged combustion concept.	18
Figure 2-2. Steam side process flow diagram for the SPOC process.	19
Figure 2-3. Gas side process flow diagram for the SPOC process.	19
Figure 2-4. Comparison of net plant efficiencies for various cases. (SC: Supercritical. Both SPOC cases are supercritical).	37
Figure 3-1. Percentage of flue gas moisture condensation at various DCC operating pressures and flue gas exit temperatures from the DCC	42
Figure 3-2. Increase in net plant efficiency (HHV) as a function of pressure over Case P1 (16 bar).	43
Figure 3-3. Increase in recoverable heat (integration into Rankine cycle) from (a) DCC, (b) oxygen production.	46
Figure 3-4. Change in net plant efficiency (HHV) as a function of as-fired fuel moisture. Reference is a fully dry fuel.	49
Figure 3-5. Effect of flue gas recycle ratio on the net plant efficiency (HHV) in the SPOC process	52
Figure 3-6. Net plant efficiencies when using different steam temperatures and pressures, and number of reheats in the Rankine cycle of the SPOC process.	55
Figure 4-1. A comparison of a swirl-stabilized and an axial jet flame of coal combusting in pure oxygen. Temperature contours in false colors are shown on the left, and the corresponding wall heat flux profiles are shown on the right. Figure reproduced from Xia et al. [80].	61
Figure 4-2. Temperature contours for a case with buoyancy (top) and a case without buoyancy (bottom).	62
Figure 4-3. Illustration of radiative trapping	63

Figure 5-1. Simplified process flow diagram for a three-stage SPOC power plant.	70
Figure 5-2. Geometry of the burner and the boiler.	71
Figure 5-3. First 20-meter axial profile of the mass-averaged mean velocity in the boiler.....	71
Figure 5-4. Possible flame shapes for a triaxial system with fuel in the annulus, and two oxidizer streams. Dark blue represents the flame resulting from the SO and red represents the flame resulting from the IO.....	77
Figure 5-5. Volatile reaction rate and temperature contours for the base case. Note: Only the first 30 m of the boiler shown.....	78
Figure 5-6. Radiative and total heat flux profile for the base case.	79
Figure 5-7. First 30 m of (a) axial velocity and (b) temperature contours for two lengths of the conical frustum (10m and 20m).	80
Figure 5-8. Wall heat flux profiles for the two conical frustum lengths shown in Fig. 5-7.	81
Figure 5-9. Temperature contours with optical thickness of 2.3 from the wall overlaid for different burner configurations. The red arrows indicate the flame lengths measured by volatile reaction rates.	83
Figure 5-10. Radiative heat flux profiles for different burner configurations.	84
Figure 5-11. Temperature contours for different SR_{IO} . The red arrows indicate the volatile flame lengths as determined by completion of volatile reactions.	85
Figure 5-12. Radiative heat flux profiles for different SR_{IO}	86
Figure 6-1. Schematic showing the comparison of electricity produced by renewable sources and the electricity demand. The difference—residual power—has to be generated by non-renewable source. Reproduced from [111].....	88
Figure 6-2. Geometry of the boiler and burner. Reproduced from Chapter 5.	90
Figure 6-3. Radiative and total heat flux for the base (100% thermal input) case and the turndown case (40% thermal input).	91
Figure 6-4. The first 30 m of the temperature contours for the base case (100% thermal input) and the turndown case (40% thermal input) with $\tau_w = 2.3$ contour overlaid.....	92
Figure 6-5. The first 30 m of the axial velocity contours for the base (100% thermal input) case and the turndown case (40% thermal input). Buoyancy induced internal recirculation shown using iso-contour for zero axial velocity.	92

Figure 6-6. Schematic of the modified boiler design with wall-rings added to increase effectiveness of advection.	94
Figure 6-7. The first 30 m of temperature and axial velocity contours for base case and the turndown case with rings.....	95
Figure 6-8. Comparison of wall heat flux for different thermal loads: (a) radiative and (b) total heat flux for the 100% thermal input case, and (c) radiative and (d) total heat flux for the 40% thermal input case.....	96
Figure 6-9. (a) Temperature and optical thickness profiles as functions of radial distance from the wall and (b) the temperature profile as a function of optical thickness from the wall at 7.5 downstream from the burner for the 100% thermal input cases with and without rings	98
Figure 6-10. The first 40 m of temperature and axial velocity contours for the 100% thermal input case with wall-rings and longer expansion.	99
Figure 6-11. The (a) radiative and (b) total heat flux profiles for the 100% thermal input case with wall-rings and a longer conical expansion.	100
Figure 6-12. The (a) radiative, and (b) total heat flux profiles for the 40% thermal input case with wall-rings and a longer conical expansion.	101
Figure 6-13. The first 40 m of temperature and axial velocity contours for the 40% thermal input case with wall-rings and longer expansion.	101
Figure 7-1. Schematic of (a) a normal flame and (b) a tri-axial flame. The red curves are shown as representatives of flames in the two configurations. Note: This is only a longitudinal section of an axi-symmetric system.	111
Figure 7-2. Comparison of (a) normal Burke-Schumann flame with (b) tri-axial Burke-Schumann flame. The region between the critical C/O limit and the low temperature limit marks the region for soot inception. Note: A 2D longitudinal section of an axisymmetric flame is shown here.....	114
Figure 7-3. Combustor and burner design.	116
Figure 7-4. Particle size distribution of soot—comparison of normal configuration and tri-axial configuration.....	118
Figure B-1. Combustor and burner design.....	154
Figure B-2. The effect of Z_{st} on the soot inception location and soot volume fraction at various axial locations, as seen from the luminosity of the flame. Red arrows mark soot inception location.	161

Figure B-3. Line of sight emissivity at various axial position for three different Z_{st} cases. Soot volume fraction is proportional to the emissivity.	162
Figure B-4. Radiant heat flux profiles for the three Z_{st} cases.	163
Figure B-5. Flame structure, i.e., species and temperature profiles in mixture fraction (Z) space at 0.05 m from the burner. The black and red arrow mark the locations of the low temperature and C/O ratio bounds for ring formation respectively. Between them is the shaded region where soot can form. Note: For $Z_{st} = 0.68$, the temperature limit is on the other side of the C/O limit, thus no soot can form.	166
Figure C-1. Schematic of the tri-axial burner configuration.....	170
Figure D-1. Schematic of the reactor.....	179
Figure D-2. Visual representation of the volatile flame: a) No volatile breakthrough: the end of the volatile flame is downstream of the end of volatile release. b) Volatile breakthrough: the end of the volatile flame is upstream of the end of the volatile release zone. Reproduced from [191].....	182
Figure D-3. Isokinetic particle sampling probe schematic.	183
Figure D-4. Fuel particle size distributions using sieves, and the mass-mean diameters calculated using Rosin-Rammler curve fit.	187
Figure D-5. Experimental CO ratio profiles (symbols) and curve fit (lines). Error bars show the maximum and minimum values for that port. The arrows denote the end of flame.	188
Figure D-6. Volatile content measured in particle samples taken immediately downstream of the volatile flame during the co-firing cases. Note: For the 20% moisture case, particles were sampled before the end of volatile flame.	190
Figure D-7. Characteristic times for biomass particle heating (t_p), divided into heat diffusion to the center (t_d) and heating of particle mass (t_h), and moisture vaporization (t_m).	191

List of Tables

Table 1-1. A representative oxy-coal combustion flue gas stream. Adapted from [42].....	9
Table 1-2. CO ₂ purity standards [42, 44].....	9
Table 2-1. Site conditions	21
Table 2-2. CO ₂ purity requirement for EOR and CO ₂ purity achieved with the SPOC process.....	22
Table 2-3. Key components data	22
Table 2-4. Reactions assumed for the direct contact column for SO ₂ and NO _x removal	25
Table 2-5. Properties of Wyodak/Anderson PRB sub-bituminous coal and Illinois #6 bituminous coal on an as-received basis [65].....	29
Table 2-6. Key process parameters [43, 66, 67]	30
Table 2-7. Flow rates and compositions at the outlet of each stage in the SPOC process firing PRB coal producing 550 MWe power.....	31
Table 2-8. Performance comparison of SPOC process (Case A and B) with relevant atmospheric pressure reference cases.....	32
Table 2-9. Global economic assumptions.....	36
Table 2-10. Financial structure	36
Table 3-1. Steam conditions for the various Rankine cycles considered	54
Table 5-1. Properties of Powder River Basin (PRB) coal	73
Table 5-2. CFD sub-models and some input parameters.....	75
Table 5-3. Velocities and geometries of the burner.....	82
Table 6-1. Coal properties and operating conditions.....	90
Table 7-1. Boundary conditions for the Burke-Schumann model.....	113
Table 7-2. Operating conditions for the two configurations.....	117
Table B-1. Operating condition parameters.....	157
Table D-1. Coal and biomass properties.....	186

Acknowledgments

First and foremost, I would like to thank my family for their constant and unconditional support and encouragement that helped me tremendously to pursue my dreams—both personal and professional.

I would like to sincerely thank Prof. Richard L. Axelbaum for guiding me through Ph.D. research. I appreciate his support, guidance, and more than anything confidence in me. He provided me with the means to study and explore the fascinating area of combustion engineering, while doing industrially relevant research. Working at the scales available to us has made me better appreciate the field of engineering research and the complexities associated with it. In the same breath, I have to thank Prof. Pratim Biswas for not just the encouragement and support he has provided, but also for being available to discuss my progress, and for trying to keep me on track with my publications.

I also wish to gratefully acknowledge Joerg Maier at the Institute for Combustion and Power Plant Technology (IFK), Univ. of Stuttgart, for inviting me to spend the first half of 2014 in his group working on ash deposition, fouling and slagging related topics. I learnt a lot from him and his research group, and have also made a number of friends. I would like to thank the entire KWF group at IFK for making me feel welcome and sharing your knowledge with me.

Of my committee members, I have worked with Drs. Benjamin Kumfer and Jeffrey Phillips for the entire duration of my Ph.D. They have always provided me with a lot of critical comments on my research, and have been extremely valuable in being available for bouncing new ideas. I would also like to thank Drs. Brent Williams, Patricia Weisensee, and Ligang Zheng for serving in my committee. Dr. Ligang Zheng's support and encouragement of my research over the years is

extremely valuable, especially since he is an expert and pioneer in the process modeling of pressurized oxy-combustion power plants.

I also would like to acknowledge the guidance and advise provided by the SPOC team outside WashU, especially Drs. Jeff Phillips and David Thimsen at EPRI. They helped make sure that my research was not an irrelevant exercise, but actually relevant to the industry that we were hoping to make an impact on. Recent interest from various companies in the technology has given me a sense of pride of the work that is in this dissertation.

In LACER lab, I would like to thank Dr. Zhiwei Yang for being a great mentor and teaching me CFD design. Apart from help in my research, he has been a great person to chat about non-research topics—everything from religion and politics to other things which are best left out of this document. I would surely miss the badminton games after work. I also want to thank Dr. Yi Fei for working with me and helping me during my research rotation at LACER. Drs. Fei Xia and Melissa Holtmeyer's encouragement in the early years of my Ph.D is also appreciated. The LACER lab members, previous and current, including Dr. Mikos Lengyel, Wendong, Adewale, Matt, Mike, Jose, Phillip, Dishant and Piyush, have been a really great team to work with.

I have also had the good fortune of having some of the best roommates here in St. Louis, starting with Drs. Bharat Suthar and Onkar Manjrekar. They are amazing people, who are always available to help—both personal and academic. I am really grateful for their support and friendship. I can't think of any person other than Bharat, with whom I have had discussions/arguments on the most wide-ranging topics. He has been a great teacher to me on numerical simulations and on some fascinating things he learnt in Dr. Carl Bender's class. Girish and Krishna, my new roommates are another set of people I am happy to have known. Krishna is one of the best cooks and a really nice

person in general. Girish has pushed me into exploring many new non-academic things for which I am grateful. They have made my stay quite pleasurable.

I would also like to thank Drs. Venkat Ramadesigan, Tandeep Chadda, and Ramesh Raliya for their encouragement. I also appreciate the random hangouts and discussions with many others, like Sameer, Shaline, Vivek, and Philip on research and beyond. I thank my friends in the EECE department for making graduate school an enjoyable experience. I would also like to thank the EECE staff, Rose Baxter, for the paperwork related to my graduate studies, Trisha Sutton, for helping with purchasing, Beth Mehringer, for reimbursements, Lesley Smith and Christine Tilley, for administrative help, and Irma Adams for everything related to my final defense.

I graciously acknowledge the funding agencies that helped me pursue this research. The work in the dissertation was supported by the U.S. Dept. of Energy, the Consortium for Clean Coal Utilization (CCCU) at Washington University, and the Wyoming Advanced Conversions Task Force.

I express my gratitude to Prof. Virendra Sethi, IIT Bombay who really pushed me towards a Ph.D. at WashU. I am glad I followed his advice. Finally, once again I wish to thank my parents and brother for their support throughout my life.

Akshay Gopan

Washington University in St. Louis,

August 2017

Dedicated to my family

*Just as the fire of knowledge liberates man from the shackles of ignorance,
The knowledge of fire throws open myriad potent means to power mankind's leap into the future.*

ABSTRACT OF THE DISSERTATION

Studies in Pressurized Oxy-Combustion:

Process Development and Control of Radiative Heat Transfer

by

Akshay Gopan

Doctor of Philosophy in Energy, Environmental, and Chemical Engineering

Washington University in St. Louis, 2017

Professor Richard L. Axelbaum, Chair

Fossil fuels supply over 80% of the world's primary energy and more than two-thirds of the world's electricity. Of this, coal alone accounts for over 41% of the electricity supplied globally. Though coal is globally well-distributed and can provide stable and reliable energy on demand, it emits a large amount of carbon dioxide—a greenhouse gas responsible for global warming. Serious concerns over the implication of the increased global temperature have prompted the investigation into low carbon energy alternatives. The idea of capturing the carbon dioxide emitted from the combustion sources is considered as one of the viable alternatives. This would allow the utilization of vast and widespread fuel resources (coal, oil, gas and biomass) that are capable of delivering power on demand, while mitigating the potentially harmful impact of CO₂.

Support for carbon capture, utilization and sequestration (CCUS) for power plants is, however, limited due to the high cost of electricity associated with the currently available technologies. The ultimate requirement of high pressure CO₂ for either sequestration or utilization has led to the investigation of pressurized oxy-combustion technologies. Since at higher pressure, the dew point of the flue gas is higher than at atmospheric pressure, pressurized oxy-combustion can be utilized

to extract the latent heat of condensation of the flue gas moisture, leading to an increase in plant efficiency.

A new staged, pressurized oxy-combustion (SPOC) process for power generation with carbon capture is presented in the first part of this dissertation. The proposed staged, pressurized oxy-combustion process not only extracts the latent heat of condensation of the flue gas moisture, but unlike first generation oxy-combustion or even other pressurized oxy-combustion processes, it also minimizes the recycle of flue gas. The net plant efficiency of this proposed process is more than 25% higher than that of first generation oxy-combustion. A detailed analysis of the capital and operating costs shows that the cost of electricity generated from this process would meet the U.S. Dept. of Energy target for power generation with carbon capture.

The design of a low-recycle oxy-combustion boiler is not trivial. A number of designs have been proposed, but were deemed unfit for the utility industry due to much higher heat flux than could be safely tolerated by the boiler tubes. In the second part of this dissertation, a new burner and boiler design is proposed that could be utilized in the low-recycle SPOC process. The proposed burner/boiler design 1) accommodates low flue gas recycle without exceeding wall heat flux limits, 2) increases the share of radiative over convective heat transfer in the boiler, 3) significantly reduces ash fouling and slagging, and 4) is flexible in that it is able to operate under various thermal loads. The proposed burner design would also lead to reduced soot, as compared to a normal burner. These aspects of the burner/boiler design are investigated in the dissertation.

Chapter 1

Introduction

1.1 World Fossil Energy Scenario

The global energy consumption is increasing every year, with increasing global population and the improvement in living conditions [1-3]. Combustion based sources—which includes fossil and biomass derived fuels—supply over 90% of the world’s primary energy (see Figure 1-1) [4, 5]. Even in electricity generation, combustion based sources play a dominant role, supplying more than two-thirds of the globally generated electricity [4]. Although these numbers will change over the years, thermal energy sources are still seen as being the dominant method of energy supply over the next several decades [5].

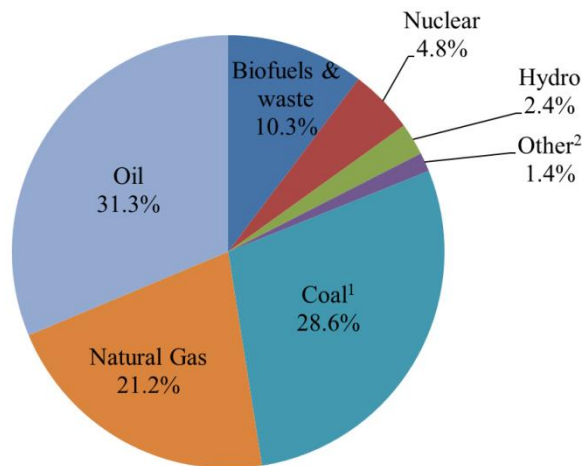


Figure 1-1. Fuel share of world total primary energy supply for the year 2014. ¹Peat and oil shale are aggregated with coal; ²Includes geothermal, solar, wind, heat, etc. Adapted from [4].

In the developing countries, like India and China, the per capita energy consumption is still much lower than in the developed world [5]. Significant population of these countries is currently energy impoverished. With the strive to end energy poverty [6], and a fast increasing GDP, the energy consumption of these countries is has been increasing significantly [5, 7-9], as can be seen in Figure 1-2. The primary energy source for both India and China is predominantly (> 90%) thermal energy based [6, 10]. Even with the pledge by these countries to limit the fossil fuel share of their total energy consumption [11, 12], the absolute amount of fossil fuel consumption is predicted to increase over the next several decades [5, 8-10].

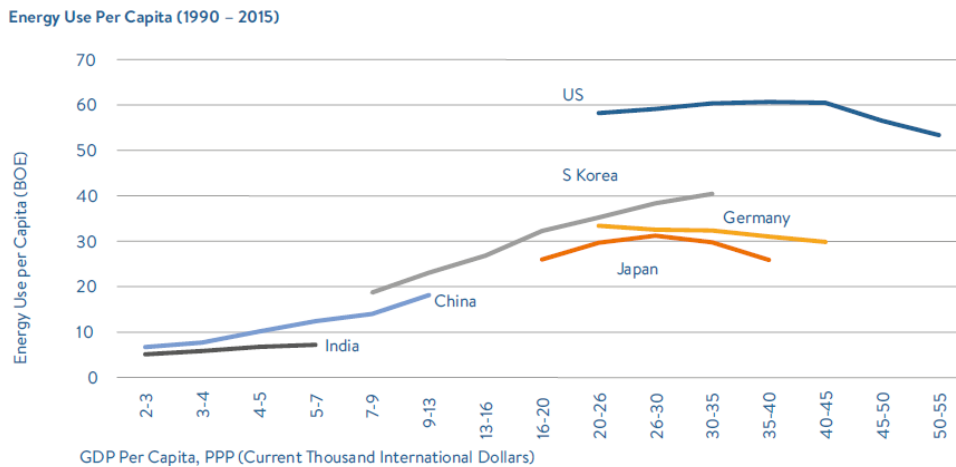


Figure 1-2. Energy use and per capita income of selected countries. Source: [5]

Coal accounts for about 41% of the electricity supplied globally [5]. The steady price of coal (at about \$2.2/MMBtu), and power generation costs from coal, along with the large and even availability across the globe, makes it a very attractive fuel for baseload power generation. Projections on the amount of extractable coal vary, but it is usually pegged at more than 100 years

at current consumption [7, 9]. Even in the U.S., with the current low cost of natural gas, coal is responsible for about one-third of the electricity generation.

1.2 Carbon Dioxide: Capture, Utilization, and Sequestration

Anthropogenic sources have contributed to a significant increase in atmospheric CO₂ concentrations since the industrial revolution, leading to an increase in the average global temperature [13, 14]. Concerns over the potential implications of global climate change have led to several efforts towards minimizing carbon dioxide emissions from human activities [15, 16]. Coal combustion is one of the leading sources of global CO₂ emissions. However, due to its large reserves and low prices, coal is projected to continue being one of the major energy sources in the long term [1, 7]. Thus, we need aggressive and cost effective CO₂ mitigation strategies for reducing emissions from coal-based power generation sources.

There are essentially three different ways to achieve CO₂ capture from coal based power generation sources:

Post-combustion capture—The CO₂ in the flue gas of a conventional power plant is separated using chemical or physical sorption processes [17-23]. Post-combustion capture is best suited for retrofit applications, as an add-on to existing power plants. However, due to the very low CO₂ concentrations in the flue gas (~ 14 vol%), the separation is very energy intensive. In the capture process, a large amount of heat load is required for the desorption step to regenerate the chemical or physical sorption material. This can significantly bring the efficiency of the process down (~ 10 %-pts.) [24].

Pre-combustion capture—The fuel is either gasified or reformed to syngas, a mixture of CO and H₂, from which CO₂ is formed using the water gas shift reaction with steam. This CO₂ is separated from the hydrogen by using a membrane based process, and the hydrogen is then used in a gas turbine [25-32]. Similar to post-combustion capture technologies, there is a high efficiency penalty (~ 10 %-pts.) for carbon capture with pre-combustion capture technologies. Still, it offers a slightly higher plant efficiency than the other capture methods [33]. However, the high capital costs associated with the carbon capture, the complexity of the process, and the reduced plant availability currently limit pre-combustion capture's acceptance as a viable, low-cost alternative [34].

Oxy-fuel combustion—Oxygen (with recycled flue gas to control temperature) is used, instead of air, for the combustion of coal, resulting in a concentrated CO₂ stream. In this process, the need to separate a dilute stream of CO₂ from the post-combustion flue gas is eliminated [35]. And unlike pre-combustion capture, oxy-fuel combustion is not a completely new and different method for power generation. It is very similar to the traditional method of power generation. Oxy-combustion has also been extensively used in industrial applications, and hence the major parts of the technology are relatively mature. However, the process of oxygen production is very energy intensive, and the net plant efficiency of oxy-combustion processes is similar to post-combustion capture based power plants.

Once captured by any of the processes, CO₂ could either be sequestered underground or utilized directly. One such use is enhanced oil recovery (EOR), which is an important means of increasing the amount of crude oil that can be extracted from an oil field. In deep oil wells (> 600 m depth), supercritical CO₂ can be injected to form an immiscible fluid with the oil, with a reduced viscosity. The lower viscosity fluid can then easily be pushed through the reservoir towards production wells, and extracted. Although other gases, such as methane, propane, butane, or nitrogen can be used

for miscible displacement, CO₂ is considered the most economical. Currently, about 4% of the U.S. oil production is through CO₂-EOR.

Beyond enhanced oil recovery, CO₂ can also be used in other areas, such as enhanced coal bed methane (ECBM) recovery. In this process, CO₂ is injected into unmineable coal seams with a high natural gas presence. The CO₂, due to its higher adhesion to coal, is able to displace the bound natural gas, which is then extracted. ECBM technology is still being researched, and is economically viable only in places where natural gas prices are high.

1.3 Oxy-Combustion

Oxy-fuel combustion was initially proposed in the early 1980s as a means to produce large quantities of CO₂ for EOR [36-38]. Industrial furnaces, such as used in glass, steel and cement production have also been extensively using this technology for several decades to obtain high temperature gases and highly radiating flames. With increasing concerns over global climate change, oxy-fuel combustion has been explored as a means of power production with carbon capture. There are several inherent benefits of oxy-combustion over other processes, such as its simplicity, and its low nitrogen content—which leads to low NO_x production. Several oxy-coal demonstration projects have been undertaken, such as the Schwarze Pumpe project in Germany and the Callide oxy-fuel project in Australia [39].

A schematic of the oxy-fuel combustion power plant concept is shown in Figure 1-3. As discussed above, the nitrogen and oxygen in air are separated in the air separation unit, and the oxygen stream (containing approximately 96% O₂ and 4% Ar) is then mixed with a large amount of recycled flue

gas before entering the boiler, to reduce the oxygen concentration of the stream to approximately 30 vol%. The coal is then combusted with this mixture of oxygen and recycled flue gas, and a CO₂-rich stream is produced as flue gas. After particulate and sulfur removal, and moisture condensation, the cleaned flue gas is sent to the CO₂ processing unit (CPU) for further polishing before finally being compressed and transported for utilization or sequestration. The flue gas can be recycled from a number of different places (before or after the FGD, before or after the FGC, etc.), with each location having its advantages and disadvantages, as discussed in Stanger et al. [39].

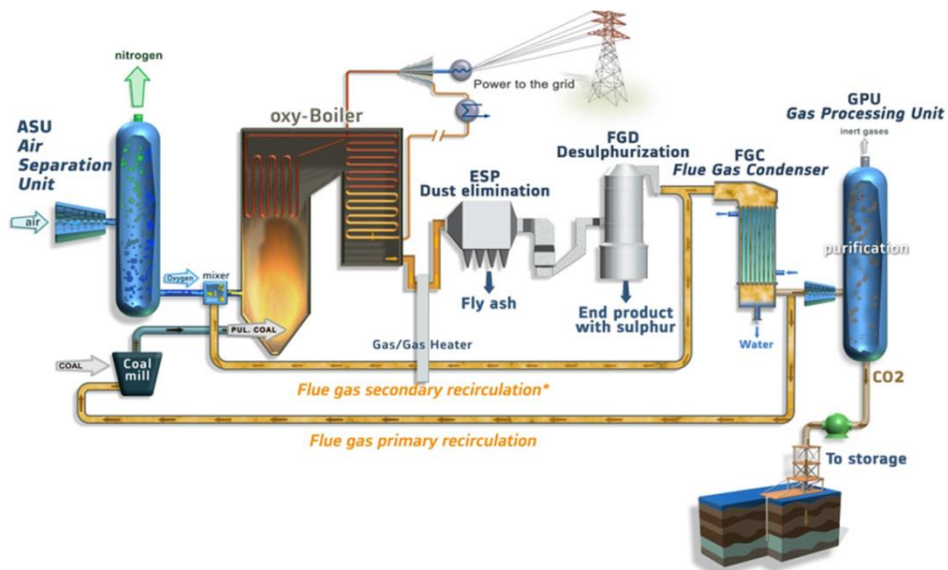


Figure 1-3. Schematic of an oxy-coal combustion power plant. Image source: Alstom

The flue gas recycle used to reduce the oxygen concentration before combustion in the boiler lowers the flame temperature to values similar to that in traditional air-firing systems. The flue gas recycle ratio is adjusted to control a number of parameters, such as flame temperature, radiative and convective heat flux to the boiler tubes, and exhaust gas temperature. These adjustments help

best utilize existing boilers for retrofit. Alternatively, in the case of a new build, it helps capitalize on decades of power plant operational know-how. The resultant flue gas recycle ratio is usually about 70 vol%. Recycling such a large amount of flue gas increases the capital costs, the operating (fan power) costs, and the efficiency penalty for power generation with carbon capture.

Air Separation:

There are a number of ways of producing oxygen from air, such as cryogenic, adsorption based, and membrane based processes. Cryogenic air separation is the only fully commercial technology which can produce oxygen at the scale required. With more than 90% of all industrial oxygen produced by cryogenic separation of air, the cost and performance of such ASUs are well established. Cryogenic separation is very energy intensive, and causes a significant loss in oxy-combustion plant efficiency. The efficiency of separation is continually being improved, with most of the improvement in cost and efficiency coming from improvements in the turbo-machinery. One of the disadvantages of the cryogenic process is that the similar volatilities of oxygen and argon make it difficult to separate the two. There is a sharp increase in energy cost for increasing the oxygen purity beyond approximately 96 vol%. Since in oxy-combustion, a separate CO₂ purification step is inherently required, the cryogenic air separation can be used with the 96% purity—avoiding the high cost of argon removal.

Ion transport membranes (ITM) offer potentially high efficiency air separation [40]. The process requires air at high temperature (1075 K) and pressure (14 bar), for the production of oxygen at much lower pressures (~ 1.5 bar), resulting in a huge pressure drop (about 3 times that in cryogenic processes). Tight heat integration in the ASU is required for this process to be efficient. The advantage of this process is the ability to obtain pure oxygen without a very high energy penalty

for the separation of Ar, as in cryogenic separation. However, the high temperature required for the activation of the membranes and the tight heat integration increase the complexity of this process.

Since adsorption and polymeric membrane processes for air separation are economical only when the oxygen requirement is less than 200 tpd and 20 tpd respectively [41], cryogenic air separation is considered here as the best available technology to produce oxygen for power generation.

CO₂ processing:

The flue gas from oxy-combustion boilers, though CO₂-rich, still needs further purification before it can be transported for either utilization or sequestration. A representative oxy-combustion flue gas stream composition is shown in Table 1-1. Table 1-2 shows the range of standards suggested for CO₂ purification for utilization and sequestration. There are a number of different configurations for the purification of CO₂, depending on the level of CO₂ purity requirement. To obtain extremely pure CO₂ for utilization, a distillation column is usually required. Details on the different configurations can be found in [42, 43]. In most configurations, the flue gas is initially pressurized up to about 35 bar, cooled in a platen heat exchanger (PHX), and then throttled to 10-15 bar for further cooling. The temperature in the cold box can reach approximately -50°C . This partially condenses the CO₂, and depending on the purity requirement is either separated from the other gases in a simple phase separator, or is fed to a distillation column for higher purity. The purified CO₂ is then vaporized in the PHX against the flue gas entering the cold box and then compressed up to approximately 150 bar for transportation to sequestration or utilization sites.

Table 1-1. A representative oxy-coal combustion flue gas stream. Adapted from [42]

Pressure	1 atm
<i>Composition by volume:</i>	
CO ₂	54.9%
N ₂	9.0%
Ar	2.5%
O ₂	3.5%
H ₂ O	30.0%
NO _x	220 ppm
SO _x	505 ppm
CO	275 ppm
Particulate matter	1.5 mg/Nm ³
Hg	15 ppb

Table 1-2. CO₂ purity standards [42, 44]

Component	Purity Target (Max. unless specified)
CO ₂	95–99.5% (min)
H ₂ O	10–300 ppmw
N ₂	10 ppmw–1%
O ₂	10–100 ppmw
Ar	10 ppmw–1%
CO	35–100 ppmw
SO ₂	1500–100 ppmw
NO _x	1500–100 ppmw

There have been a number of advances in the field of oxy-combustion in recent years. However, most of the advances are incremental, and the primary auxiliary loads of ASU, CPU, and flue gas recycle (FGR) cannot be overcome with merely incremental improvements. For high efficiency of power generation with carbon capture, there is a need to implement more radical and transformational designs.

1.4 Pressurized Oxy-Combustion

The inherent requirement of high pressure carbon dioxide for either enhanced oil recovery (EOR) or sequestration makes it possible to pressurize the oxy-combustion process with no intrinsic added cost or loss in efficiency, since compressing oxygen before combustion requires comparable energy to compressing carbon dioxide after combustion. An important benefit of pressurization is that the dew point of the flue gas moisture increases with pressure, so that at higher pressure, moisture condensation occurs at a higher temperature than at atmospheric pressure [45]. Hence, with pressurized oxy-combustion, a significant portion of the latent heat of condensation can be utilized in the steam cycle, instead of being wasted as it is in atmospheric pressure oxy-combustion [46, 47]. Thus, pressurized oxy-combustion is well-posed to increase the efficiency of carbon capture.

Previous analyses have indicated that pressurized oxy-combustion can improve overall plant efficiency by approximately 3 percentage points [48-50]. In brief, the primary benefits of pressurized oxy-combustion include the following:

1. The moisture in the flue gas condenses at higher temperature, and thus the latent heat of condensation can be utilized to improve the overall cycle efficiency.
2. The gas volume is greatly reduced; therefore, the size and cost of equipment can be reduced.
3. At higher pressure, the convective heat transfer to boiler tubes is increased for a given mean velocity. This increase is due to the increase in flue gas density with pressure, which in turn produces an increased Reynolds number and convective heat transfer coefficient [49]
4. Air ingress—which normally occurs in atmospheric pressure systems—is avoided, thereby increasing the purity of the CO₂ in the combustion products and reducing purification costs.

In fact, the elimination of air ingress may remove the need for cryogenic distillation within the CO₂ purification process, which would result in a significant cost savings, provided that the oxygen is sufficiently pure and the CO₂ purity requirements are not too stringent [51].

Pressurized oxy-combustion can, therefore, make significant progress towards achieving the U.S. DOE goals of at least 90% CO₂ removal at no more than a 35% increase in cost of electricity.

While different designs for pressurized oxy-combustion have been proposed, they must be carefully analyzed to ensure that they lead to significant efficiency gains beyond what is possible by optimizing atmospheric oxy-combustion. Even though any increase in efficiency is important, there are trade-offs in terms of the complexity of the process and the new training of the plant operators. Some pressurized oxy-combustion processes have been unable to achieve this step change in efficiency due to the sub-optimal utilization of the advantages provided by pressurizing the combustion process. For example, the ISOTHERM process of ITEA was one of the first designs for pressurized oxy-combustion [52, 53]. In this process, coal-water slurry is fed as fuel into a refractory lined reactor, with a combination of oxygen and some recycled flue gas. The amount of flue gas recycled to the combustor is only about 20%, because of the large amount of water added with the fuel. After combustion in a nearly adiabatic reactor, the hot flue gas is mixed with a large amount (~ 60%) of colder recycled flue gas from downstream. This large amount of recycling is to temper the flue gas so that its temperature is less than about 800°C before it enters a convective heat exchanger. This exchanger, called the heat recovery steam generator (HRSG), is the primary means of heat transfer to the boiler feed water. One of the biggest drawbacks of this process is the large (~ 80%) amount of flue gas recycle required. Another reason for the recycling is to increase the gas volumetric flow rate through the HRSG to improve the heat transfer rate. An independent analysis by Électricité de France (EDF) [54], the largest French utility, showed that

the efficiency of this process is even lower than that of a well-integrated atmospheric pressure oxy-combustion process. Thus, mere pressurization and extraction of the latent heat of flue gas moisture is not sufficient to provide a significant gain in power plant efficiency with carbon capture. Process innovation is required for optimal utilization of pressure in oxy-combustion.

1.5 Reducing Flue Gas Recycle in Oxy-Combustion

Since the combustion of coal with pure oxygen could result in adiabatic flame temperatures on the order of 3000 K, most oxy-combustion concepts incorporate the recycle of about 65-80% of flue gas back to the boiler to control the flame temperature and thereby the wall heat flux. Thus, though the reduction in flue gas recycle could reduce the cost and energy penalty, it is quite challenging. A number of approaches have been proposed to reduce the flue gas recycle without significant negative impact on the boiler performance or safety [55, 56]. A few have been tested in demonstration units, but only in industrial furnaces or boilers operating with low temperature and pressure steam, where much harsher conditions could be tolerated in these systems than in utility boilers [55]. Notable among these is the approach of Goanta et al. [56], who used controlled non-stoichiometric burners, placed at several heights, to control the adiabatic flame temperatures of the individual flames. Tests were conducted to try to reduce the flue gas recycle to 50%, with three burner levels, each operating at a different stoichiometric ratio. The modeling and experimental results show flame impingement on the wall [56, 57]. The results also showed that even if only the non-impingement side of the furnace was analyzed, the difference in peak heat fluxes between air-fired and oxy-combustion with 50% flue gas recycle could be as much as 50% higher for the oxy-combustion case [57]. Since even at 50% flue gas recycle, the increase in heat flux was high,

further reduction was not considered. Chapter 4 contains more discussion on the boiler design challenges posed by low flue gas recycle.

1.6 Scope of the Dissertation

The work presented in this dissertation can broadly be divided into two parts: development of a high efficiency power generation process with carbon capture, and development of burner and boiler design strategies to control wall heat flux in such a process.

In this chapter, advantages and challenges of pressurized oxy-combustion were discussed. It was seen that even though, due to the extraction of hitherto unutilized thermal energy, pressurized oxy-combustion should have a higher efficiency, it might not. Further, process design for high efficiency power generation has to take into account various factors affected by increasing pressure. In Chapter 2, a new process—staged, pressurized oxy-combustion (SPOC)—for electricity generation with carbon capture is presented. The process modeling for the SPOC power plant is done using Aspen Plus™ and the performance results are discussed. The plant design proposed is not only a pressurized oxy-combustion system, but also utilizes only a very small amount of flue gas recycle. The economic analysis conducted to ascertain the cost of electricity produced using this process will also be briefly discussed. In Chapter 3, results of a detailed parametric analysis are presented. The key process parameters that affect the plant efficiency are varied to identify the best operating conditions for SPOC.

Chapter 4 will identify the key challenges that exist in the design of a high pressure, low recycle oxy-combustion burner and boiler. The next two Chapters, 5 and 6, will address the design

constraints for developing a burner and boiler design that is both practical and flexible. Computational Fluid Dynamic (CFD) simulation will be used to design the burner and boiler. Emphasis will be placed on controlling the wall heat flux, since that is the critical constraint in the design of a low recycle boiler. Chapter 7 will discuss the sooting tendencies in such high temperature systems, and will also present the reasons for lower soot in the design presented in Chapters 5 and 6. Chapter 7 will present both analytical modeling of simple laminar flames, to understand the fundamental reasons limiting soot inception, and experimentally obtained exhaust soot concentrations and size distributions from more practical, turbulent flames.

This dissertation contains four appendices. In Appendix A, the selection criteria for the CFD sub-models and the sensitivity studies of the particle and wall properties are discussed. Appendix B is a reproduction of [58], and is provided as a methodology developed to control soot and radiative heat flux from high temperature, turbulent diffusion flames. The appendix is a combination of experimental results and CFD simulations with detailed chemical mechanisms. Appendix C provides the nomenclature, non-dimensionalization approach and the formulation of the Burke-Schumann model extended to tri-axial flames with the fuel in the middle tube. The basic formulation is due to Chao and Axelbaum [59], with some new extensions added to obtain the contours of carbon-to-oxygen atom ratio. Appendix D is a discussion on the effect of fuel-moisture on volatile breakthrough during co-firing two fuels.

Chapter 2

Staged, Pressurized Oxy-Combustion

2.1 Introduction

As discussed in Chapter 1, the pressurization of oxy-combustion process can provide significant advantages with respect to gain in net plant efficiency. Still, depending on the process configuration a significant loss in efficiency due to recycle and slurry feeding may result. In this work, a unique pressurized oxy-combustion process is described that aims to further improve the efficiency and costs by reducing the recycling of flue gas to near zero. Normally, in the absence of recycled flue gas or another inert gas, combustion of fuel and oxygen results in a dramatic increase in temperature of the combustion products and the rate of radiant heat transfer [55]. The resulting high heat flux to the boiler tubes may result in tube surface temperatures that exceed safe operating limits. In the Staged Pressurized Oxy-Combustion (SPOC) process, this problem is addressed by staging the delivery of fuel and controlling the characteristics of the flame.

The aim of this work is to evaluate the application of the fuel-staged approach to pressurized oxy-combustion (SPOC) that has heretofore not been considered, and to understand and quantify its potential benefits by modeling the process and analyzing the performance of this system. Later chapters, viz., Chapters 4–6, will discuss in detail the methods to control heat flux in low flue gas recycle boilers.

2.2 Process Summary

2.2.1 Fuel-staged oxy-combustion

In order to reduce the mean combustion product temperature and heat flux associated with burning coal in nearly pure O₂, the burner and boiler must be designed specifically to address this. The design must be compatible with the configuration of a pressurized boiler as well. The SPOC approach incorporates a number of different concepts to address this. As with air-firing combustion, non-reacting gases must be present to dilute and to absorb a portion of the heat released from combustion. With air-firing combustion N₂ plays this role, and in first generation oxy-combustion systems the dilution gases are combustion products (CO₂ and H₂O) in the recycled flue gas. In the fuel staging approach described below both combustion products and excess O₂ are utilized for dilution.

One approach to fuel staging to reduce flue gas recycle (FGR) in an oxy-fuel process has been studied by Technical University of Munich [56, 57, 60]. Both numerical and experimental results have been reported with the goal of reducing flue gas recycle under atmospheric pressure conditions. To achieve controlled staging, the concept of utilizing non-stoichiometric burners was investigated. In a traditional boiler, the fuel is generally supplied with an amount of oxygen that is in slight excess (in the range of 3%) of that required for stoichiometric combustion of the fuel to ensure complete combustion. On the other hand, in the fuel-staged combustion approach, in the first stage there is an over-supply of oxygen, as characterized by the stoichiometric ratio, λ , which is defined as the ratio of the mass of oxygen supplied to the mass of oxygen required for stoichiometric combustion of the fuel. The aim of the work at TU Munich was to reduce the flue gas recirculation rate from the typical 75% to around 50% of the total flow. While the temperatures

were maintained at acceptable levels, the heat flux increased by 4-11% compared to the traditional oxy-fuel approach with high recycle.

The SPOC concept of fuel staging is somewhat different from this and is depicted in Figure 2-1. Unlike the staged approach described above, the SPOC process is designed to operate each stage as a separate boiler, with the fuel distributed to the various stages. The oxygen is primarily supplied to the first stage, whereas some amount of oxygen is/could also be supplied to the other stages to improve combustion characteristics. As can be expected with such a process design, in the first stage there is an over-supply of oxygen, i.e., $\lambda \gg 1$. The large amount of excess O_2 effectively acts as a diluent, thereby assisting in the control of the well-mixed temperature of the combustion products and downstream heat transfer. The near-burner heat transfer control is more complicated and will be described in Chapters 4–6. In the SPOC process, heat is extracted from the first stage into the Rankine steam cycle. Once the flue gas temperature is sufficiently reduced, the products of combustion from stage 1, including excess O_2 are passed to Stage 2 where additional fuel (and oxygen) is injected, and more O_2 is consumed. This process continues in multiple stages until all the fuel, and nearly all of the O_2 is consumed.

It is important to note that the total gas flow in SPOC process is equivalent to the case in which coal and oxygen, in nearly stoichiometric proportion, are combusted in a single stage, i.e., there is no net addition of dilution gases, but when staging the combustion process, dilution is available, in a local sense, in each stage of combustion. The exact number of stages chosen for the process is dependent on the amount of burner and boiler configuration, flue gas recycle, and other constraints discussed in later chapters. With the assumption of a fixed furnace end flue gas temperature (FEGT), the number of stages will not affect the heat and mass balance, or the location for the integration of the heat with the steam Rankine cycle.

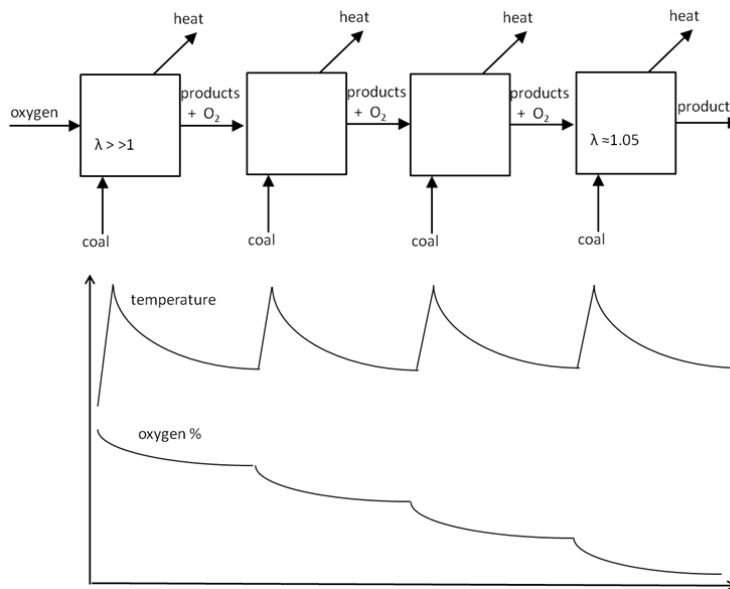


Figure 2-1. Depiction of the staged combustion concept.

2.2.2 Process description

A process flow diagram for a power plant incorporating the SPOC process is illustrated in Figures 2-2 and 2-3, and is briefly described below. Oxygen is produced via cryogenic separation of air. Heat generated from the compression of air is integrated with the steam cycle and utilized for boiler feed water regeneration. Staged combustion of fuel is carried out using three combustion vessels or boilers in series. Coal is fed with a pneumatic dry feeder using a small amount of recycled flue gas as motive gas. This feed system is modeled after systems developed by Siemens [61], Shell and Mitsubishi [62] for coal gasification. Other feeding techniques, like dry solids pump, which are capable of delivering dry coal at up to 40 bar without the aid of a motive gas [63, 64] and slurry feed can also be considered, although slurry feeding is detrimental to plant efficiency due to the added water (see Chapter 3).

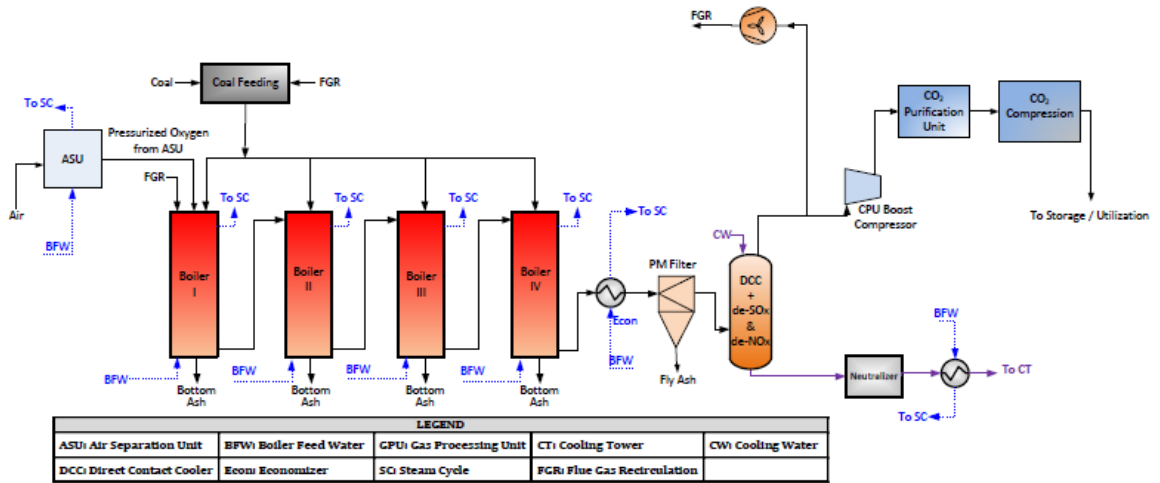


Figure 2-3. Gas side process flow diagram for the SPOC process.

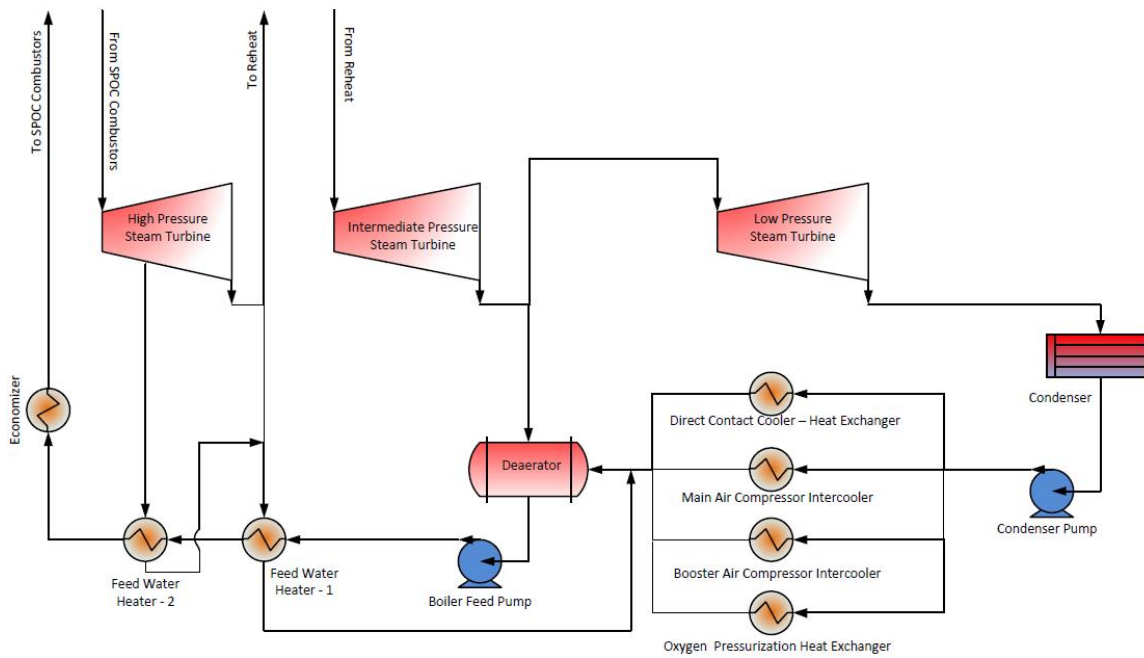


Figure 2-2. Steam side process flow diagram for the SPOC process.

In the present analysis for the process model, it is assumed that coal is delivered to each of the boilers in roughly equal amounts, and all the oxygen is delivered to the first stage (Boiler 1). In practice the distribution of the fuel and the oxygen could be different to affect the heat transfer characteristics. Any variation in the distribution of the fuel and oxidizer has no effect on the process modeling results. In the boiler, heat of combustion is transferred to a steam Rankine cycle, primarily by radiation. The products of Boiler 1 are passed to Boiler 2. The oxygen contained in the products of Boiler 1 is available to combust the coal in Boiler 2, along with any extra oxygen added to Boiler 2. This process continues until nearly all of the oxygen is consumed in the final radiative boiler. The temperature of the products is further reduced in a convective heat exchanger (Economizer) followed by fly ash removal in a candle filter. After the particulates have been removed, the flue gas is further cooled, its moisture condensed, and the pollutants (SO_2 and NO_x) removed in the Direct Contact Column (DCC). A small fraction of this cooled and dry flue gas is recycled back to the boilers as motive gas, while the majority goes to the CPU where it is further purified to meet the stringent specifications for Enhanced Oil Recovery.

The details of each of these processes and the key assumptions associated with them are given in Section 2.3.

2.3 Modeling Approach and Key Assumptions

For comparison with atmospheric oxy-combustion and air-fired combustion, a process modeling approach that is similar to the National Energy Technology Laboratory (NETL) studies, and NETL guidelines for process modeling, CO_2 purity, etc. was used [44, 65-67]. Aspen Plus™ (v7.3.2) software was used for the process modeling. Two cases were modeled, corresponding to two fuel

types: bituminous and sub-bituminous coal. The modeled pressurized oxy-combustion (SPOC) power plant has an output of 550 MW_e (net) with a supercritical Rankine cycle – 241 bar/593°C/593°C (3500 psig/1100°F/1100°F), and is located at a generic Midwest ISO location [67]. The process was modeled for 90% carbon capture and Enhanced Oil Recovery grade purity. The site conditions and CO₂ purity requirements are detailed in Tables 2-1 and 2-2 respectively. The design, operating and performance characteristics of the key components of the SPOC models are shown in Table 2-3. The SPOC models were compared to the reference case (“Current Technology” or “Base Case”) in the DOE/NETL oxy-combustion R&D guide, which is an ASPEN model of an atmospheric pressure supercritical steam oxy-combustion case [68].

Table 2-1. Site conditions

Site Conditions	Midwest ISO
Elevation, m (ft)	0 (0)
Barometric Pressure, MPa (psia)	0.101 (14.7)
Design Ambient Dry Bulb Temperature, °C (°F)	15 (59)
Design Ambient Wet Bulb Temperature, °C (°F)	10.8 (51.5)
Design Ambient Relative Humidity, %	60
Cooling Water Temperature, °C (°F)	15.6 (60)
Air Composition, mass%	
H ₂ O	0.616
AR	1.280
CO ₂	0.050
O ₂	22.999
N ₂	75.055
Total	100.00

Table 2-2. CO₂ purity requirement for EOR and CO₂ purity achieved with the SPOC process

Component	Enhanced Oil Recovery Target (Max. unless specified) [44]	SPOC Case
CO ₂	95% (min)	>99.9%
H ₂ O	300ppmw	trace
N ₂	1%	11ppb
O ₂	100ppm	10ppm
Ar	1%	13ppm
H ₂	1%	trace
CO	35ppm	trace
SO ₂	100ppm	trace
NO _x	100ppm	trace

Table 2-3. Key components data

Component/ Subsystem	Technology Type, Basis for Design & Performance	Operating Conditions				Performance Characteristics	Notes
		Inlet		Outlet			
		Temp. (°C)	Press. (MPa)	Temp. (°C)	Press. (MPa)		
air separation unit	Cryogenic. vendor data/ commercial design	15.6	0.11	20	0.11	95.9% purity O ₂ . 213kWh/tO ₂ aux power req.	
oxygen compressor	NETL guidelines[67]	20	0.11	185	1.6	84% isentropic efficiency	Multistage compression with intercoolers.
coal milling	vendor data/ commercial design	25	0.1	49.5	0.1	15.4kWh/tCoal	typical grind size for PC application
coal feeding	Pneumatic dry feed. vendor data/ commercial design	49.5	0.1	53	1.6	15 lbs coal/ lbs feed gas	Proven technology for IGCC applications can be applied
radiant boilers I-IV	self-defined	coal: 50 O ₂ : 185	1.6	700	1.6	approx. 1% heat loss	- Analogous to radiant syngas cooler for IGCC. - Fly ash/bottom ash split equal to other PC systems.
economizer	vendor data/ commercial design	700	1.6	330	1.57		
particulate filter	Candle filter. vendor data/ commercial design	330	1.57	330	1.55	98% ash	
DCC + de-SO _x & de- NO _x column	Counterflow packed bed. vendor data/ commercial design	330	1.55	26.2	1.5	100% SO _x and NO _x .	High efficiency conversion into acids will occur at 15 bar, SO _x /NO _x < 2 .

intermediate flue gas compressor	NETL guidelines [67]	26.2	1.5	92.3	3.5	86% polytropic stage efficiency	
CO ₂ cryogenic purification unit	Cryogenic. Vendor data/ commercial design	21.2	3.5	44	15.3	90% CO ₂ capture. ~45.8 kWh/tCO ₂	Includes CO ₂ auto- refrigeration cycle & cryogenic distillation. Meets EOR purity specs [44].
steam turbine (SC)	NETL guidelines[67]	593	24.2	32.2	0.005	single reheat at 4.9MPa to 593 C	

2.3.1 Operating pressure

To determine the appropriate operating pressure for the boilers, three aspects of the process were considered. First, an initial analysis on the flue gas moisture condensation as a function of pressure and temperature was conducted. This study revealed that for pressures higher than 10 bar and flue gas temperatures lower than 50°C, the amount of flue gas moisture condensation did not vary significantly with pressure, with a maximum variation of less than 1% for a pressure variation from 10 bar to 35 bar. Second, the pressure for effective removal of SO₂ and NO_x in the integrated removal approach has been reported as approx. 15 bar [69, 70]. Operating the boilers at a slightly higher pressure was considered to be advantageous to avoid additional equipment (*e.g.*, compressors or fans) before the flue gas cleanup, avoiding possible condensation and corrosion in such equipment. Lastly, in order to transfer most of the heat extracted at the direct contact column to the cold boiler feed water for regeneration while maintaining the minimum approach temperature in the regenerator, an additional constraint was imposed on the operating pressure of the process. A pressure high enough to transfer the heat to the boiler feed water without violating the minimum temperature approach was required. For an approach temperature of ~ 9°C, the DCC was required to be operated at approx. 15 bar. Based on these three considerations, a pressure of 16 bar was selected to account for pressure losses from the combustors to the DCC as given in

Table 2-3. The fluid mechanics was also a consideration in choosing pressure but this will not be discussed here.

2.3.2 Radiant and convective heat exchanger

The combustors were modeled as described in the Aspen Plus™ solids modeling guidelines [71] and also by others in literature [72]. The exit temperature of the flue gas from each combustion stage was chosen to be 700°C. Flue gas from the end of the last stage of the process was then sent to an economizer (convective heat exchange). The temperature of the flue gas exiting the economizer was chosen to be 330°C to prevent acid condensation in the heat exchanger. This was based on model prediction of the dew point (~274°C) with a conservative safety factor. Since such predictions based on thermodynamics are not always accurate [73, 74] and experimental data on acid dew point is not available for the conditions of this process, a temperature much higher than that predicted by the model, and also higher than those used by others for pressurized coal combustion [50, 75] was used, as this was deemed to be conservative.

2.3.3 Direct contact column (DCC) and integrated pollutant removal

Further cooling and moisture condensation occurs in a contacting column, with cooling water flowing from the top, and flue gas from the bottom. This column has a dual role. The first is to cool and condense the moisture from the flue gas, which occurs in the bottom stages. The second is to remove SO_x and NO_x, via conversion to dilute sulfuric and nitric acid, which is performed in the top stages. The integrated SO_x and NO_x removal from gases at elevated pressure has been studied for power plant applications [76]. Air Products and other gas technology providers have

been developing various processes of “sour gas compression” for oxy-combustion applications, in which removal of sulfur and nitrogen containing species in the flue gas is enhanced due to their mutual interaction during the flue gas compression process.

The integrated SO_x and NO_x removal has been associated with the “lead-chamber” reactions [77, 78], the overall reaction of which is shown here as Reaction D in Table 2-4. Several groups have recently investigated this reaction mechanism in more detail [79-81] and have concluded that the “lead chamber” reactions are not likely to play a critical role in this process due to the requirement of high sulfuric acid concentrations (70-80%) for such reactions to be important. These studies have argued that the conversion of NO_x and SO₂ to acids is more likely to occur via some complex liquid phase reactions between HNO₂, H₂SO₃ and possibly H₂SO₄. Even though the exact reaction mechanism is still under investigation, the experimental results from Air Products have indicated that when the SO₂ / NO_x ratio controls the removal efficiency, with a lower SO_x/NO_x ratio resulting in a higher removal efficiency [69, 82, 83]. The SPOC process is expected to remove almost all of the SO₂ and NO_x as it can produce higher NO_x than in a typical oxy-combustion system (due to the high local flame temperatures) and hence has a lower SO_x/NO_x ratio. Mercury present in the flue gas can also be removed in the same column either via dissolution or reaction with HNO₃ forming Hg(NO₃)₂ [77].

Table 2-4. Reactions assumed for the direct contact column for SO₂ and NO_x removal

Reaction	Phase	No.
$\text{NO} + \frac{1}{2} \text{O}_2 = \text{NO}_2$	Gas phase	(A)
$\text{NO}_2 + \text{SO}_2 + \text{H}_2\text{O} = \text{NO} + \text{H}_2\text{SO}_4$	Gas phase	(B)
$2\text{NO}_2 = \text{N}_2\text{O}_4$	Gas phase	(C)
$\text{N}_2\text{O}_4 + \text{H}_2\text{O} = \text{HNO}_2 + \text{HNO}_3$	Liquid phase	(D)
$3\text{HNO}_2 = \text{HNO}_3 + 2\text{NO} + \text{H}_2\text{O}$	Liquid phase	(E)
$\text{SO}_3 + \text{H}_2\text{O} = \text{H}_2\text{SO}_4$	Liquid phase	(F)

In this work, as with others who have modeled such integrated pollutant removal [70, 78, 84], the reactions chosen for modeling were based on the lead-chamber mechanism. As the experimental results from Doosan Babcock and Air Products [69, 70] indicate nearly complete removal of SO_x and NO_x at the conditions similar to the SPOC exhaust, and the process modeling results with a large enough residence time in the column also lead to complete removal of both the gases, modifying the mechanism would not affect the process modeling results. It could however impact the costing of the equipment due to differences in terms of the residence time required in the column. The removal efficiency was also found to be a function of the SO_x / NO_x ratio, and Air Products has suggested the use of an extra column at about 30 bar for a near 100% removal of the NO_x [69]. This has not been considered in the process model presented here. If further polishing of NO_x is found necessary for the SPOC process (based on pilot scale experiments to be conducted at Washington University), an additional efficiency penalty of no more than 0.05 percentage points will be added, since the clean flue gas inherently requires further compression to 35 bar in the CPU for auto-refrigeration requirements [85]. Another factor that enhances the removal efficiency in the SPOC process is that all the cooling water used in the column is fresh water and not recycled with acids [69].

In the reactions modeled for the DCC, Reaction A is a slow reaction but the rate increases with increasing pressure (3rd order) and decreasing temperature. Reactions B, C and E are fast and are equilibrium limited [77]. Reaction D is a kinetically controlled reaction.

The integrated pollutant removal system has been proposed as either two separate columns [50, 69, 77] or a single column [78]. To minimize equipment exposed to corroding acids (columns and heat exchangers), a single column approach was chosen, and the moisture condensation step was also integrated into the same column. Since rate of the overall rate-limiting Reaction A increases

with decreasing temperature, the flow rates of the liquid in the column and the column height were adjusted to allow the top stages to be at low temperature, promoting the reactions, while most of the cooling and condensation occurs in the bottom stages. Since the column is at high pressure, the size of the column would be much smaller than that at atmospheric pressure.

The cooling water used in the direct contact column for cooling and condensation exits the bottom of the column at relatively high temperature ($\sim 165^{\circ}\text{C}$), with an acid concentration of about 730-4000 ppmv, depending upon the sulfur content of the coal. After neutralization of these dilute acids with caustic, the water is passed through an indirect heat exchanger for regeneration of low temperature BFW. This heat, in conjunction with the low-grade heat that is available from the ASU, eliminates or nearly eliminates (depending on the fuel) the need for steam extraction from the low-pressure turbine, allowing for higher gross power generation.

2.3.4 CO₂ purification unit (CPU)

After removal of particulates, SO_x, and NO_x, the flue gas is compressed to a pressure of 35 bar. A small fraction ($\sim 3\text{-}5\%$) of this compressed, dry and clean flue gas is recycled back for carrying the coal in a dense phase, while the majority ($>95\%$) is sent to the CPU after passing through molecular sieves for further moisture removal, and a bed of an activated carbon for removal of any mercury remaining in the gas.

The CPU uses cryogenic distillation to purify the CO₂ to the desired EOR specification. Two designs were initially analyzed – an ammonia chilled CPU (external cooling cycle), and an auto-refrigeration CPU. The auto-refrigeration CPU was found to be significantly more efficient, and the other option was dropped at an early stage in the model optimization.

2.3.5 Other considerations

A sub-bituminous Wyoming Powder River Basin coal (Case A), and a bituminous Illinois #6 coal (Case B) were assumed for fuels, and their proximate and ultimate analyses are shown in Table 2-5 [65]. In order to model coal combustion, coal was defined as a non-conventional component and its proximate & ultimate analysis and heating value were provided as user-inputs. The raw coal was dried to the desired level (as-fired moisture: 24% for Case A and 9.75% for Case B) in a dryer block with a hot and dry nitrogen stream from the ASU. The nitrogen from ASU was heated with a portion of the heat available from air compression. This heat in atmospheric oxy-combustion models can be used for pre-heating oxygen with tight heat-integration. For pressurized combustion, the oxygen compression provides more than the requisite pre-heating (the excess heat being utilized for steam regeneration). The dried coal feed was then split and fed into each of the combustion stages with a small amount of recycled flue gas using a pneumatic dry feed system [61].

Since adsorption and polymeric membrane processes for air separation are economical only when the oxygen requirement is less than 200 tpd and 20 tpd respectively [41], a cryogenic ASU was chosen for this study. Air separation was performed at low pressure (1-5bar) in a 3 column cryogenic unit, producing oxygen of 95.9 vol% purity (0.1% N₂ and 4% Ar). The specific power consumption for air-separation to atmospheric pressure oxygen was 213 kWh/tO₂ [86]. This oxygen stream was then compressed in multiple stages with intercooling to reach the desired combustor operating pressure (16 bar). The intercoolers for both the air and oxygen compressors used boiler feed water (BFW) as the coolant.

Table 2-5. Properties of Wyodak/Anderson PRB sub-bituminous coal and Illinois #6 bituminous coal on an as-received basis [65]

Proximate Analysis	PRB	Illinois #6
Moisture	27.42%	11.12%
Volatile Matter	31.65%	34.99%
Ash	4.50%	9.70%
Fixed Carbon	36.43%	44.19%
Total	100.00%	100.00%
Ultimate Analysis		
Carbon	50.23%	63.75%
Hydrogen	3.41%	4.50%
Nitrogen	0.65%	1.25%
Sulfur	0.22%	2.51%
Chlorine	0.02%	0.29%
Ash	4.50%	9.70%
Moisture	27.42%	11.12%
Oxygen	13.55%	6.88%
Total	100.00%	100.00%
Heating Value	As-Received (Reported)	As-Received (Reported)
HHV (kJ/kg)	20,469	27,113

The steam turbine, generator and motor efficiencies were obtained from the guidelines issued by the U.S. Dept. of Energy for process modeling of coal-based power plants (shown in Table 2-6) [66]. The steam side was modeled with a governing stage, high-pressure, intermediate-pressure and low-pressure turbines. For regeneration of boiler feed water, the high-pressure turbine has two steam extractions, the intermediate has one, and the low pressure has none. The condenser pressure is 0.048 bar and operates with a terminal temperature difference of 11.7°C.

For the gas side modeling, the Peng-Robinson equation of state was used. For SO_x and NO_x removal, the ENRTL-RK method (ENRTL activity coefficient method with RK equation of state) was used so as to model the stream of dilute acid formed and the electrolytes present in the unit. For the steam side (Rankine cycle), STEAM-TA (steam tables) was used.

Table 2-6. Key process parameters [43, 66, 67]

Parameter	Value
Governing Stage Efficiency	85%
High Pressure Efficiency	91.5%
Intermediate Pressure Efficiency	94%
Low Pressure Efficiency	89.2%
Generator Efficiency	98.8%
Motor Efficiency	97%
Condenser Pressure	0.048 bar
ASU Specific power consumption (at ~ 1 bar)	213 kWh/tonneO ₂

2.4 Results and Discussions of Process Modeling

The outlet flow rates and composition from each of the combustor stages for a 550 MW_e plant firing PRB coal is shown in Table 2.7 as an example of the conditions. The outlet oxygen concentration at Stage 4 is set to approx. 3% on a dry basis [67], which for the low recycle SPOC case corresponds to 1.7% on a wet basis. In terms of partial pressure of oxygen, this value is equal to 0.26 bar, which is almost an order of magnitude higher than atmospheric pressure combustion in air, with an [O₂] of 5%. Since the excess oxygen is to ensure complete conversion of char, which is a function of the partial pressure of oxygen in the reactor, the value used in the current modeling of SPOC was deemed sufficient.

Table 2-7. Flow rates and compositions at the outlet of each stage in the SPOC process firing PRB coal producing 550 MWe power.

V-L Mole Fraction	Stage 1 out	Stage 2 out	Stage 3 out	Stage 4 out
Ar	0.036	0.032	0.029	0.027
CO ₂	0.192	0.343	0.465	0.564
H ₂	0.000	0	0	0.000
H ₂ O	0.132	0.236	0.319	0.388
N ₂	0.002	0.003	0.003	0.004
O ₂	0.638	0.386	0.184	0.017
NO _x	TBD	TBD	TBD	TBD
SO _x	0.00025	0.00025	0.00025	0.00025
Total	1	1	1	1
V-L Flowrate (kmol/hr)	15202.8	17042.4	18876.96	20709.58
V-L Flowrate (kg/hr)	497934	563864.4	629798.4	695728.8
Solid Flowrate (kg/hr)	2436.48	4874.4	7309.44	9745.2
Temperature (°C)	700	700	700	700
Pressure (Mpa, abs)	1.6	1.6	1.6	1.6

The performance summaries (and comparison with 1 atm oxy-combustion) for the two cases are shown in Table 2-8. The net plant efficiency (HHV) for Case A was found to be 35.7%, while that of Case B was 36.7%, indicating that the process is more efficient when using bituminous coal over lower rank sub-bituminous coal. The Integrated Environmental Control Model (IECM v8.0.2), which is a publicly available modeling tool developed by Carnegie Mellon University [87], was used to obtain a comparison for the decrease in net plant efficiency for a typical, atmospheric pressure oxy-coal power plant operating at the same ambient conditions on fuel switching from a high rank Illinois #6 to a low rank PRB coal. The decrease in efficiency for a typical oxy-coal plant is 7.4%, compared to 2.7% for the SPOC process. The efficiency penalty typically associated with high moisture fuels is not as significant here due to the fact that a significant portion of the latent heat of water is captured in the SPOC process.

Table 2-8. Performance comparison of SPOC process (Case A and B) with relevant atmospheric pressure reference cases

Performance Parameters	Units	PRB SPOC Process (Case A)	Illinois #6 SPOC Process (Case B)	Current Technology Oxy-coal [68]	No Capture, Air-fired [68]
Gross Power Output (After Generator Loss)	MW _e	729.2	733.1	787.8	580.4
Total Oxygen Production Load	MW _e	126.2	127.0	126.7	-
ASU Main Air Compressors and other auxiliaries	MW _e	90.1	90.6	126.7	-
Oxygen Compressors	MW _e	36.1	36.4	–	-
Total Clean-up and CPU load	MW _e	20.5	19.4	77.55	4.5
Other Auxiliaries and Misc. Balance of Plant	MW _e	32.8	31.6	33.53	25.9
Total Auxiliary Load	MW _e	179.5	178.0	237.8	30.4
Net Power Output	MW _e	549.6	555.1	550.0	550.0
Net Plant Efficiency(HHV)	%	35.7	36.7	29.3	39.3
Thermal Input (HHV)	MW _{th}	1,539.3	1,511.8	1,879.2	1,400.2

An efficiency penalty for CO₂ capture of only about 2.6 percentage points was observed for the SPOC cases as compared to 10 percentage points for the reference atmospheric oxy-combustion case reported by DOE/NETL [41, 88]. The improvement in net plant efficiency over the atmospheric pressure cases is due to a number of factors. Most of these are related to the SPOC technology and these will be discussed in detail in the following sub-sections. Others are related to differences in the assumed steam turbine efficiencies, condenser operating conditions, etc. These contributions are not intrinsically associated with the SPOC process and will be identified in the comparison.

As shown in Table 2-2, the purity of the CO₂ that is captured with the SPOC process meets the purity standards for Enhanced Oil Recovery (EOR) set by DOE/NETL, and even meets the more stringent standards set by Kinder-Morgan and others [44, 89].

2.4.1 Auxiliary load comparison

About 28% of the total oxygen production load in the SPOC process is due to oxygen compression to 16 bar, but since the resulting flue gas is at higher pressure, the CPU compression power is equivalently reduced. The power summaries are compared in Table 2-8. Due to the higher efficiency (lower heat rate), the auxiliary load is about 33% lower in the SPOC process than in the atmospheric pressure process (the comparison is based on auxiliary load without feed water pumps as the pumps are turbine driven in the atmospheric pressure report and electric motor driven for the SPOC cases). This reduction is a sum of reduction due to lower oxygen production, and the reduced gas volume that needs to be purified and compressed for the same power output. The SPOC process eliminates the requirement of recycled flue gas for temperature control and only 3-5% of the total flue gas is required for dense-phase coal feeding. Consequently, the fan power requirement for flue gas recycle in the SPOC process is small. Whereas, it has been reported in prior studies that the fan load for recycle reduces efficiency by ~ 0.4–4 percentage points (based on fuel thermal input) at various combustion pressures analyzed [41, 50].

Another factor that results in a lower auxiliary load for the SPOC process is the lower CPU power load that results from the elimination of air in-leakage at high pressure, and hence a purer CO₂ stream entering the CPU.

2.4.2 Heat integration and net plant efficiency

The net plant efficiency for SPOC cases is about 7.4 percentage points higher than for the atmospheric pressure reference oxy-combustion case [41]. This increase in efficiency cannot be attributed to a single aspect of the design but is rather a result of a number of incremental increases in various units of the process. The direct contact cooler/condenser (DCC) is a major contributor

towards the increase in efficiency of the SPOC process over atmospheric oxy-combustion, adding about 10% extra heat into the Rankine cycle ($\sim 0.1 \text{ MW}_t / \text{MW}_t$ input) in the PRB case. Since not all of the latent heat from the moisture in the flue gas is recoverable, a lower moisture fuel will inherently have lower losses. Illinois #6 coal (Case B) has lower moisture and the net plant efficiency is higher than for Case A with PRB coal as seen in Table 7.

As previously stated, pressurization of oxygen to the combustor pressure was performed with a multistage compressor with intercooler. The compressed oxygen is at approx. 185°C , eliminating the need for further oxygen pre-heating, which in first generation oxy-combustion processes is done using heat from the Main Air Compressor (MAC) and Booster Air Compressor (BAC) intercoolers. The extra heat thus available in the SPOC process, from the MAC and BAC intercoolers and the oxygen compressor intercooler was also integrated with the Rankine cycle, by utilizing low pressure BFW as the coolant, increasing the net plant efficiency further.

2.4.3 Efficiency improvements breakdown

There are a number of different reasons for the improved efficiency of SPOC [46] over first-generation oxy-combustion [68], as well as other pressurized oxy-combustion concepts [50]. The benefits primarily arise due to pressurization and staging. With pressurization, as discussed above, the latent heat of flue gas can be condensed and utilized in the steam Rankine cycle. This adds a large amount of heat into the cycle and. Though important, this is not the only major cause of high efficiency of SPOC. Staging of fuel (and oxygen) also plays a major role in enhancing the efficiency of the SPOC process by aiding flue gas recycle reduction. The impact of reduced recycle on efficiency is not only due to the reduced fan power consumption for recycling, which could be between 0.4–1.2 %-pts. [35, 50]. The benefit also arises from the reduced exergy losses due to higher heat transfer in the high temperature region and less heat transfer in the low temperature.

With higher recycle, the gas volume in the combustor is increased, which pushes more sensible energy to the lower temperature region. Since, the conversion efficiency of thermal energy to electrical energy is a function of the temperature at which it is integrated in the Rankine cycle [90, 91], a lower flue gas recycle leads to a higher power generation, and therefore higher plant efficiency. A brief comparison of the SPOC process with other oxy-combustion processes using exergy analysis is presented by Hagi et al. [54].

2.5 Economic Analysis

The cost analysis for the SPOC process was performed in collaboration with Burns & McDonnell on the basis of the plant performance and stream tables, by scaling the costs from NETL reports where appropriate and using vendor data otherwise. Process & project contingencies, engineering construction management and home office fees, and owner's cost were included in calculating the total overnight costs. A brief summary of the economic assumptions are provided in Table 2-9. For cost comparison, the reference case was an air-fired, supercritical PC power plant in the Midwest, using PRB coal. The costs for the reference plant were calculated by scaling the costs from the NETL report [92] for Illinois # 6 coal and using the IECM models to obtain scaling factors. The scaling exponents were found from the NETL guidelines [93]. The cost of electricity for the SPOC process was calculated assuming a high-risk finance structure, whereas the baseline was calculated using low risk finance structure (Table 2-10).

Table 2-9. Global economic assumptions

Parameter	Value
Income Tax Rate	38% Effective (34% Federal, 6% State)
Capital Depreciation	20 years, 150% declining balance
Repayment Term of Debt	15 years
Capital Expenditure	5 years
Operational Period	30 years
Economic Analysis Period (used for IRROE)	35 years (capital expenditure period plus operational period)
Capital Cost Escalation During Capital Expenditure Period (nominal annual rate)	3.6%
Distribution of Total Overnight Capital over the Capital Expenditure Period (before escalation)	10%, 30%, 25%, 20%, 15%
Working Capital	Zero for all parameters
% of Total Overnight Capital that is Depreciated	100% (<i>this assumption introduces a very small error even if a substantial amount of TOC is actually non-depreciable</i>)
Escalation of COE (revenue), O&M Costs, Fuel Costs (nominal annual rate)	3%

Table 2-10. Financial structure

Type of Security	% of Total	Current (Nominal) Dollar Cost	Weighted Current (Nominal) Cost
LOW RISK (Capital Charge Factor = 0.116)			
Debt	50	4.5%	2.25%
Equity	50	12%	6%
Total			8.25%
HIGH RISK (Capital Charge Factor = 0.124)			
Debt	45	5.5%	2.475%
Equity	55	12%	6.6%
Total			9.075%

The levelized cost of electricity (LCOE) of the SPOC process with carbon capture was calculated as \$98.5/MWh compared to approx. \$73.05/MWh for a baseline air-fired plant without carbon capture. Thus SPOC process captures carbon dioxide for a 34.8% increase in LCOE. In comparison to atmospheric pressure oxy-combustion and post combustion capture processes, this is more than a 40-50% reduction in increase in LCOE [27, 29-31]. This reduction is mainly due to the reduction

in efficiency penalty by pressurization and fuel-staging. Furthermore, the use of the integrated pollutant removal column also contributes to the capital cost savings by reducing the cost of gas cleanup.

2.6 Conclusions

Staged, Pressurized Oxy-Combustion (SPOC) process, due to fuel staging approach is able to avoid auxiliary loads associated with recycling of large amounts of flue gas for temperature control. This along with significant capture of latent heat from the flue gas and other waste heat from the auxiliary systems at high pressure resulted in a net plant efficiency (HHV) of 35.7% when using subbituminous PRB coal and 36.7% when using bituminous Illinois #6 coal.

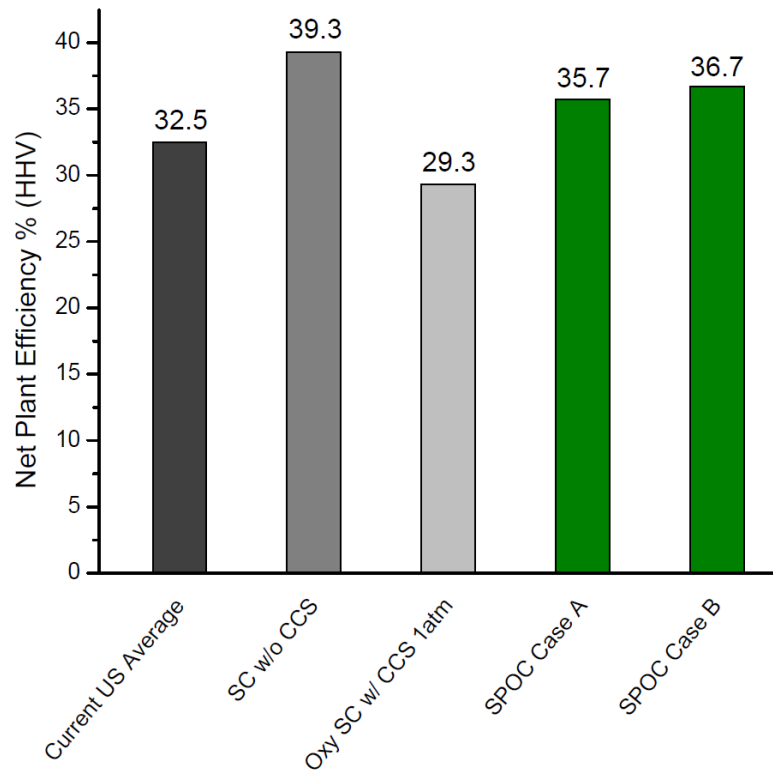


Figure 2-4. Comparison of net plant efficiencies for various cases. (SC: Supercritical. Both SPOC cases are supercritical).

The penalty in plant efficiency due to carbon capture is reduced from 10 percentage points in the atmospheric pressure oxy-combustion plant (as reported by DOE/NETL) to about 2.6 percentage points due to the SPOC process. The average efficiency for coal based power production efficiency in the United States is currently 32.5% (HHV)[94, 95]. This suggests that the SPOC process has a potential to increase the average efficiency of coal based power generation even with carbon capture, in contrast to the conventional carbon capture processes in the U.S. (Figure 2-5). The significant reduction in efficiency penalty also helps reduce the economic penalty for carbon capture by approximately 50%, making SPOC an attractive process for power generation with minimal CO₂ emissions.

Chapter 3

Parametric Analysis of Staged, Pressurized Oxy-Combustion

3.1 Introduction

In Chapter 2, the efficiency and cost of the SPOC process were shown to compare quite favorably to other oxy-combustion approaches for power generation with carbon capture. The analysis of the SPOC process was based on a given operating pressure, fuel-moisture content, and flue gas recycle ratio (~ 5%). From a process perspective, the pressure was chosen to ensure proper operation of the DCC for integrated pollutant removal and flue gas moisture condensation, without the use of any moving parts between the boilers and the DCC. There are other considerations, such as a minimum pressure requirement to create an optically dense boiler, the advantage of which will be discussed in Chapters 4–6. The optimal pressure for pressurized oxy-combustion has been studied for two different systems—one developed by Babcock Power and Thermo-Energy [96], and the other, a flameless combustion system, developed by ITEA and ENEL [41]. Pressures ranging from 6 bar to 80 bar have been considered, and the optimal pressure has been found to be system dependent [41, 84, 96, 97]. The optimal pressure for the high recycle processes are strongly limited by the need to maintain sufficient velocity without significant pressure drop [41]. This is primarily

because, with increased flue gas recycle and a given furnace exit temperature, the proportion of radiative over convective heat transfer to the steam tubes decreases. With an increased dependence on convective heat transfer—which inherently has a lower heat flux—the gas-side velocity in the heat recovery steam generator must be high to obtain a high convective heat flux. But, this leads to increased pressure drop, and hence auxiliary power requirement, reducing the efficiency. With a high pressure, the density is high, but that leads to a reduced volumetric flow rate, and thereby velocity. The competing effects of increasing velocity by shrinking the size of the heaters, leads to an optimal pressure that is around 6–8 bar.

The SPOC process, on the other hand, is based on a low flue gas recycle concept, with the primary mode of heat transfer being radiative, rather than convective. Thus the pressure drop in the system is much lower than the other processes. Since the optimal operating pressures are system dependent, it is necessary to understand the best operating conditions to maximize the efficiency gain. Furthermore, the understanding of the effect of as-fired fuel moisture is also seen as crucial not only for this process, but for other pressurized oxy-combustion processes as well, because of the assumption of coal-water slurry feeding in other proposed pressurized oxy-combustion processes [48, 50, 96]. In this chapter, the motivation for the selection of 16 bar pressure and surface-dried fuel will be provided.

Another key feature of SPOC—low flue gas recycle—is also investigated in this chapter to understand how plant efficiency varies with flue gas recycle. Since the SPOC process models developed in the previous chapter assume only about 5% flue gas recycle (sufficient for dense-phase transport of coal), the first SPOC boiler will essentially operate with pure oxygen. Though, methods have been developed to control the heat flux in SPOC boilers even with pure oxygen as the fuel [98], other considerations detailed in Chapter 4 could potentially limit the immediate

acceptance of such a configuration in utility boilers. An understanding of the effect of flue gas recycle on the net plant efficiency would provide insights for better process and boiler design.

Finally, some potential areas for process intensification, such as the direct contact column, and the steam Rankine cycle operating conditions are explored to increase the plant efficiency.

The key assumptions and modeling approach used is similar to that described in Chapter 1, and hence is not repeated here. In this chapter, and henceforth, only the sub-bituminous PRB coal (proximate and ultimate analysis provided in Chapter 2) will be used, unless otherwise specified. The choice of PRB coal is due to the low cost and high availability of this coal in the US—accounting for more than 40% of the coal consumed in the US for power generation.

3.2 Operating Pressure

Operating pressure analyses are divided into two different studies – the first analyzes the effect of direct contact column (DCC) operating pressure on moisture condensation and lays the groundwork for the next part, which is to analyze the effect of combustor operating pressure on the net plant efficiency. For the operating pressure analyses, the coal is surface-dried to 24% as-fired moisture.

Direct Contact Column (DCC) Pressure:

For moisture condensation in the DCC, six different flue gas and DCC pressures are analyzed over the range of 10 to 35 bar. All pressures mentioned in this paper have units of bar absolute. Based on equilibrium flash calculations, Figure 3-1 shows the effect of operating pressure on the gas exit temperature of the DCC. The greatest difference is seen between 10 bar and 15 bar, while at higher

pressures almost no difference in moisture condensation is observed, especially at lower exit temperatures. It can be seen that for temperatures less than 50°C, the moisture condensation and heat in the DCC increases by less than 1% when the pressure is more than doubled, beyond 15 bar. At any given exit temperature, the effect of pressure on moisture condensation yields diminishing returns with increasing pressure.

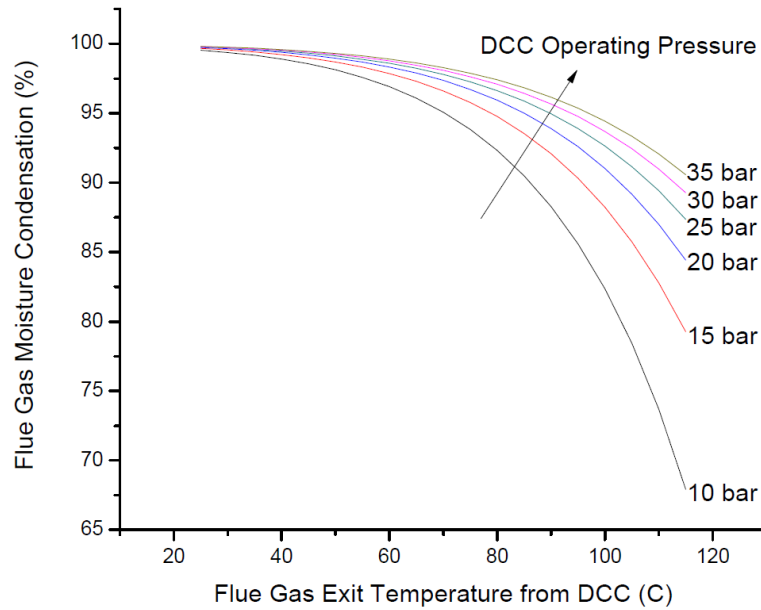


Figure 3-1. Percentage of flue gas moisture condensation at various DCC operating pressures and flue gas exit temperatures from the DCC

Radiant Boiler Operating Pressure:

Since the analysis of the DCC indicates that 15 bar is sufficient to capture a large majority of the latent heat, the minimum operating pressure of the radiant boilers considered in this study is 16 bar, to allow for pressure losses between the boilers and the DCC. Due to the considerations detailed in Chapter 1, and the above paragraphs, the minimum pressure analyzed for the SPOC process is 16 bar (Case P1). In this work, two higher pressures—30 bar (Case P2) and 36 bar (Case

P3)—have been considered. Pressures higher than 36 bar were not considered, even though analyzed by others such as Babcock Thermo [96], due to the limitation of coal feeding by solid pumps at higher pressures.

Case P1 is the same as analyzed in Chapter 1, and the results of the process model have been discussed in detail. Case P1 is the base case for this study, and the corresponding net plant efficiency is 35.7% (HHV). Cases P2 and P3 only differ in the combustion pressure. An increase in combustion pressure above 16 bar increases the net plant efficiency only slightly, and with diminishing returns, as can be seen in Figure 3-2. The difference in net plant efficiency between 16 bar and 36 bar cases is less than 0.14 percentage points. The different contributors to this trend are discussed below.

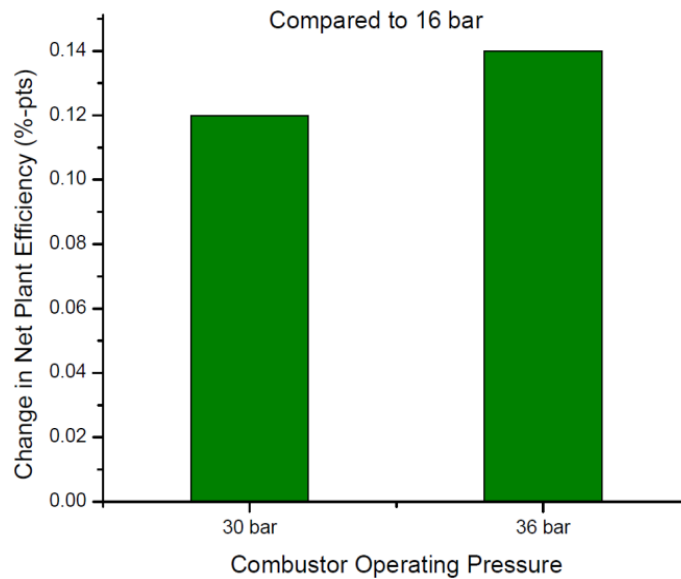


Figure 3-2. Increase in net plant efficiency (HHV) as a function of pressure over Case P1 (16 bar).

The power requirement for oxygen production increases with combustion pressure. Since this increase in power demand is only for increased compression, and since the final flue gas is required

to be compressed up to 153 bar, the CPU power load is reduced. The sum of ASU and CPU power demand, on the other hand, remains relatively constant, between 142–145 MW_e ($\approx 0.09\text{MW}_e/\text{MW}_{\text{th}}$ fuel input), for all three pressures cases.

In SPOC, heat from either flue gas moisture condensation or “waste heat” from auxiliary systems can be integrated into the steam cycle, thereby reducing the steam extraction requirement for regeneration of BFW. As we know, steam extraction for feedwater heating (regeneration) is used to increase plant efficiency of the Rankine cycle, but utilizing the heat from the DCC and the auxiliary systems instead of from the boiler increases the overall (net) plant efficiency.

The bottoms product (subsequently referred to as “bottoms”) of the DCC is hot water along with some (dilute) acids. The temperature of the bottoms of the column is a function of the operating pressure of the column, and increases with operating pressure. This hot water can be used to exchange heat with the Rankine cycle either upstream or downstream of the de-aerator (see Figure 2-3), replacing some of the extraction steam from such locations. As the de-aerator pressure is set at 8 bar, which corresponds to a saturation temperature (and hence BFW exit temperature) of 170°C, the DCC bottoms water temperature is not high enough in Case P1 to allow integration into the Rankine cycle downstream (high-temperature side) of the de-aerator. In contradistinction, for both the higher pressure cases—Case P2 and P3—the exit water temperature is high enough (193°C and 200°C respectively) to allow for partial integration downstream of the de-aerator. As already stated, higher pressure (higher than Case P1) does not increase the amount of moisture condensation significantly (difference between Case P1 and P3 = 0.16 percentage points), but integrating into the high pressure region allows heat transfer from the DCC bottoms water to the Rankine cycle in a larger temperature range. It also reduces the amount of cooling water required in the DCC, from 864 tonnes/h (16 bar) to 690 tonnes/h (36 bar) and hence reduces the rejected

heat after heat transfer to the boiler feed water. In other words, with increasing pressure the amount of heat addition from the DCC increases by approx. 8 MW_{th} (5.3%) from 16 bar to 36 bar (Figure 3-3a). And more importantly, the amount of heat shifted from the LP to the HP region for the 30 bar and 36 bar cases are, respectively, 6.5 MW_{th} and 11.5 MW_{th}.

In this work, the only other auxiliary heat integrated into the Rankine cycle is the heat from oxygen production. As the operating pressure of the combustor increases, the oxygen compression requirement increases. This compression is accomplished with multistage compressors and intercoolers that use low-pressure boiler feed water (LP BFW) for cooling. As the compression requirement increases, the oxygen temperature at the intercooling heat exchangers increases. Thus, more heat can be transferred at higher temperature. As the compression requirement increases further, the stage pressure ratio in the multistage compressor increases significantly, requiring the addition of another stage to keep the compression process efficient. For both 30 bar and 36 bar cases, three stages were required while only two were required in the 16 bar case. Addition of an extra stage reduces the maximum temperature and the temperature range in which heat is available from the oxygen compressors. Thus, the heat from the ASU is restricted in the temperature range suitable for integration with the low pressure BFW only.

Figure 3-3b shows that with increasing pressure, more heat is available from the ASU. The partial shift of DCC heat into the HP region allows the increased heat transfer from the ASU into the steam cycle, thus increasing the net plant efficiency (Figure 3-2). Still, since the temperature at which heat is available from oxygen compression is restricted, the benefit from increasing pressure is quite modest.

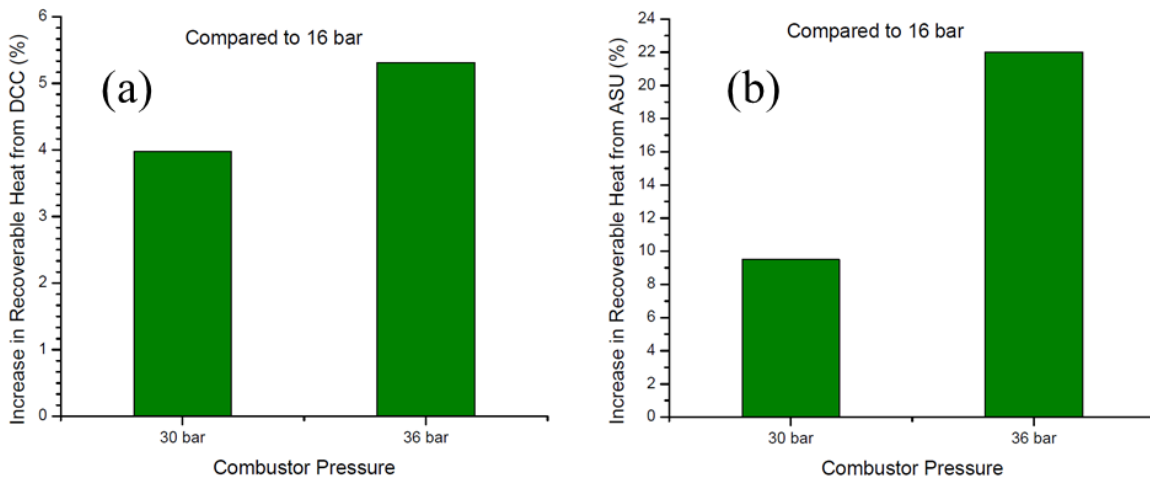


Figure 3-3. Increase in recoverable heat (integration into Rankine cycle) from (a) DCC, (b) oxygen production.

Increasing system pressure has two benefits—first is in increasing the efficiency of the process, and the second is in reducing the size of various units. The first effect has been quantified and discussed above. For the second effect, a brief and qualitative discussion is provided here. Since, the change in efficiency is small with increasing pressure above 16 bar, we will, for ease of discussion, neglect the effect of reduced thermal input for the same power output on size and only concentrate on the reduced gas volumes due to compression. The various units in the SPOC process are the ASU, O₂ compressors, radiant boilers, DCC, CO₂ boost compressor (which pressurizes the clean flue gas to about 36 bar) and the CPU. Of these, the ASU and CPU sizes remain the same since they always operate between the same states: ASU produces 1 bar O₂ from 1 bar air, while the CPU purifies the clean and dry CO₂ and compresses it from 36 bar to 153 bar. The combination of the O₂ compressors and the CPU boost compressor would have similar overall size, since they compress from atmospheric pressure to about 36 bar in all cases. In the higher-pressure cases since the number of compressors increases, and more oxygen compressors are required, the capital cost may increase with increasing pressure. The radiant boilers, on the other hand, are not sized based

only on the gas volumes. The primary purpose of the radiant boilers is to transfer heat to the steam cycle, and their size is dependent on heat transfer surface area requirements, and this size does not reduce proportionally with increasing pressure. On the other hand, the material of construction required will increase with pressure due to an increase in wall thickness of the boilers, even though the overall size may be reduced slightly due to reduced thermal input (higher net plant efficiency). It is important to note, however, that the material of construction only forms a small part of the boiler cost, which is mainly governed by boiler tube costs. The effect of pressure on the design of the DCC is not obvious, though there is potential for size reduction with increasing pressure, both due to the potential increase in performance of the integrated pollutant removal reactions at higher pressure [69, 99, 100] and reduced gas volumes.

3.3 Fuel Moisture Content

In order to feed the coal into the boilers at elevated pressure, a high pressure, dense-phase feeding system (pneumatic dry feeding) has been considered in the process analysis. This process requires that the surface moisture of the pulverized coal be removed for optimal feeding. Further drying to remove some inherent moisture may also be considered. An alternative method to feeding the coal is to feed coal water slurry, which can be readily pumped to deliver the coal at elevated pressure.

For a typical 1 atm coal-fired power plant, it is well understood that increasing moisture content decreases plant efficiency, since the added flue gas volume from moisture results in additional stack loss. However, in pressurized systems, the impact on moisture content is not obvious since a portion of the latent heat associated with flue gas moisture may be recovered. A systematic study on the effect of as-fired moisture on net plant efficiency was performed by studying 6 different

cases with a constant thermal input of 1539 MW_{th}, matching the work in [46]. The as-received coal moisture is 27.42%. Coal drying was considered in three cases: drying to 9.7%, 17% and 24% moisture. The other three cases represent moisture addition to the as-received fuel (30%, 35%, 45%). Other parameters of the process were kept constant. The drying of coal was modeled as being performed by dry nitrogen gas from the ASU. The heat for drying was partly derived from ASU and partly from previously unutilized low temperature heat from CPU boost compressors.

As can be seen from Figure 3-4, the net plant efficiency monotonically decreases with increasing moisture content, but the slope of the curve changes drastically between the low moisture and high moisture cases. In the low moisture cases, low pressure BFW is heated with a combination of auxiliary heat and steam extraction. With increasing amounts of moisture in the fuel, the high temperature sensible heat available from the combustion gas in the radiant boilers and the economizer reduces, whereas the amount of low temperature latent heat available in the DCC increases. Overall, this shift of heat from the higher grade to the lower grade reduces the amount of steam extraction for BFW regeneration. The sum of the heat available from the boilers, economizer and the DCC is constant at low moistures, and so is the heat available from other auxiliary systems like ASU and CPU for a given fuel input. Since the net heat supplied to the steam cycle is constant, but the steam extraction is reduced, the cycle efficiency reduces, as does the plant efficiency. Nonetheless, the reduction in plant efficiency is only slight.

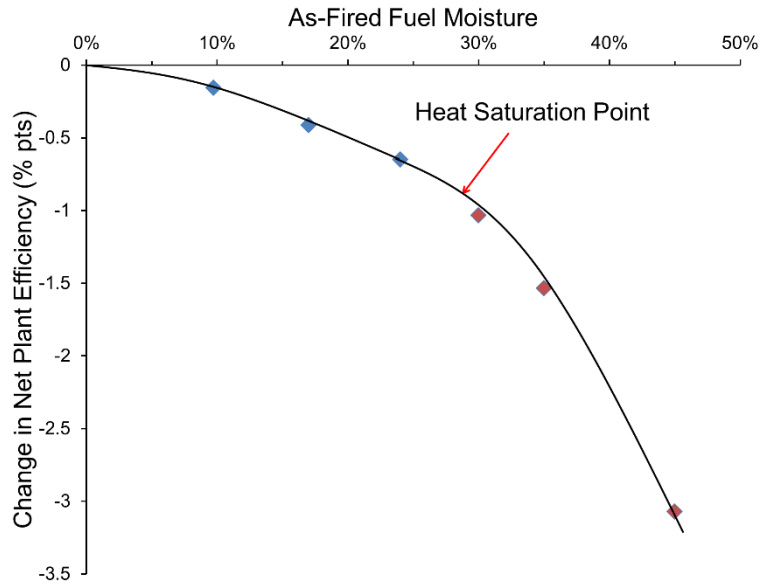


Figure 3-4. Change in net plant efficiency (HHV) as a function of as-fired fuel moisture. Reference is a fully dry fuel.

As the fuel moisture increases further, more heat is available from the DCC for integration and the steam extraction from the LP steam turbine is completely eliminated. This is considered the point of *heat saturation* of the LP BFW. This heat saturation point is around 29% as-fired moisture for the system modeled in this paper. Beyond the point of heat saturation, increasing fuel moisture does not lead to additional heat integration into the Rankine cycle and hence does not affect the cycle efficiency, but the net plant efficiency decreases. This is because at the point of heat saturation, the maximum possible heat is integrated in the low pressure region of the BFW. Even if more heat is made available from the DCC, it cannot be integrated into the steam cycle. The excess heat from the DCC condensate, which cannot be integrated into the steam cycle due to heat saturation, needs to be cooled using cooling water and discarded.

In most conceptual pressurized systems modeled, coal water slurry (CWS) feeding is considered as the standard approach for fuel feeding due to experience and expertise in such feeding for other

purposes, such as coal gasifiers. Furthermore, the pressurized oxy-combustion systems are considered to be more beneficial for low rank coals, as the hitherto unrecovered heat of moisture condensation at lower pressure, can be recovered, potentially making them more efficient. It has been shown above that increasing the moisture content beyond what would lead to LP BFW heat saturation is detrimental to the plant efficiency. The challenges of feeding low rank coal as a slurry are discussed in [101]. In order to pump slurry, the maximum apparent viscosity accepted in the industry is about 1000 mPa-s at 100s⁻¹ [102, 103]. The viscosity of the CWS increases with the hydrophilicity of the coal. Therefore, a hydrophobic coal can more easily be used to form low viscosity slurry at high solids loadings. Normally, high-rank coals are hydrophobic, while low-rank coals are hydrophilic [82]. For high pressure operations, like coal gasification, coal water slurry feeding works well for bituminous coals but not for lower grade coals [104]. Delivering a coal water slurry using PRB coal requires water content as high as 65 wt% in order to make it pumpable [101], which corresponds to more than 3 %-pts. loss in net plant efficiency.

In summary, a steep decrease in plant efficiency occurs when the low-grade heat available through flue gas moisture condensation is sufficiently high such that there is excess latent heat that cannot be integrated into the steam cycle. Thus, slurry feeding of fuel even with high-pressure combustion is not recommended since the as-fired moisture in slurries exceeds this limit for heat saturation in the Rankine cycle. On the other hand, drying the fuel (beyond the minimum requirement for dry feeding) does not increase the efficiency significantly. This result is true for other pressurized processes as well, though the point of heat saturation in the Rankine cycle may occur at different fuel moisture contents.

3.4 Flue Gas Recycle Ratio

Two main configurations for flue gas recycle are considered in oxy-combustion systems—warm gas recycle, and cold gas recycle. For warm-gas recycle, the flue gas is recycled prior to the gas clean-up equipment (in some cases after the filter, but still before the FGD). This increases the sulfur content in the boilers, and is only considered for operation with low sulfur coals. This configuration has a slightly higher efficiency at atmospheric pressure. The cold-gas recycle entails complete gas cleanup, moisture condensation, and then recycling back the flue gas to the boiler.

For the SPOC process, due to high pressure in the boilers, warm-gas recycling could lead to very high SO_2 and SO_3 concentrations, and from a conservative point of view this configuration is not considered here. In the cold-gas recycle configuration on the other hand, the flue gas passes through the DCC before being recycled back. As the DCC is a direct contact heat exchanger, the heat transfer is not efficient from an exergetic perspective. The temperature of the flue gas for recycling is reduced to about 38°C . Flue gas recycling also increases the volumetric flow in the combustor and pushes a significant amount of sensible energy downstream to lower temperature regions. The conversion of thermal energy to electrical energy from the lower temperature regions (DCC) is much less efficient compared to what could be achieved from the high temperature regions (combustor / economizer). Therefore, during recycling, a lot of energy is wasted leading to reduced efficiency. Figure 3-5 shows the net plant efficiency as a function of flue gas recycle ratio.

As can be expected, increasing flue gas recycle increases the efficiency penalty, with 70% recycle (conventional flue gas recycle ratio) resulting in an efficiency penalty of almost 4 percentage points. However, the relation of flue gas recycle with efficiency is not linear, and most of the

efficiency is penalized in the flue gas recycle ratio range of 33% to 70%. Below 33% of flue gas recycle, the efficiency loss is less than 1 percentage point.

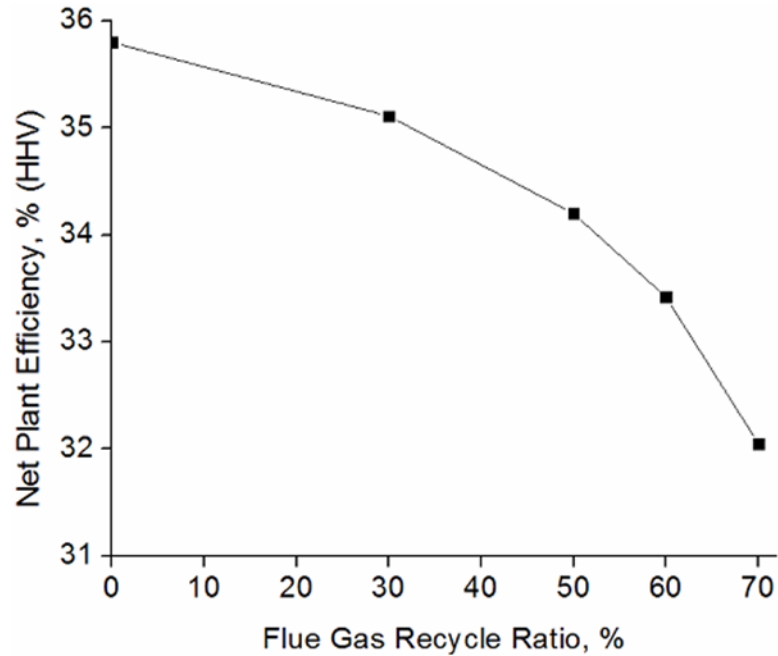


Figure 3-5. Effect of flue gas recycle ratio on the net plant efficiency (HHV) in the SPOC process

3.5 Process Intensification and Advanced Rankine Cycles

Process intensification in staged, pressurized oxy-combustion can be achieved by the modification of the flue gas condensing heat exchanger from a low efficiency direct contact column, to a more efficient indirect contact heat exchanger. Modifications to the Rankine cycle, in line with the latest industrial advancements, such as a double reheat steam cycle or advanced ultra-supercritical Rankine cycle would also help increase the plant efficiency. In this section, the results from such intensification or cycle modification are presented.

Indirect Contact Heat Exchanger for Flue Gas Moisture Condensation:

The direct contact column used in the SPOC process provides a practical means of condensing the flue gas moisture, while minimizing the impact of the acids that would condense along with the moisture. In the DCC, due to the very large amount of water added for cooling, the acids are diluted. Furthermore, since the heat exchange is not through the surface of the contacting column, the material of construction can be made acid resistant at low cost. However, the process is highly inefficient in terms of heat transfer. The raw hot flue gas enters the DCC at approximately 330°C, and the maximum temperature of the hot water from the DCC used for heat exchange with the boiler feed water is at 165°C. This represents a significant loss in availability (exergy). An indirect contacting heat exchanger could be used instead of the direct contact column to capture this availability. The flue gas at the outlet of this indirect heat exchanger can be designed to enter the DCC at a low temperature for an efficient integrated pollutant removal (~ 46°C). The indirect heat exchanger would be exposed to very high acids concentration (acid dew point is higher than moisture dew point), and hence would require expensive materials of construction. For the SPOC process, the gain in net plant efficiency when using an indirect heat exchanger is approximately 0.55 %-pts. This analysis provides a basis for cost-benefit analysis for the utilization of such a heat exchanger.

Advanced Rankine Cycles:

Advances in the development of materials and turbo-machinery have allowed two primary modifications in the design of Rankine cycle to further increase efficiency—double reheat of steam, and higher steam temperature and pressures (USC and AUSC cycles). Similar to the indirect heat exchanger for flue gas moisture condensation, the implementation, or lack thereof, of these process intensification measures is dictated by the economics. However, in this section, only the performance improvements through such process intensification are discussed. The cycle

conditions for the different configurations studied are presented in Table 3-1. In the cases of double reheat, the steam temperature at the outlet of the second reheat is maintained the same as in the first reheat. In all the cases, a direct contact column is considered for flue gas latent heat recovery. Only the cycle conditions are changed, while the coal properties, site conditions, etc. are maintained the same as described in Chapter 2.

Table 3-1. Steam conditions for the various Rankine cycles considered

Condition	Main Steam Pressure (bara)	Main Steam Temperature (°C)	Reheat Steam Temperature (°C)
SC	242	593	593
Ultra-Supercritical (USC)	277	690	690
Advanced USC (AUSC)	277	732	732

The results for the sub-bituminous PRB coal are shown in Figure 3-6. For all steam conditions shown in Table 3-1, adding a second reheat leads to approximately 1.5 %-pts. increase in net plant efficiency. Whereas, increasing the steam temperature and pressure from that for SC to AUSC can increase the efficiency by almost 3 %-pts. Overall, the highest efficiency of 40.64% is obtained by using an AUSC steam cycle with double reheat. If a higher rank coal, such as the Illinois #6 coal described in Chapter 2 is considered, the net plant efficiency is approximately 41.4%. These efficiencies are 25–30% higher than the current U.S. average, as shown in Figure 2-5.

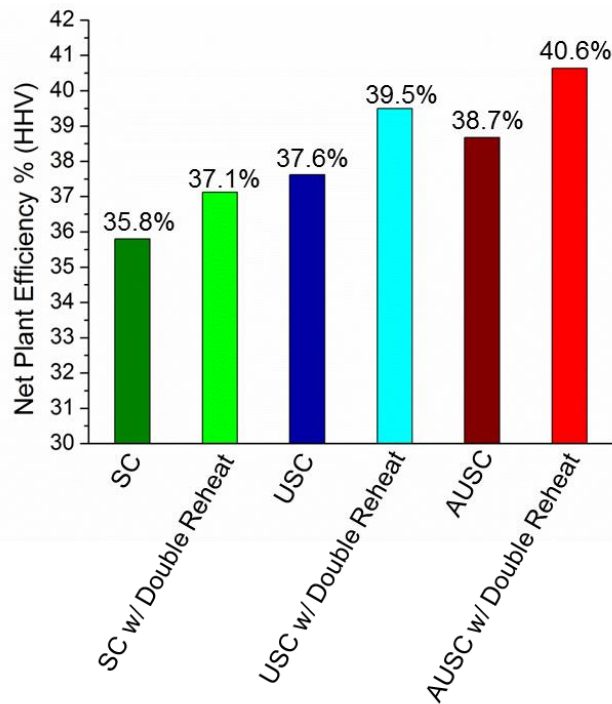


Figure 3-6. Net plant efficiencies when using different steam temperatures and pressures, and number of reheats in the Rankine cycle of the SPOC process.

3.6 Conclusions

In this chapter, parametric analyses on the effects of combustor operating pressure and fuel moisture were performed for a fuel staged, pressurized oxy-combustion power plant. It was found that combustor pressure has only a minor impact beyond 16 bar. At higher pressures, the increase in pressure leads to a negligible increase on the amount of flue gas moisture condensation and only a small increase on the heat available for integration with the Rankine cycle. But, its ability to partially shift the location of the heat integration to the HP region of the Rankine cycle from the LP region, along with a small increase in the heat available from the ASU, results in an increase in the net plant efficiency. In the range of pressures considered, although the net plant efficiency increases, the increase is quite modest (~ 0.14 percentage points) for the significant increase in

combustor operating pressure (pressure is more than doubled in the range considered). Overall, the economic gain or loss due to further pressurization will be case dependent. The fuel cost, fuel moisture, sulfur and nitrogen in fuel, etc. will play a role in determining on a case-by-case basis the optimal pressure. Based on this analysis, though, it is expected that the optimum would be around 16 bar.

When compared to an atmospheric pressure oxy-combustion system the plant efficiency increases for the high-pressure combustion systems for all moisture contents. But, if the as-fired moisture content of the fuel is increased, the gain in efficiency will reduce. This is an important observation, especially when slurry feeding is considered for high pressure operation, and when working with low rank coals or lignites, which require a large amount of water for slurry feeding. Operating with as-fired moisture lower than what would cause heat saturation in the low pressure regenerators is recommended. This in almost all cases translates to dry or surface-dry feeding of coal.

Similarly, the non-linear dependence of net plant efficiency on the flue gas recycle ratio provides some room for recycle without significant loss in efficiency. Flue gas recycle upto a recycle ratio of 33% results in an efficiency penalty of less than 1 %-pts. This has implications in addressing other burner design constraints, as will be highlighted in Chapters 4 and 5.

Finally, process intensification through indirect heat exchangers, instead of a direct contact column for flue gas moisture latent heat recovery, and advanced steam Rankine cycle can increase the plant efficiency. The indirect heat exchanger can increase the efficiency by 0.55 %-pts., whereas the advanced ultra-supercritical Rankine cycle with double reheat will result in about 4.5 %-pts. higher efficiency than the supercritical, single reheat Rankine cycle considered in Chapter 2.

Chapter 4

Introduction to Burner and Boiler Design for Low-Recycle Pressurized Oxy- Combustion

4.1 Introduction

In the previous two chapters, the process design and parametric analysis of the SPOC power plant were discussed, with an emphasis on the net plant efficiency. It was assumed that such a low flue gas recycle oxy-combustion boiler could be designed and operated at high pressure. This chapter presents a brief discussion on the primary design considerations for such a boiler, and the burner therein.

Boiler walls are made up of tubes carrying water/steam at very high pressures (up to 250 bar). In a supercritical steam cycle, the high pressure water/steam is heated in the boiler to become a supercritical fluid at high temperature and pressure, and is then expanded in a turbine to produce electricity. Since the boiler tubes are under high pressure, significant care is required to not exceed their temperature constraints. A very high wall heat flux could lead to a boiler tube temperature that is above its limit, resulting in tube failure. In air-fired conditions, the heat flux is below the maximum permissible value, due to the low flame temperature caused by the large amount of inert (N_2) in air. On the other hand, the combustion of coal with pure oxygen could result in an adiabatic

flame temperature as high as 3000 K, leading to excessively high heat flux. The primary method of controlling wall heat flux in first generation oxy-combustion is through the control of flame temperature by recycling a large quantity of flue gas [39, 105]. Reducing flue gas recycle has, therefore, traditionally been considered to pose risks and has been avoided.

Nonetheless, reducing flue gas recycle has received interest recently due to its impact on plant efficiency. Furthermore, reducing flue gas recycle increases the portion of heat transfer to the furnace wall that is due to radiation, as opposed to convection [57]. Since radiative heat flux from a flame is usually higher than convective heat flux in power plants, reducing flue gas recycle can reduce the amount of boiler tube materials required, thereby reducing capital costs. A few combustor designs have been proposed for reduced recycle [55-57, 106], however, as Kobayashi and Bool [55] have noted, these were only demonstrated for industrial furnaces or for boilers with low thermal input and low temperature and pressure steam, where much higher heat fluxes can be handled than in a typical utility-scale boiler. None of these designs have been demonstrated for utility-scale boilers, due to the inability to control wall heat flux within manageable levels.

4.2 Boiler Design Considerations

In most traditional boilers, the fuel and oxidizer are supplied at the bottom of a large rectangular boiler and are rapidly mixed, usually by generating a swirling flow, to react the two streams and release heat. This configuration has many disadvantages for pressurized, low recycle combustion and the subsequent discussion will address why a radical departure from traditional combustor/boiler design is required for SPOC. For example, swirling motion has many disadvantages when designing a low recycle boiler where the flame temperature is higher than

typical. First, the swirling motion invariably pushes the flame towards the wall—potentially leading to flame impingement. Swirling also throws large particles to the wall, and for a boiler with a very high temperature flame, the particles can be molten, and swirling would invariably lead to a high level of slagging on the boiler tubes. Finally, rapid mixing could lead to an excessively high heat flux in the near-burner region because of the high flame temperature. These issues, and others, will be addressed in the SPOC design.

Another important difference for the design of a pressurized combustion system is that the standard design for a pressure vessel is a cylindrical shape and, thus, the aspect ratio is considerably larger in a pressurized boiler compared with the typical rectangular shape of an atmospheric-pressure boiler. This high aspect ratio will be an important factor in all of the subsequent design considerations.

As noted in Chapter 2, the plant efficiency of SPOC is very high due to pressurized combustion and minimal recycle, but the flame temperatures for the initial stages can be very high. The high flame temperature presents a number of challenges, such as excessive wall heat flux and slagging, which will be addressed in the SPOC design. To avoid flame impingement and slagging on the walls requires that swirl be minimized, and a high level of symmetry be maintained throughout the pressure vessel. To maintain axisymmetric flow, buoyancy dictates that the pressure vessel and burner be oriented vertically. This is very different from the traditional atmospheric-pressure boilers, which are typically up-fired, with the burners placed horizontally on vertical walls. For SPOC, the axisymmetric burner arrangement is preferred, with the burner down-fired from the top of the cylindrical pressure vessel. Down-firing from the top (as opposed to up-firing from the bottom) avoids the possibility that ash/slag build-up will fall on the burner.

A number of factors must be considered to avoid excessive heat flux, but a more fundamental question with respect to heat flux in the pressurized system is how to ensure high, but not excessive heat flux throughout the length of the long, narrow (high aspect ratio) pressurized boiler. A high average heat flux over the length of the boiler will minimize boiler tube surface area, and lead to a reduction in capital costs for the plant. As will be shown, with proper design for SPOC, a high radiative heat flux can be maintained throughout the boiler. This is assisted by ensuring slow mixing between the fuel and the oxidizer, so that the heat release can be distributed over a longer length of the boiler. Once again, this shows a fundamental difference between pressurized combustion and traditional boiler combustion, where rapid combustion and heat release are required. As an example, in Figure 4-1 [107] the heat flux profile for coal burning in pure oxygen in a swirl-stabilized, rapidly mixed combustor is compared with that of an axial jet flame with the same coal and oxygen feed rate. The swirl-stabilized flame leads to rapid mixing and heat release, which leads to a sharp peak in heat flux as well as flame impingement, whereas the axial jet flame has a more distributed heat release and no flame impingement, leading to a more distributed wall heat flux.

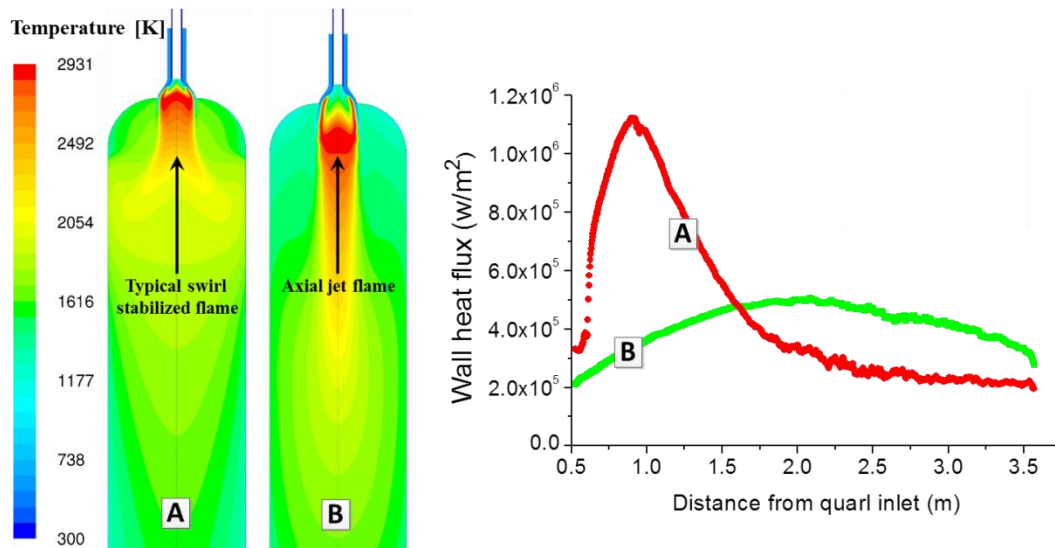


Figure 4-1. A comparison of a swirl-stabilized and an axial jet flame of coal combusting in pure oxygen. Temperature contours in false colors are shown on the left, and the corresponding wall heat flux profiles are shown on the right. Figure reproduced from Xia et al. [80].

While the axial jet flame has a lower mixing rate than the swirl-stabilized flame, it does not intrinsically represent a low-mixing system. To minimize mixing, a low relative velocity between the fuel and the oxidizer is needed because in an axial flow system, near-burner mixing is controlled by the relative velocity between the streams. Furthermore, if such a system can be designed, while at the same time avoiding recirculation, there would be no mean velocity towards the wall. The lack of mean radial velocity would reduce the rate of deposition on the wall by an order of magnitude, due to the elimination of inertial impaction [108]. Fuel-staging, as discussed in Chapter 1, leads to a higher gas flow than the stoichiometric amount required by the fuel in that stage. This larger gas flow can also act as a shroud to reduce particle deposition on the walls. However, for the small number of particles that still penetrate the boundary layer and reach the wall, due to eddy-impaction or thermophoresis, the shroud gas can be used to cool them enough to avoid slagging [108].

External recirculation can be avoided by controlling the Thring-Newby parameter [98, 109]. Still, in a high-temperature down-fired flame, buoyancy could lead to internal recirculation. Depending on the size and location of the internal recirculation, the volatile flame shape could significantly be altered. A much shorter and bulkier volatile flame could result, leading to flame impingement and therefore a very high heat flux. For illustration, a false-color temperature contour from simulation of a case with buoyancy is compared to a case without buoyancy (body-force set to zero) in Figure 4-2.

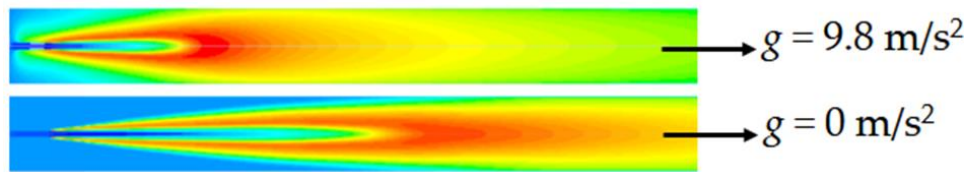


Figure 4-2. Temperature contours for a case with buoyancy (top) and a case without buoyancy (bottom).

Finally, even if flame-impingement could be avoided and a distributed heat release achieved, since the adiabatic flame temperature in this system will be very high, the wall heat flux could also be very high. To control the wall heat flux in such low-recycle systems, the burner and boiler can be designed to utilize radiative trapping. Detailed discussions on the fundamentals and the potential applications of radiative trapping are presented in [110, 111]. In the next section, only a brief and simplified overview of the concept is given.

4.2.1 Radiative trapping

Radiative trapping, in the present context, is a means of controlling radiative heat flux to the boiler tubes. It is illustrated in Figure 4-3, which shows a boiler with high temperature in the central core

region and low temperature near the walls. In the figure, the optical thickness from the wall, $\tau_w(x)$, is a measure of the opaqueness of the medium between any location, x distance from the wall, and the wall. It is calculated by integrating the local extinction coefficient of the medium, $k_e(x)$ over the radiation path length, $\tau_w(x) = \int_0^x k_e(x)dx$. The extinction coefficient is defined as the inverse of the distance that radiation travels in a medium before it is scattered and/or absorbed. Obviously, τ_w increases from zero at the wall to a higher value when approaching the axis of the boiler. A medium is considered optically dense when τ_w is much larger than 1, because the radiation penetration depth [112] would be much smaller than the physical distance to the wall from this location.

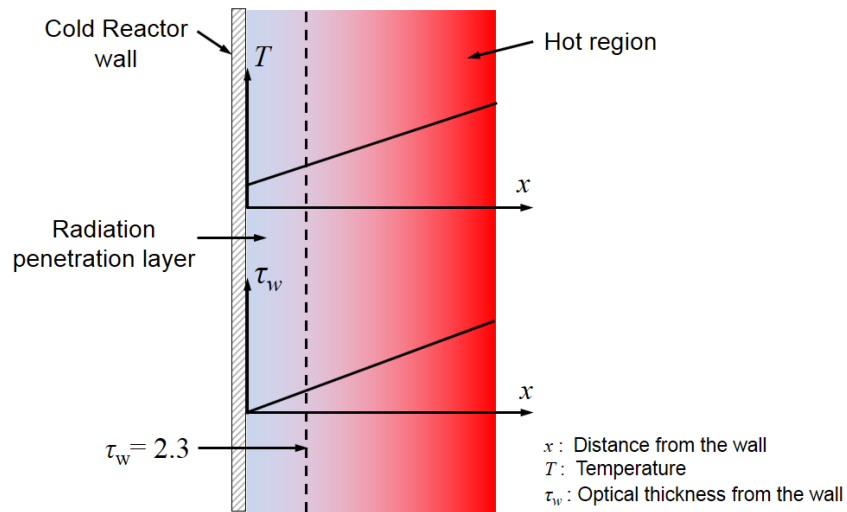


Figure 4-3. Illustration of radiative trapping

Based on Beer's law, the transmissivity of a medium with an optical thickness, τ_w , is given by $\exp(-\tau_w(x))$ [113]. A greater optical thickness leads to less transmission of radiation through the medium. For example, if τ_w is 2.3 at a certain location, the transmissivity between this location

and the wall is about 10% ($\approx e^{-2.3}$), meaning that of all the incident radiation reaching this location, only 10% passes through towards the wall. The rest is either absorbed or scattered by particles within the medium. In such a situation, even if the local emission in the system is very high, especially in regions where both the temperature and the number of emitters (particles) are very high, the incident radiation at the wall is independent of the high local emission, provided that the emission occurs $\tau_w > 2.3$ away from the wall. Instead, it is mainly dependent on the temperature and medium properties between the wall and the location where τ_w is 2.3. This region is termed the “radiation penetration layer” (see Figure 4-3). Thus, if a burner and boiler can be designed so that the medium inside the boiler is optically dense and the temperature in the radiation penetration layer is low, the wall heat flux will also be low, irrespective of the temperature in the core of the boiler.

An optically dense medium can be created by increasing the extinction coefficient of the medium. In a particle-laden medium, the local extinction coefficient of the medium is given by [113]

$$k_e(x) = \sum_i N_{p,i}(x) Q_{e,i}(x) \frac{\pi}{4} d_{p,i}^2(x) \quad (4-1)$$

where N_p , Q_e , and d_p are, respectively, the particle number concentration, extinction efficiency factor, and diameter of particle of size i . A larger particle number concentration leads to larger extinction coefficient, but, for most standard boilers, where the optical thickness is low enough that the medium is optically thin, increasing the particle concentration of the medium increases the number of emitters and thus the heat flux to the wall. Consequently, from a conventional radiation perspective, a high particle number concentration leads to a high wall heat flux.

However, in a low-recycle, pressurized oxy-combustion system, the particle number concentration could be increased significantly due to the combination of high pressure and low dilution gas

volume, such that the medium is extremely optically thick, i.e., optically dense. Such a medium can then effectively trap a significant portion of the radiation emanating from the core of the boiler. With proper burner and boiler design, where the temperature is low in the radiation penetration layer, these boilers can utilize radiative trapping, instead of flue gas recycle, to control wall heat flux.

Note that radiation is also trapped in other pressurized systems, such as gasifiers. While these systems are not specifically designed to control wall heat flux, the heat transfer is modeled as conduction rather than radiation due to the high extinction coefficient in these systems [114-116].

4.3 Burner and Boiler Constraints

Xia et al. [98], using computational fluid dynamics (CFD) simulations, showed a design for the SPOC boilers where, even at very low flue gas recycle, the wall heat fluxes for all stages were controlled to manageable levels for utility-scale applications using radiative trapping. In the design, the fuel was staged into four boilers, while all the oxygen was supplied to the first stage, creating highly over-ventilated initial stages. After combustion of the fuel in the first stage and sufficient cooling by heat transfer to the boiler tubes, the exhaust gas—which still contained a high oxygen concentration—was fed to the next stage where more fuel was injected and some of the oxygen was consumed. This process was repeated until almost all the oxygen and all the fuel was consumed. In this system, the flue gas recycle was only about 5% of the total exhaust gas, and was required only for the dense-phase transportation of the fuel [46].

Though conceptually the design of Xia et al. [98] shows that the wall heat flux can be controlled using radiative trapping even for negligible flue gas recycle, certain practical constraints might limit the use of such a design. Primary among them is the high oxygen concentration next to the boiler tubes. For example, in Stage 1 of the design, the oxygen concentration next to the boiler tubes could be as high as 100%, creating a risk of metal fires if an ignition source—such as an impacting ash particle—is present. Thus, to provide a safe operating condition, the oxygen concentration next to the wall must be constrained to a pre-defined maximum, dictated by the application—utility boiler or industrial furnace. A new burner design will be presented in Chapter 5, which satisfies the constraints presented herein.

An additional challenge faced by the power generation industry is the need to respond to increasing variability in demand due to the increased market penetration of renewable energy sources. Coal and combined cycle gas power plants, which were historically considered base-load generators and required minimal cycling, are now being subjected to significant and deep cycling. New plants must be designed to operate at various reduced plant loads, i.e., turndown [117, 118]. The impact of flexible operation on carbon capture plants has been studied from the perspectives of both process and boiler operation [119-124]. Stanger et al. [39] discussed the preferred characteristics of new power plant designs and indicated that a stable turndown to 40% thermal load is desirable for the burner and boiler. Impact of turndown on the wall heat flux in such a low recycle, pressurized oxy-combustion boiler will be studied in Chapter 6, and modifications to the design of Chapter 5 will be presented in for improving the flexibility of the boiler.

Finally, for a high temperature co-axial flame with a long flame length, there is a high potential to form and emit large amounts of soot. Higher pressure further increases the sooting tendency. Large amounts of soot could significantly change the radiative characteristics in the boiler, and if

unburnt, it would also lead to loss of boiler efficiency. Any unburnt soot could also deposit on heat transfer surfaces, reducing their efficiency. In coal combustion, soot is generated during the devolatilization, wherein due to the envelope nature of the volatile flame—similar to gas flames—a reducing environment is created, and the oxygen deficiency promotes tar and soot formation. There are two ways to deal with soot in such systems—prevent its formation in the volatile envelope, or burn it off immediately downstream of the flame. A method of controlling soot formation in high temperature turbulent flames is presented in [58] and Appendix B, with a detailed discussion on the affected chemical mechanisms. In Chapter 7, a simplified discussion on the soot formation and emission from the burner configuration presented in Chapters 5 and 6 will be presented.

4.4 Conclusions

The basic design considerations for the SPOC boilers were laid out in this chapter. Limitations of the conceptual boiler design of Xia et al. [98] were discussed. The next three chapters will address the three main considerations for a practical SPOC boiler design, *viz.*:

- (a) Control of the oxygen concentration next to the boiler walls.
- (b) Enhanced operational flexibility.
- (c) Control of soot in an axial flow low-recycle oxy-combustion system.

Chapter 5

Burner Design and the Effect of Mixing

5.1 Introduction

As discussed in the previous chapter, the boiler design of Xia et al. [98] had a very high oxygen concentration next to the boiler walls in the initial stages. The current chapter will discuss a new burner that can reduce the maximum oxygen concentration next to the boiler walls, while still maintaining a low flue gas recycle. Certain modifications to the process will also be discussed, where with little loss of efficiency, the complexity of the process can be further reduced.

5.2 Process Modification—Reduction in the Number of Stages

The design presented in Gopan et al. [46] and Xia et al. [98] focused on a 4 stage SPOC process with very little flue gas recycle. However, as discussed in Chapter 4, the oxygen concentration next to the boiler tubes might need to be controlled to a pre-defined maximum from a safety perspective due to the high temperature environment in the boiler. To control the near-wall oxygen concentration, some amount of flue gas recycle would be required. The objective is to keep the

amount of flue gas recycle sufficiently low, such that the loss in efficiency associated with the recycling of flue gas is not large. In Chapter 3, the effect of cold recycle of flue gas on the net plant efficiency was presented. It was seen that the efficiency penalty for recycling flue gas is very small for recycle ratios less than 33%.

If some flue gas recycle is used in the process, further simplification of the process is possible by reducing the number of stages from four to, say, three. A simplified process flow diagram for this is shown in Figure 5-1. In this process, flue gas recycle would only be required in stage 1 to control the oxygen concentration next to the wall. The near-wall oxygen concentration of the other stages would be controlled using the products of combustion from the previous stage. The smaller number of stages, and the burner modifications presented in this paper, significantly reduce the complexity of the process and provide additional control on the amount of oxygen and its inlet concentration for each stage. Furthermore, with the new design, each stage can be supplied with some amount of pure oxygen through a central tube to enhance the combustion characteristics, such as ignition and flame stabilization, as well as reaction rates due to multiple flame fronts, as discussed in section 5.5. Using computational fluid dynamics (CFD) simulations, the effects of various design parameters on the fluid dynamics, and thereby the wall heat flux in a pressurized boiler are investigated. The principles developed here can then be utilized to design low recycle, pressurized oxy-combustion burner/boilers, where wall heat flux is controlled by flame shape and radiative trapping rather than by large amounts of recycled flue gas.

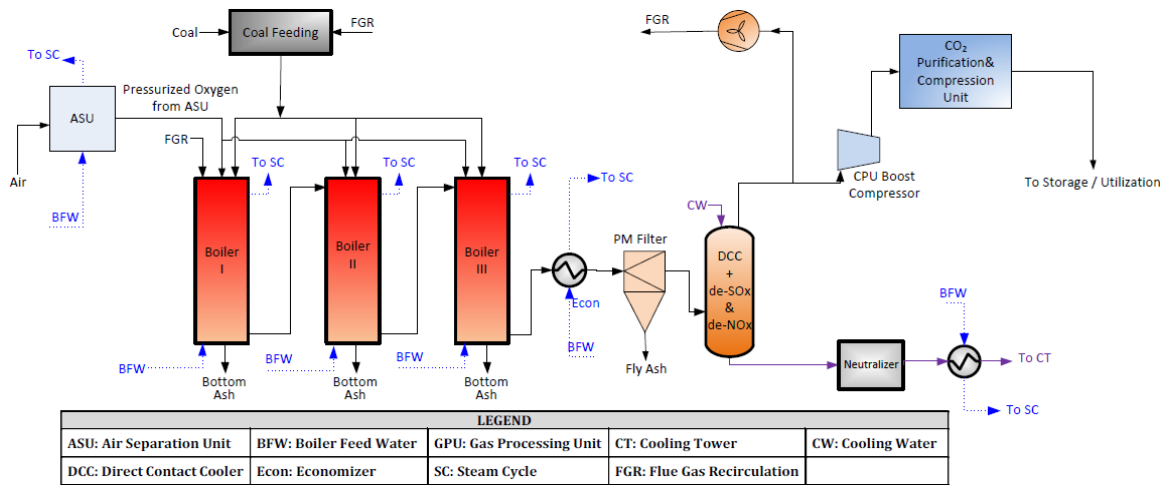


Figure 5-1. Simplified process flow diagram for a three-stage SPOC power plant.

5.3 Burner Design

In these high temperature, vertical, pressurized boilers, to minimize the effect of buoyancy, which could negatively impact flame shape and wall heat flux, the initial section of the boiler is designed as the frustum of a cone, as shown in Figure 5-2. This helps in maintaining a low Richardson number (i.e., low natural convection relative to forced convection) throughout the flame region. The effectiveness of such a cone-shaped boiler in avoiding buoyancy-induced recirculation has been demonstrated in Xia et al. [98] and Gopan et al. [125]. The Richardson number is low at the burner head because the small cross-sectional area of the conical design yields a high velocity. As the flow moves downstream, the cross-sectional area increases, but the volumetric flow rate of the gas also increases, because as the coal devolatilizes and combusts, both the moles of gas and the gas temperature increase. The cone angle of the boiler is designed by matching the increasing volumetric flow rate of the gas with the increasing cross-sectional area. The axial profile of the mass-averaged mean velocity for the base case (discussed later) is shown in Figure 5-3 to

demonstrate the effectiveness of the conical design in maintaining a relatively uniform, high velocity throughout the flame region.

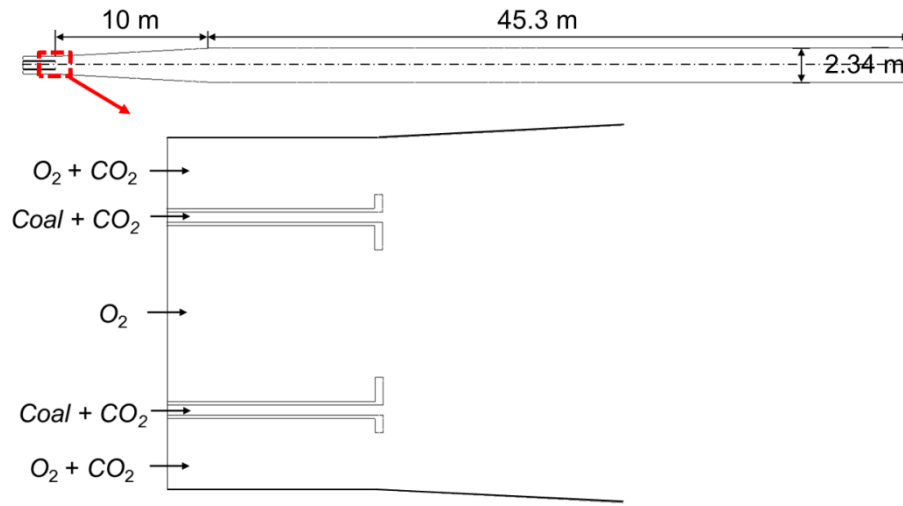


Figure 5-2. Geometry of the burner and the boiler.

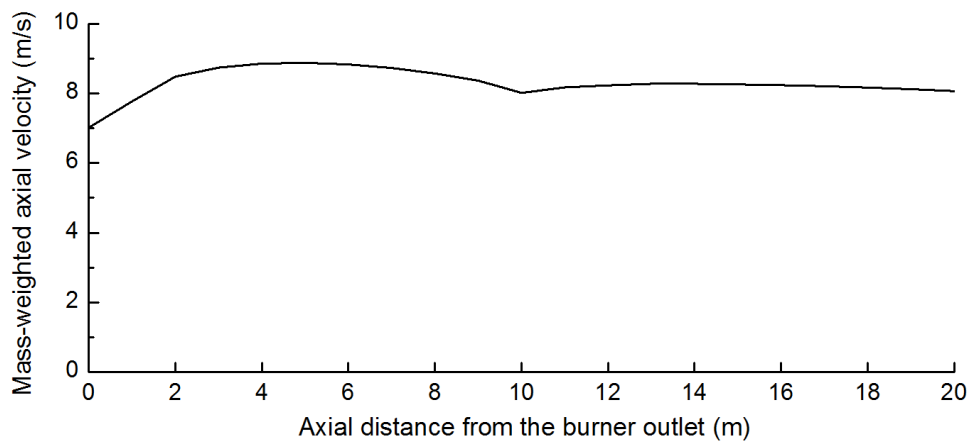


Figure 5-3. First 20-meter axial profile of the mass-averaged mean velocity in the boiler.

To provide a safe operating condition, with the oxygen concentration next to the wall constrained to a pre-defined maximum, while still maintaining a low flue gas recycle, the burner design, shown in Figure 5-2, incorporates a central pure oxygen stream surrounded by fuel in an annulus, which

is further surrounded by a secondary oxidizer (SO) with an oxygen concentration that can be varied. In this study, as an example, the SO oxygen concentration is held constant at 35 vol.%, which is similar to the SO oxygen concentration in first generation oxy-combustion. Circular rings are included on the nozzle ends on both the surrounding oxidizer side and the central oxygen side of the fuel annulus to assist with flame holding. These rings trip both oxidizer flows at the burner exit and cause small localized recirculation zones at the burner, which enhances flame stability, resulting in predicted flame attachment for a wide range of flows, including all flow conditions modeled in this study. The first 2 m of the boiler wall is refractory and is modeled as adiabatic.

It is important to note that this design with inner oxygen is quite different in both intent and implementation from the oxygen lance used in some other atmospheric pressure oxy-combustions burners. In the atmospheric pressure systems, an oxygen lance stabilizes the flame at the burner tip and incrementally improves boiler efficiency. In such systems, the amount of oxygen used is less than 5% of the total oxygen required for the fuel [126]. In contrast, the amount of oxygen supplied from the inner tube in the SPOC burner is substantial and can even be more than the oxygen required for stoichiometric combustion of fuel in that stage. Furthermore, since the pure oxygen stream in the center is surrounded by a large number density of fuel particles, the radiation from the flame is trapped and only a portion reaches the wall, thereby controlling wall heat flux even with reduced recycle. Finally, the surrounding oxidizer (SO) can be used to create a “buffer layer” between the flame and the wall, thus maintaining a low temperature inside the radiation penetration layer for a long distance, and enhancing the effectiveness of radiative trapping. To the best of the authors’ knowledge, this approach has hitherto not been explored.

There are any number of ways in which the flows of fuel and oxidizer in the three stages can be distributed. To maintain a relatively low oxygen concentration near the boiler walls, some flue gas

recycle is required in the first stage, with the later stages using the exhaust gases from the previous stage to maintain a relatively low near-wall oxygen concentration. The flue gas recycle ratio is thus inherently a function of the oxygen concentration in the SO flow in the first stage. For a given SO oxygen concentration and total fuel amount, assigning less fuel in the first stage would lead to a smaller flue gas recycle ratio. For a SO oxygen concentration of 35%, even with an equal distribution of fuel between the stages, the amount of flue gas recycle required is only 33%. This SO oxygen concentration is similar to the oxygen concentration in first generation oxy-combustion processes which utilize about 70% of flue gas recycle. Thus, the same near-wall oxygen concentration can be maintained with less than half the amount of recycle incorporated in first generation approaches. Process calculations show that under these conditions the effect on net plant efficiency is small (less than 1 %-pt.). In practice, the process configuration could utilize a deeper staging, resulting in a still smaller flue gas recycle.

PRB coal is assumed for this study, with the proximate and ultimate analyses provided in Table 5-1. The coal thermal input to the stage is $385 \text{ MW}_{\text{th}}$, and is carried by a 1.2 kg/s stream of CO_2 . The inner oxidizer is pure oxygen with a flow rate of 21.7 kg/s for the base case, corresponding to 78% of the total oxygen required for the fuel in this stage. The flow rate of the surrounding oxidizer for the base case is 69.44 kg/s .

Table 5-1. Properties of Powder River Basin (PRB) coal

Proximate analysis (% wet)				Ultimate analysis (%daf)					HHV (MJ/kg)
Moisture	VM	FC	Ash	C	H	O	N	S	
27.42	31.65	36.43	4.5	73.81	5.01	19.91	0.95	0.32	20.47

Critical design parameters are studied to determine their impacts on wall heat flux. These can broadly be broken down into two categories: 1) the effect of buoyancy-induced internal recirculation, and 2) the effect of fluid dynamic mixing between the fuel and the two oxidizer streams. Finally, the effect of scaling on wall heat flux will be discussed briefly.

5.4 CFD Methods

ANSYS FLUENT version 13.0 was used to simulate different burner designs. The flow field was modeled using the Reynolds-Averaged Navier-Stokes (RANS) equations with the Semi-Implicit Method for Pressure Linked Equations (SIMPLE). Particle trajectories were computed in the Lagrangian frame and were coupled to the gas phase. The sub-models used in this study are presented in Table 5-2, together with the particle and wall properties. Further details on the selection criteria for the sub-models and the sensitivity studies of the particle and wall properties are discussed in Appendix A. Mesh insensitivity studies, including comparison with a 3D mesh consisting of 10 million cells, showed that a 2D axisymmetric mesh with 230,000 cells was sufficient to model the system.

Table 5-2. CFD sub-models and some input parameters

	Sub-models and parameters	Source
Turbulence	shear stress transport k- ω	[127]
Turbulence-chemistry interaction	Finite rate/eddy dissipation model	[128]
Particles turbulent dispersion	Discrete random walk model	[128]
Coal devolatilization	Chemical percolation devolatilization model	[129]
Char oxidation	Kinetics/diffusion-limited model	[128]
Radiation	Discrete ordinates model	[130, 131]
Gas absorption coefficient	Weighted sum of gray gases model	[132]
Coal size distribution	Rosin-rammler distribution, $d_{\text{mean}} = 65 \mu\text{m}$, $d_{\text{min}} = 10 \mu\text{m}$, $d_{\text{max}} = 200 \mu\text{m}$, $s = 3.5$	[98]
Particle emissivity	0.6	[133]
Particle scattering factor	0.6	[134]
Wall emissivity	0.8	[135]
Wall temperature	700 K	[136]

5.5 Results and Discussion

5.5.1 Low-recycle SPOC boiler—base design

The use of two separate oxidizer streams produces a flame structure with two volatile flame fronts, as shown schematically in Figure 5-2. The inner flame front (closer to the axis) results from the reaction between the fuel and pure oxygen (inner oxygen), and the corresponding local flame temperature is very high (~2800 K). The outer flame front results from the reaction between the fuel and the secondary oxidizer (SO), which has a lower oxygen concentration, and thus the corresponding flame temperature is lower.

When over-ventilated (i.e., excess oxygen is delivered for that boiler stage relative to the stoichiometric requirement for complete consumption of the fuel delivered to that stage), three main flame types can result, as shown in Figure 5-4. The type of flame formed would depend on

the amount of oxygen supplied through each oxidizer tube, relative to the stoichiometric amount required by the fuel in the stage. The following discussion on the flame types assumes that the total oxygen supplied is the same (same stoichiometric ratio), though its placement through the inner and surrounding oxidizer tubes could be different. The Type I structure occurs when the oxygen supplied through the SO is much lower than the stoichiometrically required amount, resulting in a short outer flame, while the inner oxygen (IO) flame expands to the wall. This configuration leads to flame impingement, and hence is not an acceptable configuration. The Type II structure occurs when the SO oxygen supply is sufficiently high to prevent flame impingement, but the inner oxygen supply is much lower than the stoichiometric requirement. Due to a small oxygen supply from the central tube, the inner flame is small. This configuration is acceptable from a flame impingement perspective. But, for a given stoichiometric ratio in the stage, this structure would result in a relatively high flue gas recycle requirement since much of the required oxygen is supplied from the SO ($[O_2] = 35\%$, $[\text{recycled flue gas}] = 65\%$). The Type III structure occurs when the SO flow is just sufficient to prevent flame impingement, while most of the oxygen is supplied as inner oxygen. Since most of the oxygen required for the combustion of the fuel in the stage is supplied through the inner tube, this configuration utilizes the full advantage of pure oxygen, and allows the requirements for flue-gas recycle to be minimized. This is, thus, the preferred configuration.

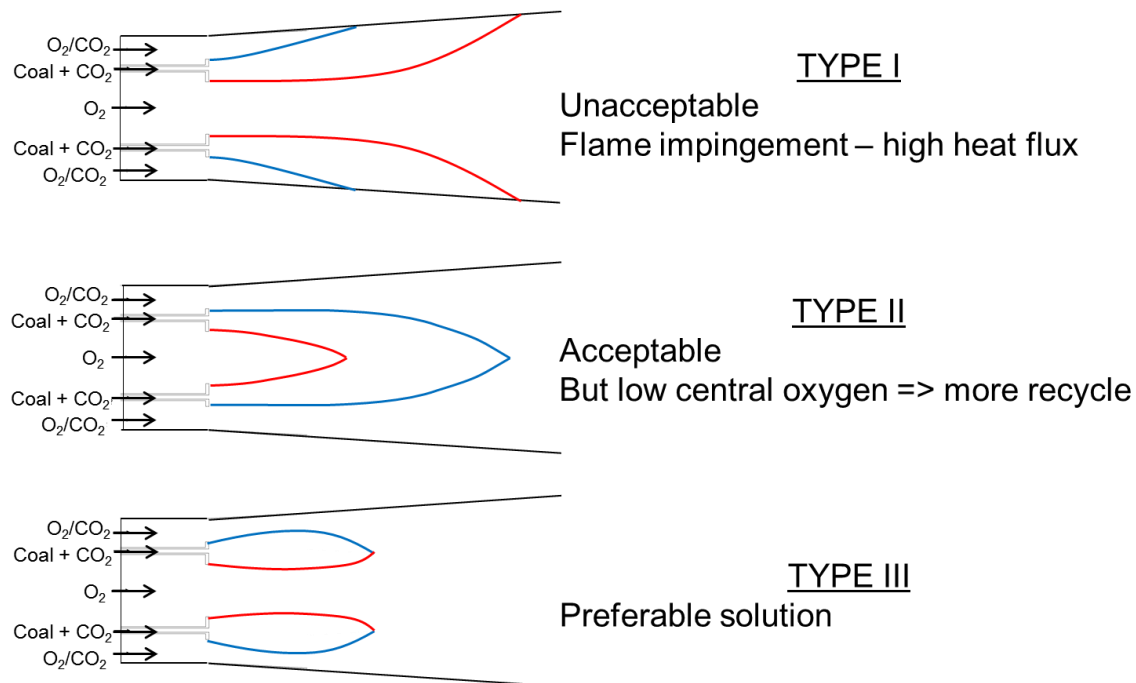


Figure 5-4. Possible flame shapes for a triaxial system with fuel in the annulus, and two oxidizer streams. Dark blue represents the flame resulting from the SO and red represents the flame resulting from the IO.

Under the conditions discussed for the base case in Section 5.3, a Type III flame structure is formed, as can be observed from the volatile reaction rate contours shown in Figure 5-5. The temperature contour, and the location where the radial optical thickness from the wall (τ_w) is 2.3 (i.e., transmissivity is 10%) is also presented in Figure 5-3. The region between the wall and this curve is the radiation penetration layer. Due to the high particle number density caused by the elevated pressure and low flue gas recycle, the radiation penetration layer is very close to the wall for most of the boiler. Furthermore, the temperature inside this layer is much lower than in the core of the boiler, especially in the flame region. This is caused by the “cold buffer layer” created by the secondary oxidizer stream, and the cooling effect of the water tubes. As an example, the near-

wall temperature distribution, including within the radiation penetration layer, is shown in more detail in the inset of Figure 5-5 for the region between 8 m and 10 m from the burner.

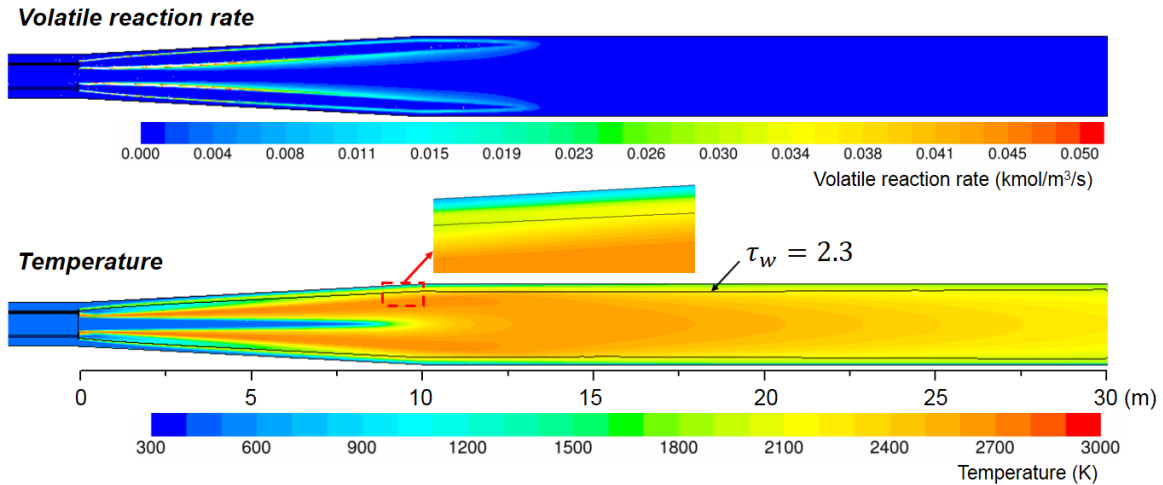


Figure 5-5. Volatile reaction rate and temperature contours for the base case. Note: Only the first 30 m of the boiler shown.

The radiative and total (radiative plus convective) heat flux profiles are shown in Figure 5-6. It is clear, that in the initial region, the radiative heat flux is much lower than what might be expected from such a high flame temperature (up to 2800 K) if radiative trapping had not been effectively implemented. Further downstream, as the buffer layer gradually dissipates due to mixing, the average temperature in the radiation penetration layer increases, as does the heat flux. Nonetheless, the boiler design ensures that the radiative heat flux is not excessive even further downstream, due to the relatively lower temperature maintained in the radiation penetration layer throughout the boiler. The peak radiative heat flux is comparable to that observed in air-fired boilers, even though the temperature in the core of the boiler is much higher.

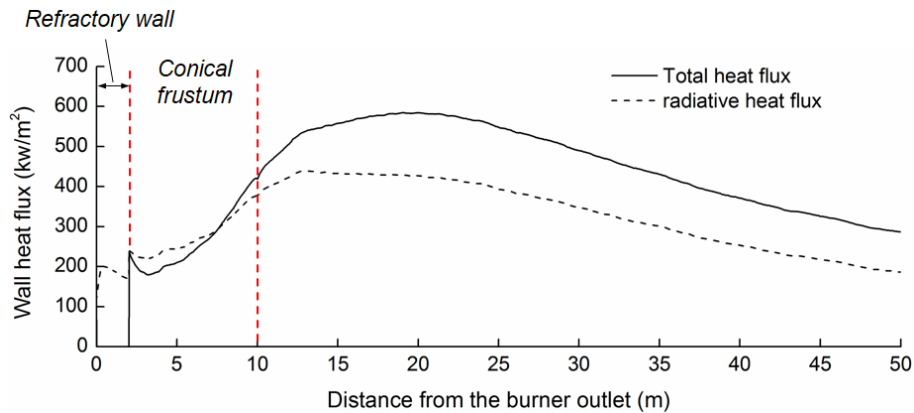


Figure 5-6. Radiative and total heat flux profile for the base case.

In this axial flow boiler, the axial gradients are much smaller than the radial gradients, especially in the radiation penetration layer. This layer effectively acts as a boundary layer for radiation and, similar to other boundary layers, it can be analyzed as a one-dimensional problem. Thus, in the following sections, the radial temperature profiles in this region will suffice for a qualitative discussion of the impact of various design parameters on wall heat flux.

5.5.2 Parametric study of important design parameters

Effect of buoyancy-induced internal recirculation

As described in Section 5.3 the cone angle is designed to result in a uniform axial velocity profile (Figure 5-3) to minimize the impact of buoyancy. The impact of buoyancy-induced internal recirculation on the wall heat flux of such an optically dense boiler is studied here by changing the conical frustum length to induce recirculation. For a given cone angle, a longer frustum length leads to a larger boiler diameter and lower velocity, which could lead to buoyancy-induced internal recirculation.

Figure 5-7 shows the axial velocity and temperature contours for two cases, the base design with no recirculation (10 m cone length), and another design with internal recirculation (20 m cone length and same cone angle). In the latter case, the internal recirculation zone is formed at around 18 m. While this is downstream of the peak temperature region, the recirculation slows the fluid flow upstream, causing the peak temperature region to broaden. This pushes the high temperature gases closer to the wall and results in a higher temperature in the radiation penetration layer.

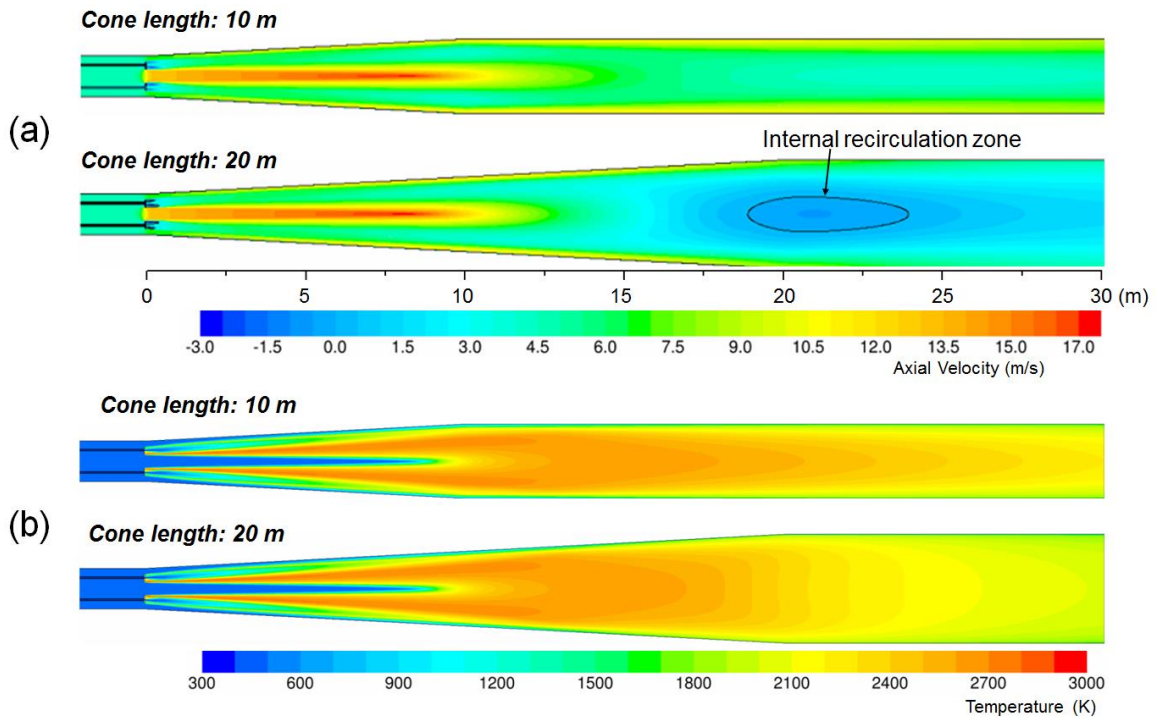


Figure 5-7. First 30 m of (a) axial velocity and (b) temperature contours for two lengths of the conical frustum (10m and 20m).

Due to the small internal recirculation created by buoyancy near the end of the volatile flame, a small difference in the temperature distribution in the radiation penetration layer exists between the two cases. Since the effectiveness of radiative trapping in controlling wall heat flux is

dependent on ensuring a low temperature near the wall, the increased temperature in the radiation penetration layer, which is caused by internal recirculation for the 20 m conical frustum, leads to slightly higher peak heat flux, as shown in Figure 5-8. It is important to recognize that the difference in heat flux is a function of the size of the internal recirculation and its location—for example, a large recirculation in the high-temperature volatile flame region could lead to a much higher temperature in the radiation penetration layer, and thereby wall heat flux. Note, we need only concern ourselves with the near-wall region, since the system is optically dense.

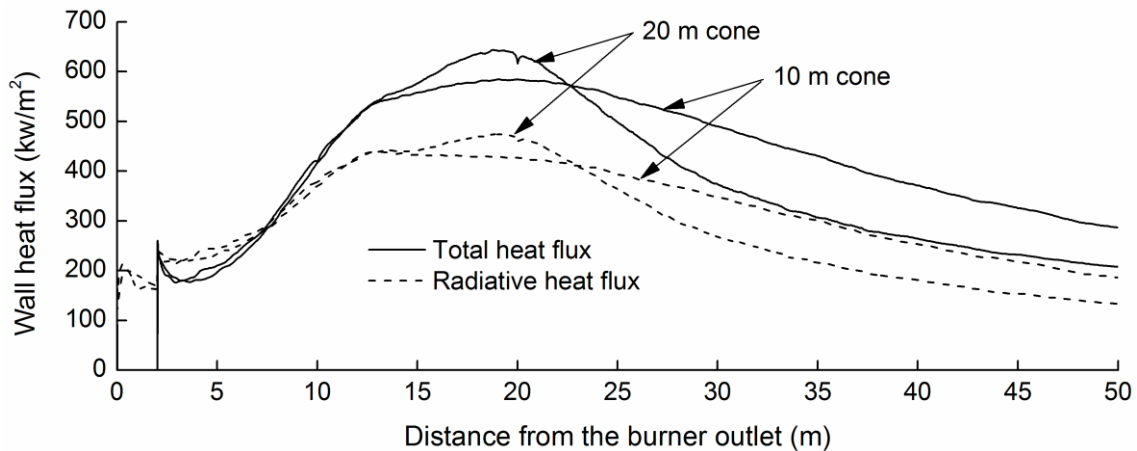


Figure 5-8. Wall heat flux profiles for the two conical frustum lengths shown in Fig. 5-7.

Effect of fuel-oxidizer mixing

The rate of mixing of the fuel stream with the oxidizers can affect the temperature distribution in the boiler, including the radiation penetration layer, and thereby the heat flux. Mixing can be affected by changing the relative velocities between the streams either by changing the physical size of the various tubes in the burner for given flow rates, or by changing flow rates for a given burner geometry.

Effect of burner tube size:

Three different cases, summarized in Table 5-3, were simulated to understand the impact of the relative velocity between the streams on wall heat flux. The size of the IO tube was varied while keeping the overall size of the burner and the hydraulic diameter of the fuel tube fixed. The hydraulic diameter of the SO tube was thus changed. The sizes chosen were such that in one case the inlet velocity of the IO was higher than that of the SO (Case G1), in the second case they were nearly equal (Case G2), and in the third case the inlet velocity of the SO was higher than that of the IO (Case G3). The momentum ratios and velocities for all cases were chosen such that there is no recirculation (internal or external) [109]. Note, Case G2 is the base case, as discussed in the previous section.

Table 5-3. Velocities and geometries of the burner

	Hydraulic diameter (m)		Mean Outlet Velocity (m/s)	
	Inner oxidizer (IO)	Surrounding oxidizer (SO)	Inner oxidizer (IO)	Surrounding oxidizer (SO)
G1	0.508	0.625	7.40	4.10
G2	0.635	0.513	4.74	4.72
G3	0.889	0.292	2.42	7.48

Figure 5-9 shows the temperature contours and radiation penetration layers for the three cases. The volatile flame lengths, as determined by the completion of volatile reactions, are shown with red arrows. As expected, the volatile flame lengths are shorter for cases G1 and G3, where the streams have different velocities, as compared to case G2, where all streams have similar velocities. The faster mixing caused by the higher relative velocities between the streams not only reduces the volatile flame length, but also increases the radial mixing in the near-burner region. The increased

radial mixing results in an increase in temperature in the radiation penetration layer, as shown in the inset of Figure 5-9. The differences in the temperature profiles in the radiative penetration layers are reflected in the near-burner variations in the radiative heat flux profiles, as shown in Figure 5-10.

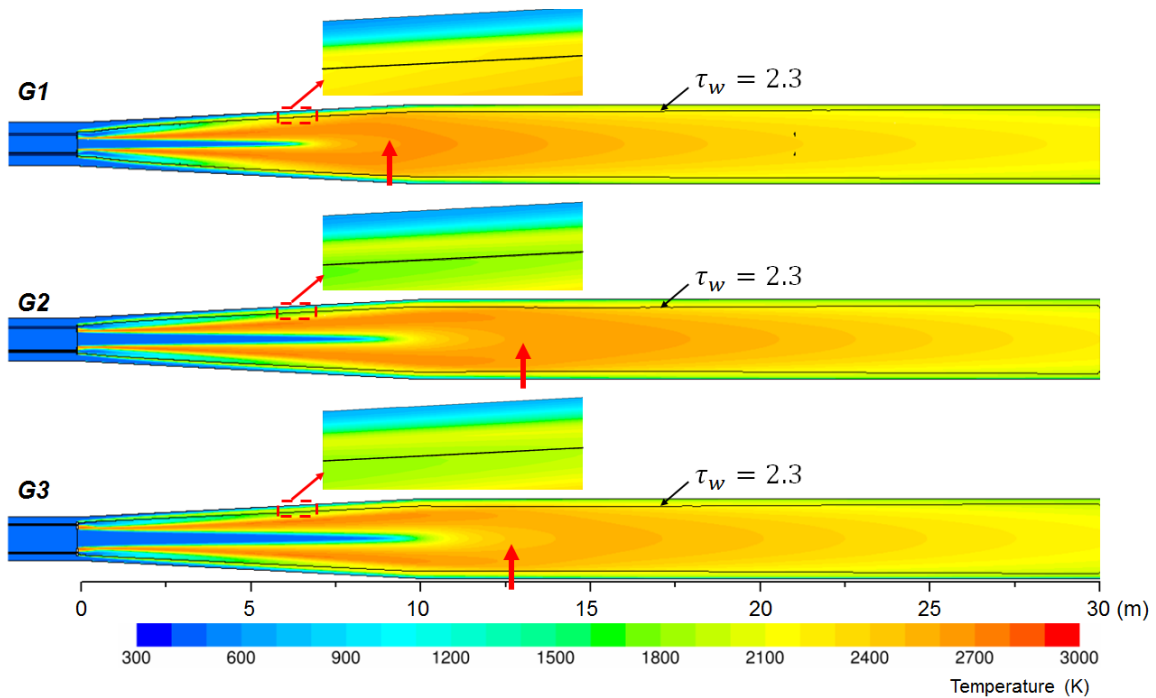


Figure 5-9. Temperature contours with optical thickness of 2.3 from the wall overlaid for different burner configurations. The red arrows indicate the flame lengths measured by volatile reaction rates.

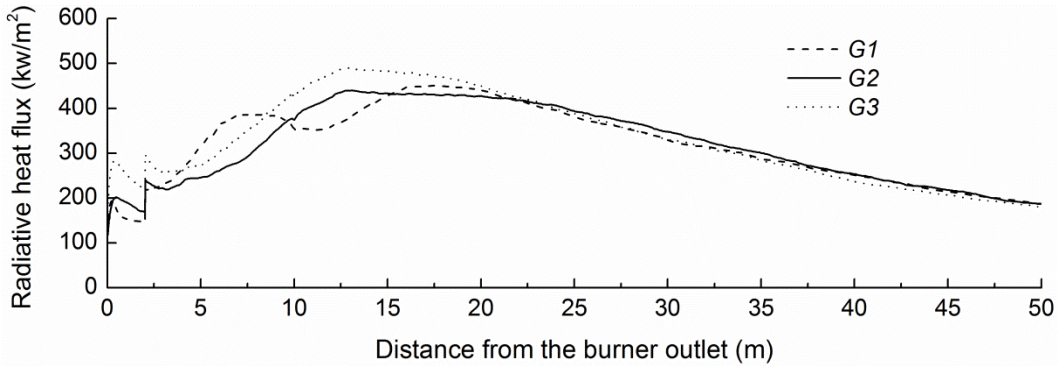


Figure 5-10. Radiative heat flux profiles for different burner configurations.

However, the peak heat fluxes for the three designs are quite similar. The peak heat flux location is where the “cold buffer gas” flow near the wall has mixed with the hot combustion gases enough to reach a maximum average temperature in the radiation penetration layer. Due to the relatively low wall heat flux and the small wall surface area in the near burner region, the near-burner variations in the radiative heat flux profiles mentioned above have little impact on the post-flame flue gas temperature, and thus on the downstream temperature in the radiation penetration layer.

Effect of inner oxygen flow rate:

As explained in the introduction of Section 5.5.2, changing the IO flow rate will affect mixing. Varying the IO flow rate also changes the overall stoichiometric ratio in the particular stage. Note that this does not affect the total oxygen consumption for the entire plant. This is because with the staging implemented in the SPOC process, the distribution of oxidizer to each stage can be varied without varying the total oxygen supplied. In this section the IO flow rate will be characterized by the inner oxygen stoichiometric ratio (SR_{IO}), which is defined as

$$SR_{IO} = \frac{Y_{O_2}^{IO} m_{IO}}{m_{O_2st}}$$

where, $Y_{O_2}^{IO}$ is the mass fraction of oxygen in the inner oxidizer (= 1 for this work), m_{IO} is the mass flow rate of the inner oxidizer, and m_{O_2st} is the mass flow rate of oxygen required stoichiometrically for the complete combustion of the fuel supplied to the stage. Four different inner oxygen flow rates are considered, corresponding to SR_{IO} of 0.35, 0.78 (base case), 1.28 and 1.78. In all cases, the SO flow rate is the same and the total oxygen supplied is more than required by the fuel in that stage.

The temperature contours for the different cases are shown in Figure 5-11. Similar to Figure 5-9, the red arrows mark the volatile flame lengths for the various cases. With increasing inner oxygen flow, the flame length is shorter, and there are two reasons for this. First, with increasing inner oxygen flow, the mixing between fuel and pure oxygen increases due to the increased relative velocity, leading to a higher combustion rate. Second, the downstream oxygen concentration is higher with higher SR_{IO} .

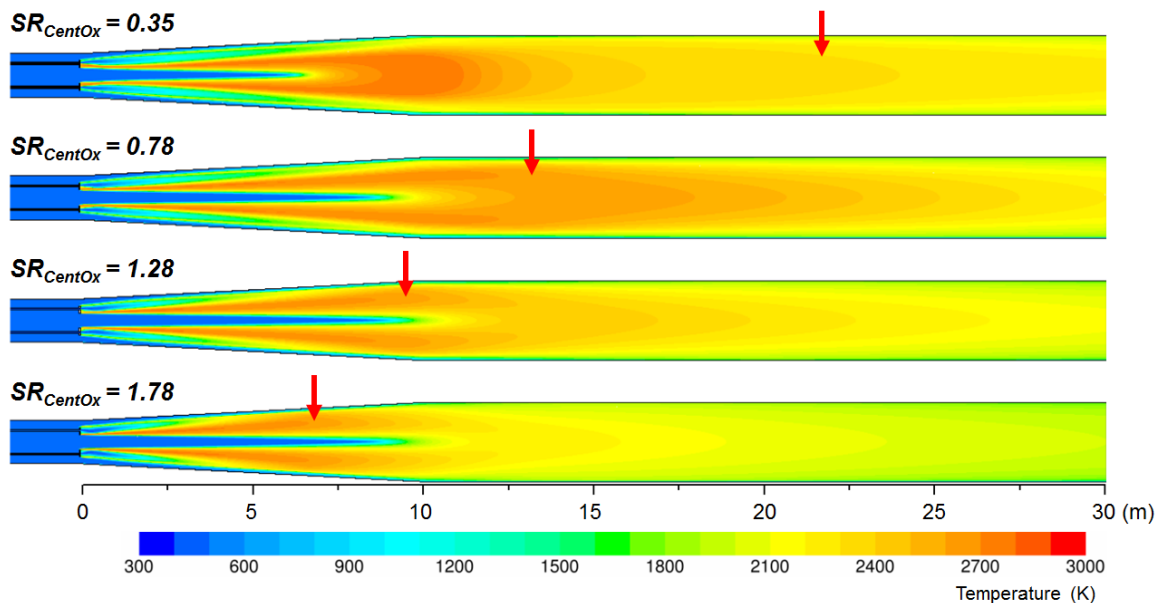


Figure 5-11. Temperature contours for different SR_{IO} . The red arrows indicate the volatile flame lengths as determined by completion of volatile reactions.

Figure 5-12 shows the radiative heat flux profiles for the four cases. The peak radiative heat flux is similar for all cases, as it was in the previous sub-section where burner geometry was varied. However, in the near-burner region, due to differences in local mixing, the location of the peak heat flux is different. Far downstream, the well-mixed temperatures are different, due to differences in the total gas supplied to the stage, resulting in different wall-heat fluxes.

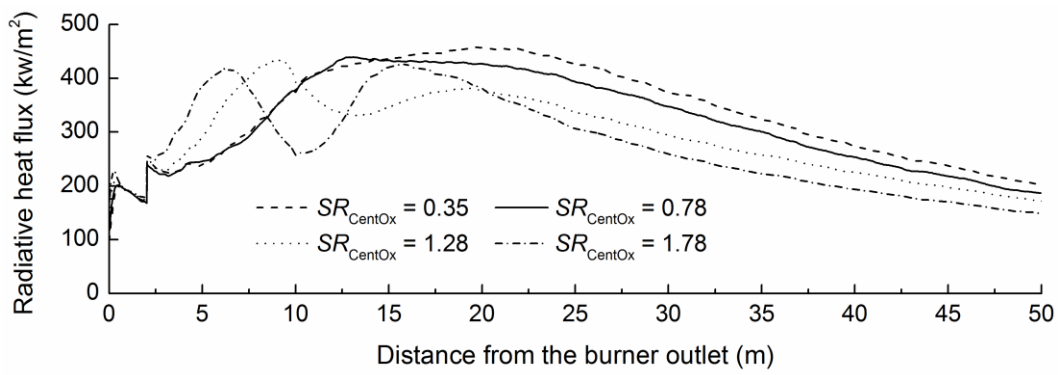


Figure 5-12. Radiative heat flux profiles for different SR_{IO} .

Increasing the inner oxygen flow rate between that of $SR_{IO} = 0.35$ and 0.78 does not affect the wall heat flux significantly in the near-burner region. This is because, with a low IO flow rate, the velocity of the SO is higher and it dominates the temperature in the near-wall region (radiation penetration layer). Thus, there is a broad range of operating conditions under which the radiative heat flux profiles are similar, and a broader range, where the peak radiative heat fluxes are similar. This implies that the basic burner design is robust and not prone to strong swings in wall heat flux under varying operating conditions.

5.6 Conclusions

In this chapter, a new and flexible, staged, pressurized oxy-combustion (SPOC) boiler design is presented for carbon capture with low flue-gas recycle. The burner and boiler design is based on the goal of ensuring a relatively smooth and high wall heat flux profile over the length of the boiler, with a manageable level of peak heat flux. Inner oxygen injection is utilized to supply most of the required oxygen, thus minimizing flue gas recycle, while still maintaining a low oxygen concentration next to the boiler tubes, with the use of a surrounding oxidizer outside of the fuel annulus. With the fuel being supplied in the annulus, a significant portion of the radiation from the inner-oxygen flame is trapped, thus effectively limiting wall radiation even though the inner-oxygen flame is at a very high temperature. The surrounding oxidizer serves to keep the flame away from the wall. It also serves an additional purpose of providing a cold buffer gas layer next to the wall to keep the temperature in the radiation penetration layer low, enabling radiative trapping as a means to control wall heat flux. This design allows the number of stages to be minimized and three stages is found to be optimum. Furthermore, flexible operation is possible by the ability to control the amount and concentration of oxygen supplied to each stage in this multi-stage process.

Through a systematic study of several burner and boiler parameters, the critical factors affecting wall heat flux profiles were evaluated. The boiler design has been shown to be quite robust, with the peak wall heat flux of the SPOC boiler being resilient to firing conditions. The most ideal conditions to ensure a high and relatively flat wall heat flux profiles is presented. Finally, though not discussed in detail in this paper, the total heat flux closely follows the radiative heat flux because the convective heat transfer coefficient is not very high for parallel flow systems, and the temperature in the near-wall region is controlled to be low.

Chapter 6

Operational Flexibility of SPOC Boilers

6.1 Introduction

An important consideration for all new thermal electric power plants is the variable thermal loading during the operating lifetime of the plant. The growing share of renewable energy sources producing clean, yet unreliable and intermittent, electricity is forcing natural gas combined cycle and coal-based power plants to operate with daily load variations [119]. As an example, a joint study by Siemens and VDE recently concluded that depending on the wind conditions in Germany, there could be 100% daily start-stop for baseload generators [137]. Similar problems are being faced by electric grid operators in most of Europe and US. A simple schematic showcasing the problem is presented in Figure 6-1 [138].

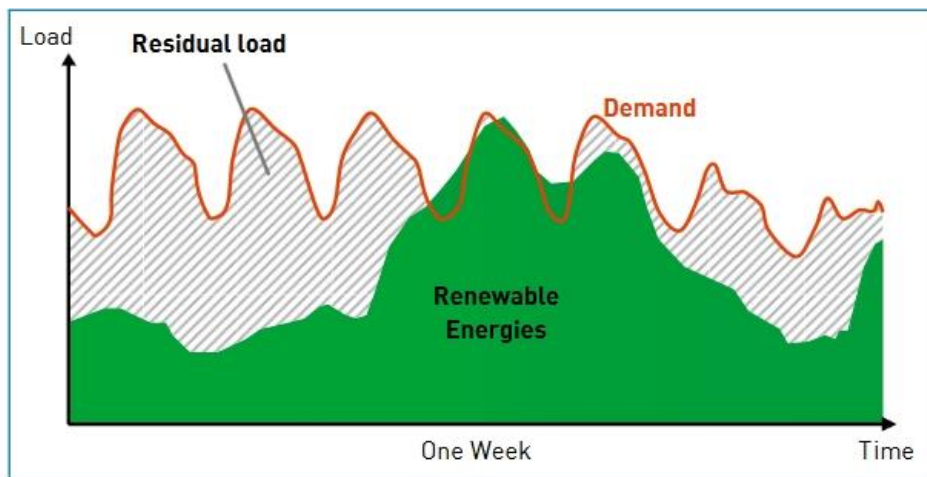


Figure 6-1. Schematic showing the comparison of electricity produced by renewable sources and the electricity demand. The difference—residual power—has to be generated by non-renewable source. Reproduced from [111]

In terms of plant flexibility, a number of areas need to be addressed, such as equipment—especially the turbomachinery—performance at varying turndown ratios, the operation of the boilers, the maximum ramp rates possible, and heat integration. The plant performance for various carbon capture processes has been studied [119-124]. The performance of pressurized oxy-combustion under varying loads has also been evaluated [139]. The role of the flue gas moisture latent heat recovery section, and its integration into the Rankine cycle for low-pressure regeneration, was found to be invaluable in enhancing the cycle flexibility for the pressurized oxy-combustion systems [139]. There are other aspects of the SPOC process, such as the multi-stage design, and the low temperature NO_x removal (instead of a high temperature SCR / SNCR based process), that are also advantageous for flexible operation [46, 124], but these are not the focus of this chapter. Stanger et al. [39] discussed the preferred characteristics of new power plant designs, and indicated that a stable turndown to 40% thermal load is desirable for the burner and boiler. In Chapter 5 a new burner and boiler design was introduced for the low-recycle pressurized oxy-combustion process. In this chapter, we focus on the turndown capability of the boiler of the three-stage SPOC process. Following Stanger et al. [39], and in keeping with the theme of Chapter 5, we will focus on the wall heat flux for operation at 40% of design load. Modifications to the design of the boiler presented in Chapter 5 will be introduced to better control heat flux under varying thermal loads.

6.2 CFD Methods and Simulation Conditions

The boiler and burner design from Chapter 5 are shown in Figure 6-2. The coal properties and the baseload operating conditions are presented in Table 6-1. ANSYS FLUENT version 13.0 was used to simulate the boiler. The modeling methods, the sub-models, and the boundary conditions are the same as in Chapter 5. The number of cells in the 2D axisymmetric simulation space was increased from 230,000 to 343,000 to accommodate for some of the new boiler modifications to be presented in this chapter. Mesh sensitivity studies were conducted and this number was deemed sufficient to model the features of interest for this study.

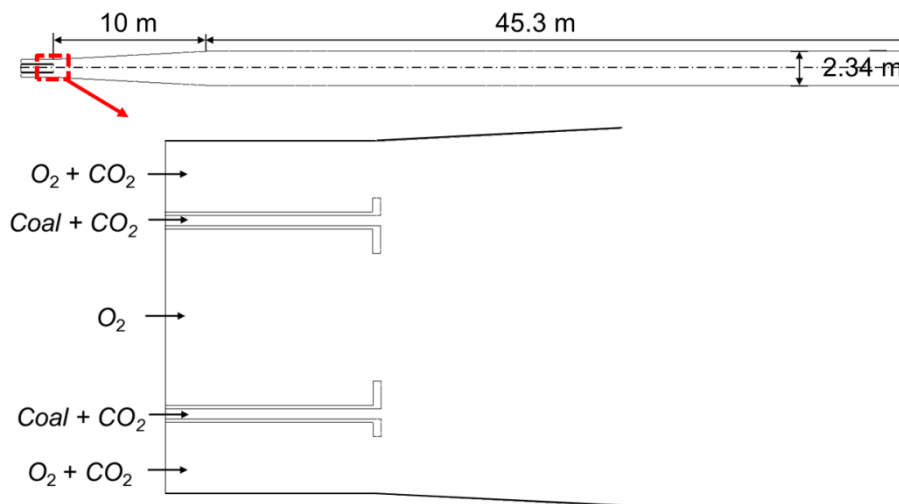


Figure 6-2. Geometry of the boiler and burner. Reproduced from Chapter 5.

Table 6-1. Coal properties and operating conditions.

Coal properties (Powder River Basin)									
Proximate analysis (% wet)				Ultimate analysis (%daf)					HHV
Moisture	VM	FC	Ash	C	H	O	N	S	(MJ/kg)
27.42	31.65	36.43	4.5	73.81	5.01	19.91	0.95	0.32	20.47
Operating conditions									
		Mass flow rate (kg/s)	O ₂ (vol. %)	CO ₂ (vol. %)	Temp. (K)				
Coal		18.8							
Coal carrier gas		1.2	0	100	458				
Central oxygen		21.7	100	0	458				
Secondary oxidizer		69.4	35	65	458				

6.3 Effect of Turndown

The radiation and total wall heat flux for the base case, T100 (100% thermal input), and the turndown case, T40 (40% thermal input), are shown in Figure 6-3. As the thermal input is reduced, the location of the peak heat flux shifts closer to the burner, and the peak value is higher than at full-load. Since the total heat flux is dominated by the radiative heat flux, both follow the same trend.

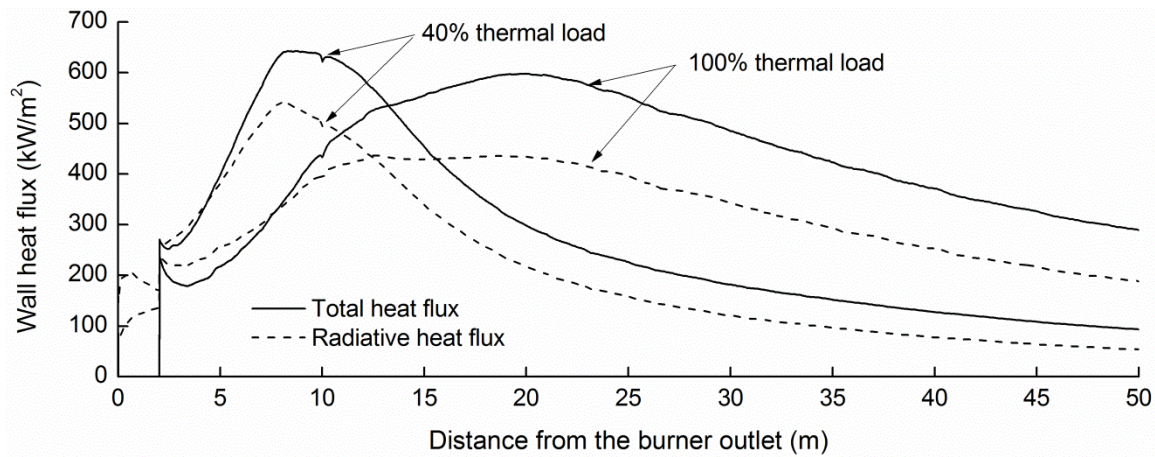


Figure 6-3. Radiative and total heat flux for the base (100% thermal input) case and the turndown case (40% thermal input).

The first 30 m of the temperature contours for the two cases are shown in Figure 6-4. The flame is attached for both cases, but with turndown it is shorter since less fuel is supplied and thus the fuel is consumed earlier. In addition, the flame is closer to the wall on turndown, as shown in the figure inset of the magnified region between 8 and 10 m. The proximity of the flame to the wall causes the average temperature in the radiation penetration layer (i.e., the region between the wall and the $\tau_w = 2.3$ contour) to increase.

The reason that the flame resides closer to the wall with turndown can be understood from the axial velocity contours shown in Figure 6-5. During turndown, the fuel and oxidizer inputs to the boiler are reduced, leading to lower velocities in the boiler. This reduced velocity leads to a higher Richardson number and buoyancy induced recirculation (Figure 6-5), further shortening the flame and pushing it closer to the wall.

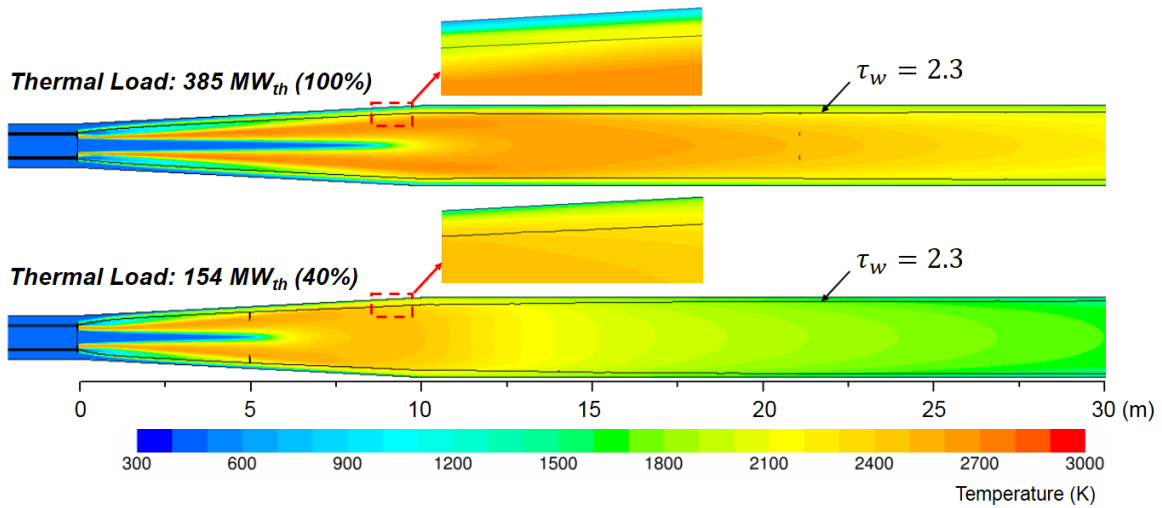


Figure 6-4. The first 30 m of the temperature contours for the base case (100% thermal input) and the turndown case (40% thermal input) with $\tau_w = 2.3$ contour overlaid.

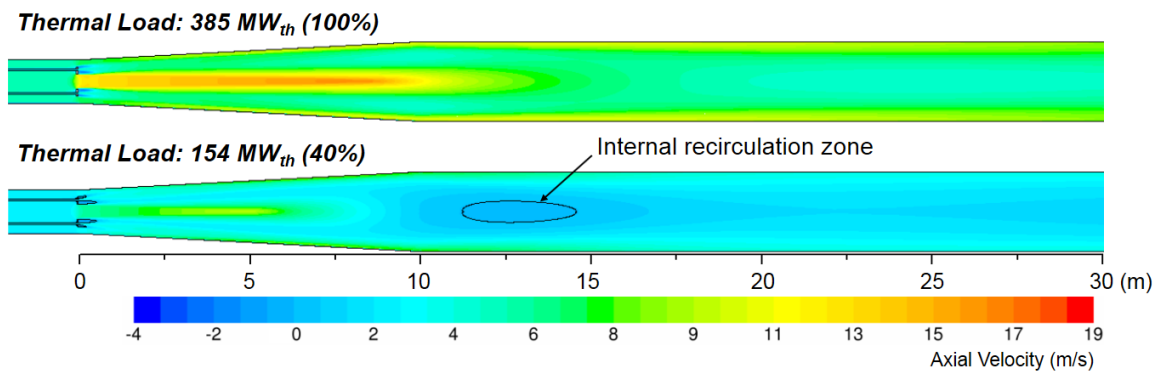


Figure 6-5. The first 30 m of the axial velocity contours for the base (100% thermal input) case and the turndown case (40% thermal input). Buoyancy induced internal recirculation shown using iso-contour for zero axial velocity.

Although the boiler system is well-designed for 100% thermal input, the design needs to address the high peak heat flux at turndown, and avoid buoyancy-induced adverse pressure gradients that lead to a flame close to the wall. A method to address this shortcoming with a modification to the design is discussed in the next section.

6.4 Modified Boiler Design

To enhance the effect of radiative trapping when operating the system under reduced thermal input, the high temperature gases should be “focused” to the center (axis) of the reactor, and not allowed to spread quickly to the walls. Also, the velocities must be kept high, even at the reduced flow rates associated with turndown. To achieve this, small obstructions, such as rings, can be added to the wall so that small, localized recirculation zones are formed in their wake. As will be shown below, this effectively pushes the remaining flow away from the wall, keeping the near-wall region relatively cold for a longer distance. The displaced flow increases the velocity in the core of the boiler, which reduces the effect of buoyancy, and consequently the bulging of the flame towards the wall. An added advantage of such a modification is that the maximum diameter of the boiler can be increased. This is because buoyancy-induced internal recirculation in the flame region, which was found in Chapter 5 to limit the maximum diameter of the boiler, does not occur until much larger diameter. The increased boiler diameter can help further reduce the heat flux, while also increasing the surface area per unit axial length. The increased surface area would lead to a shorter boiler.

6.4.1 Wall rings

The boiler design was modified by adding rings—with a rectangular cross-section—to the walls of the boiler, starting at 2 m downstream of the burner and repeating every 1 m up to 31 m from the burner. The rings project radially out 0.1 m from the wall and have a thickness of 2.54 cm. These rings could be constructed from refractory material or water-cooled tubes. Since the surface area of the rings is negligible compared with the total surface area of the wall, the boundary condition assumed for the rings will have little impact on the overall heat flux profile, and in this work, the rings are modeled as adiabatic walls. A schematic of a boiler with these wall-rings is shown in Figure 6-6. The axial velocity and temperature contours for the 100% and 40% thermal input cases (T100 and T40, respectively) are shown in Figure 6-7 where wall rings have been added. As desired, the use of these wall rings increases advection and eliminates the buoyancy induced internal recirculation in the T40 case. The temperature profile also shows a longer and thinner high temperature zone, rather than the short and bushy high temperature zone observed for the turndown case without rings (Figure 6-4).

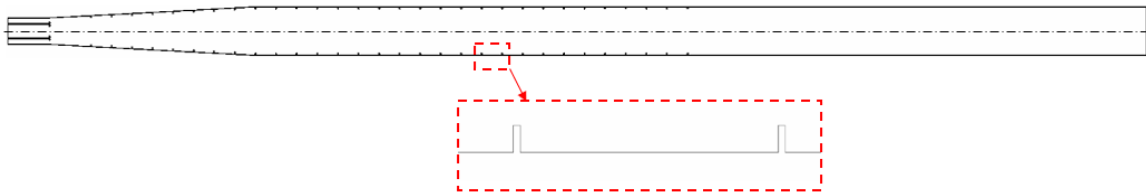


Figure 6-6. Schematic of the modified boiler design with wall-rings added to increase effectiveness of advection.

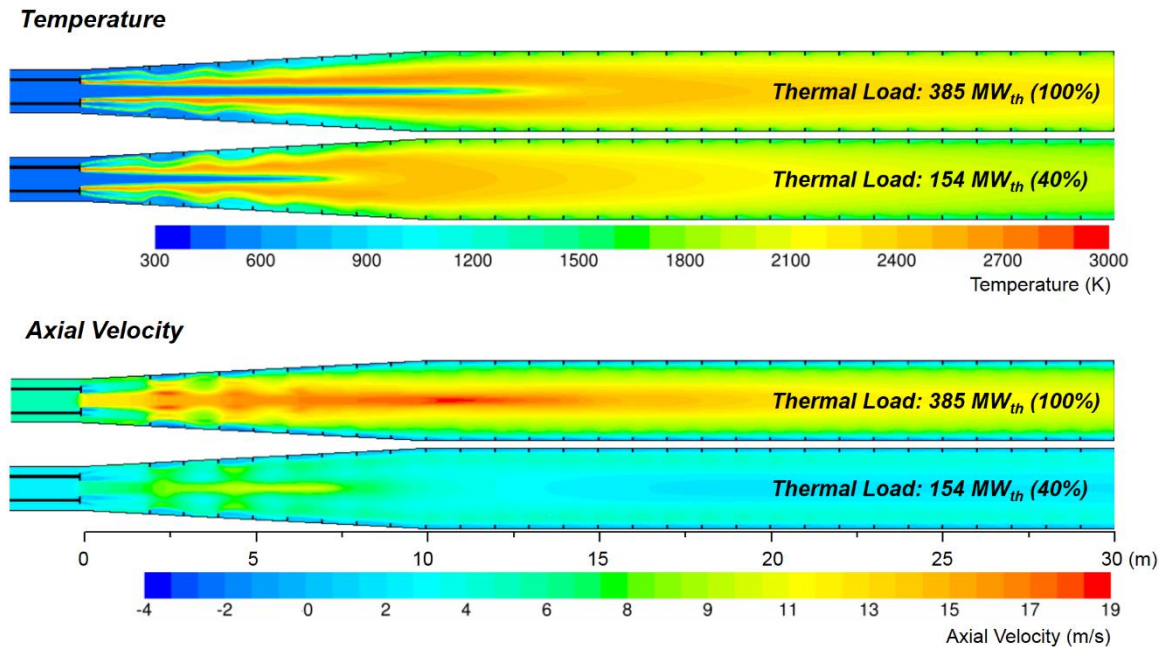


Figure 6-7. The first 30 m of temperature and axial velocity contours for base case and the turndown case with rings.

The radiative and total heat flux profiles for the 100% and 40% thermal input cases with and without the wall-rings are shown in Figure 6-8. Since the rings are modeled as adiabatic surfaces, the total heat fluxes on these rings are zero. Thus, the heat flux profile with rings has periodic dips for both radiative and total heat flux, at the location of the rings. With turndown (T40), the total heat flux peak is reduced by more than 100 kW/m^2 compared to without rings. The location of the peak heat flux shifts downstream as well, due to the reduced impact of buoyancy. Similarly, the use of rings reduces the radiative heat flux for the T100 case in the flame region. However, due to increased convection, the maximum total heat flux for the T100 case is similar with and without rings. For the T40 case, since the peak heat flux was caused primarily by high temperatures in the radiation penetration layer, the significant reduction in radiative heat flux overwhelms the modest increase in convective heat flux, and the total heat flux is lower with rings than without. In the

post-flame region, the heat flux is slightly higher, especially for the T40 case, because flue gas temperatures are higher due to the lower wall-heat-transfer rates upstream.

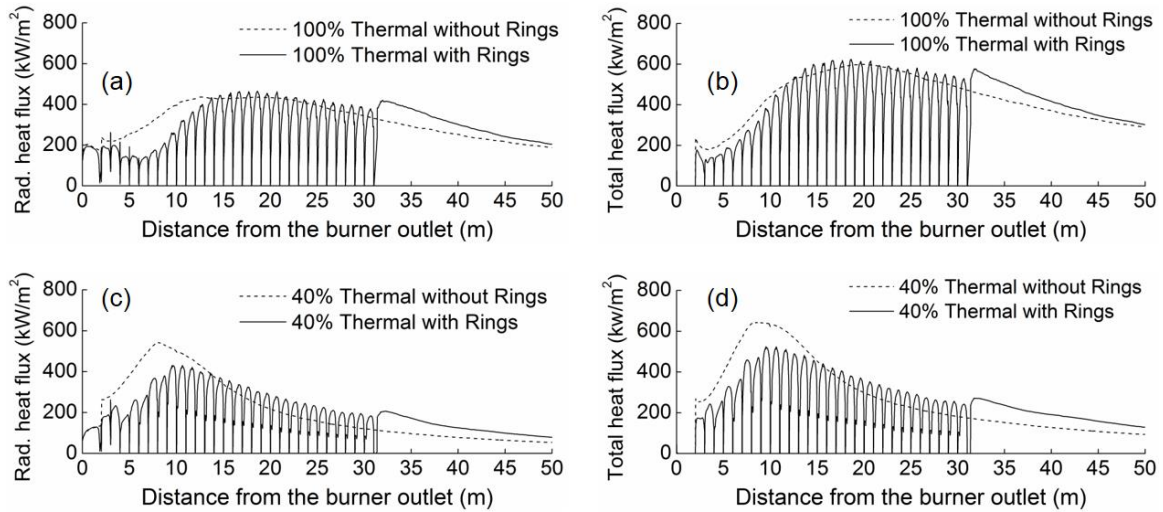


Figure 6-8. Comparison of wall heat flux for different thermal loads: (a) radiative and (b) total heat flux for the 100% thermal input case, and (c) radiative and (d) total heat flux for the 40% thermal input case.

The effect of the rings on the heat flux profile can be understood by analyzing the way rings affect the local and global fluid dynamics. Locally, the rings create small recirculation zones, which enhance local mixing. Globally, these small recirculation zones push the main flow towards the core (axis) of the boiler. Since the near-wall gases start at a lower temperature and there is limited spread of energy from the core of the boiler to these near-wall gases, the enhanced mixing creates a thicker buffer layer of “cold” gases compared with the case without rings, leading to a lower radiative wall heat flux, by reducing the average temperature in the radiative penetration layer. Radial temperature and optical thickness profiles provide a more quantitative picture of the effect of wall-rings on heat flux. As an example, Figure 6-9 shows these, with and without rings, for 100% thermal input at an axial distance of 7.5 m. The figure only shows the near-wall region due

to its importance in determining wall heat flux. Figure 6-9a shows the temperature and optical thickness profile as a function of radial distance from the wall, while Figure 6-9b shows the temperature as a function of optical thickness from the wall. Clearly, the use of rings creates a flatter profile near the wall due to enhancement in local mixing. In the radiation penetration layer (i.e., the region where τ_w is less than 2.3), the temperature and optical thickness gradients in the axial direction are negligible compared with those in the radial direction. Thus, this layer can be reasonably considered as a 1-D medium, from which the radiation power can be estimated. Qualitatively, it can be seen that in most of the region, the temperature is higher without rings than with rings. The difference in heat flux can also be estimated quantitatively by the following 1-D equation [110],

$$q_w = 2 \int_0^{\tau_w} \sigma T^4(\tau_w') \int_0^1 e^{-\tau_w'/\mu} d\mu d\tau_w' \quad (6-1)$$

where τ_w' is the optical thickness from the wall to the location of interest inside the medium, τ_w is the optical thickness of the radiation penetration layer, T is the local temperature, and σ is the Stefan–Boltzmann constant. From calculations, the radiative power for the case with rings is more than 200 kW/m² lower than for the case without rings at 7.5 m. A similar analysis for T40 produces similar results, and hence, for concision, they are not shown here.

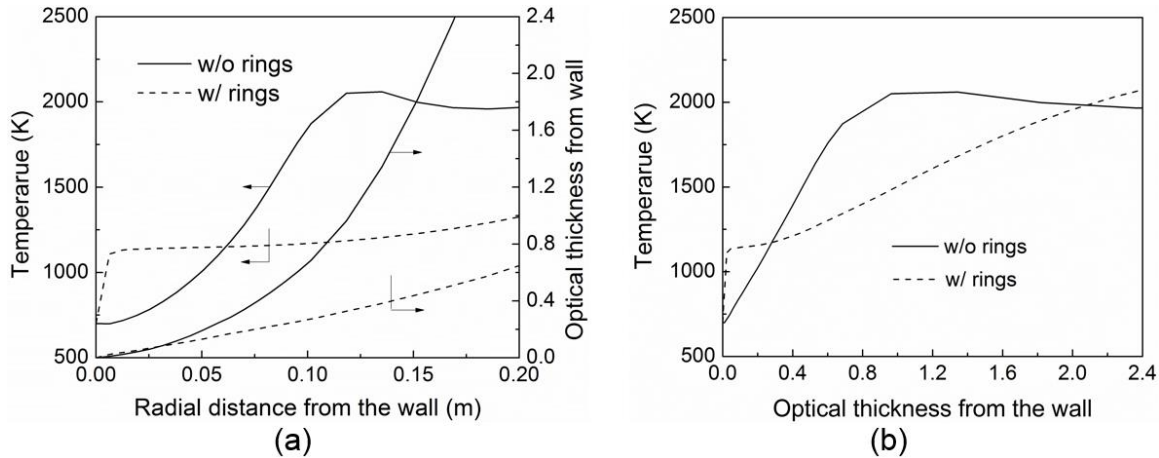


Figure 6-9. (a) Temperature and optical thickness profiles as functions of radial distance from the wall and (b) the temperature profile as a function of optical thickness from the wall at 7.5 downstream from the burner for the 100% thermal input cases with and without rings

6.4.2 Larger boiler diameter with wall-rings

In the previous design (Chapter 5), the cone angle and length were constrained to avoid buoyancy-induced recirculation, resulting in a boiler diameter of 2.83 m. Since the flue gas temperature must be reduced to an acceptable value before boiler tubes can be added in the interior of the boiler for convective heat transfer, the length of the radiant boiler is dependent on the total heat transfer per unit length, and a smaller boiler diameter would result in a longer boiler. With the addition of wall rings, and the associated increase in axial velocity, the length of the cone-shaped section, and hence the maximum boiler diameter can be increased without causing internal recirculation. In this section, the boiler is expanded to 4 m in inner diameter by extending the conical frustum length to 25 m from the burner. This diameter was chosen such that off-site manufacturing and shipping of the boilers on railroads would be possible [98]. The diameter can be changed with evolving capabilities for shipping the boilers.

Figure 6-10 shows, for the case of 100% thermal input, the temperature and axial velocity contours for the first 40 m of the boiler. The increase in velocity, which is caused by the rings, is high enough to avoid recirculation. The resulting heat flux profile is shown in Figure 6-11. As shown, the peak heat flux for the T100 case is reduced to less than 500 kW/m², and hence standard boiler tube materials can be utilized in the boiler [98, 140]. Furthermore, with a larger boiler diameter, more heat transfer surface area is available per unit length of the boiler, and hence a shorter boiler can be designed.

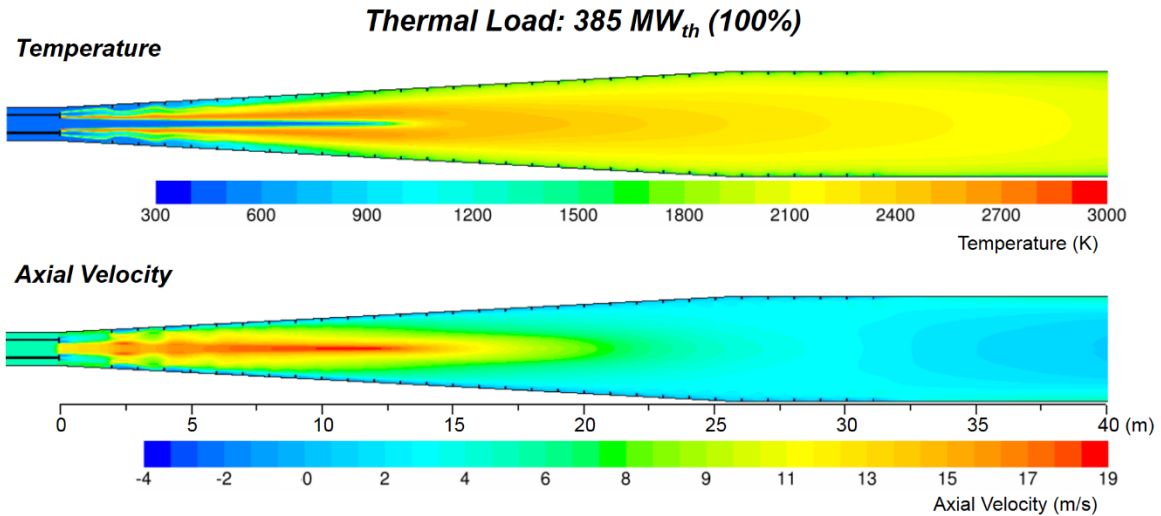


Figure 6-10. The first 40 m of temperature and axial velocity contours for the 100% thermal input case with wall-rings and longer expansion.

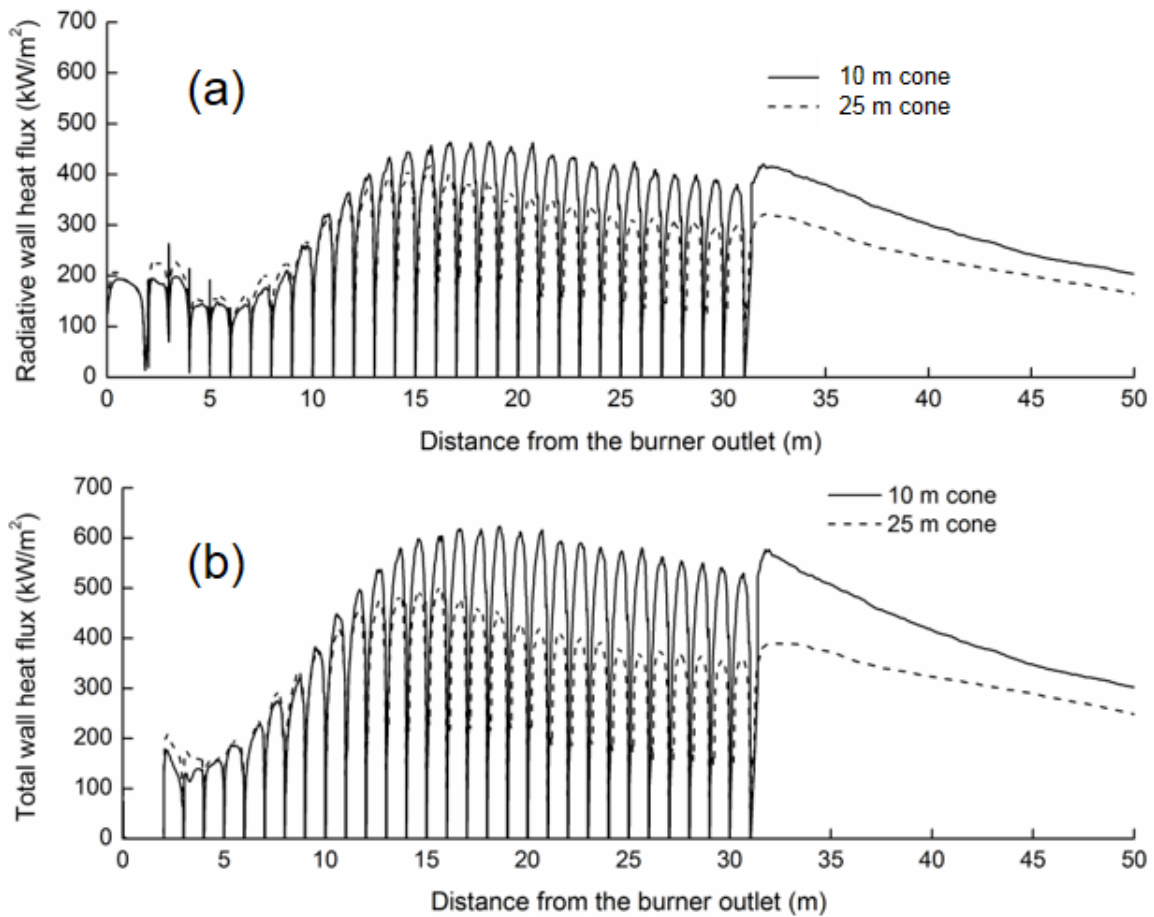


Figure 6-11. The (a) radiative and (b) total heat flux profiles for the 100% thermal input case with wall-rings and a longer conical expansion.

Figure 6-12 shows the temperature and axial velocity contours for the first 40 m of the 40% thermal input case, with the larger boiler diameter. In this case, internal recirculation starts at approximately 15 m. Since the volatile flame length is approximately 8.5 m, the recirculation does not affect the volatile flame. Thus, at 40% of design load, the heat flux profiles for both boiler diameters are similar in the flame region (Figure 6-13). Downstream, the heat flux drops faster for the larger boiler diameter due to the larger heat transfer surface area per unit length of boiler.

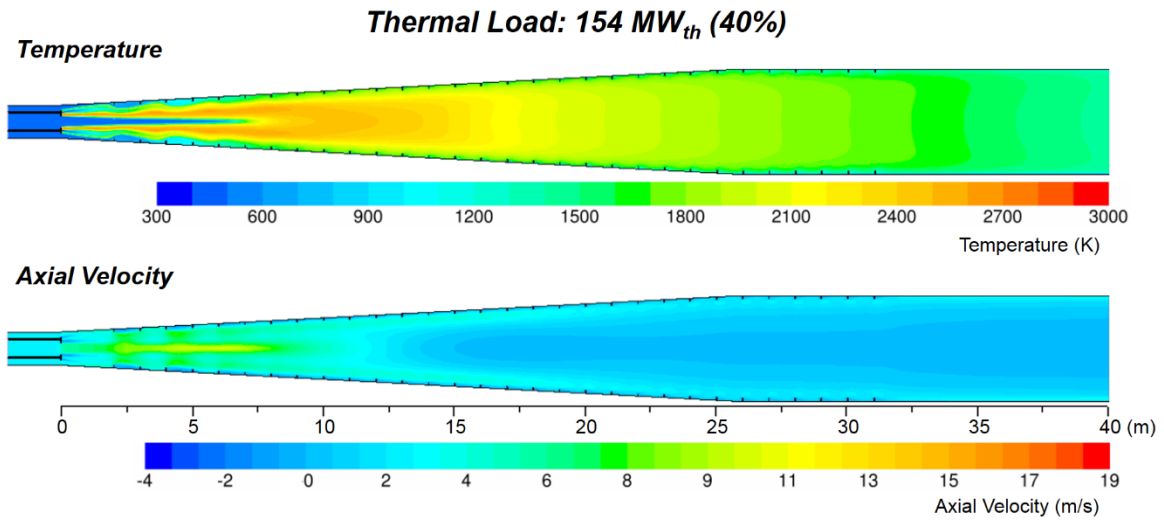


Figure 6-13. The first 40 m of temperature and axial velocity contours for the 40% thermal input case with wall-rings and longer expansion.

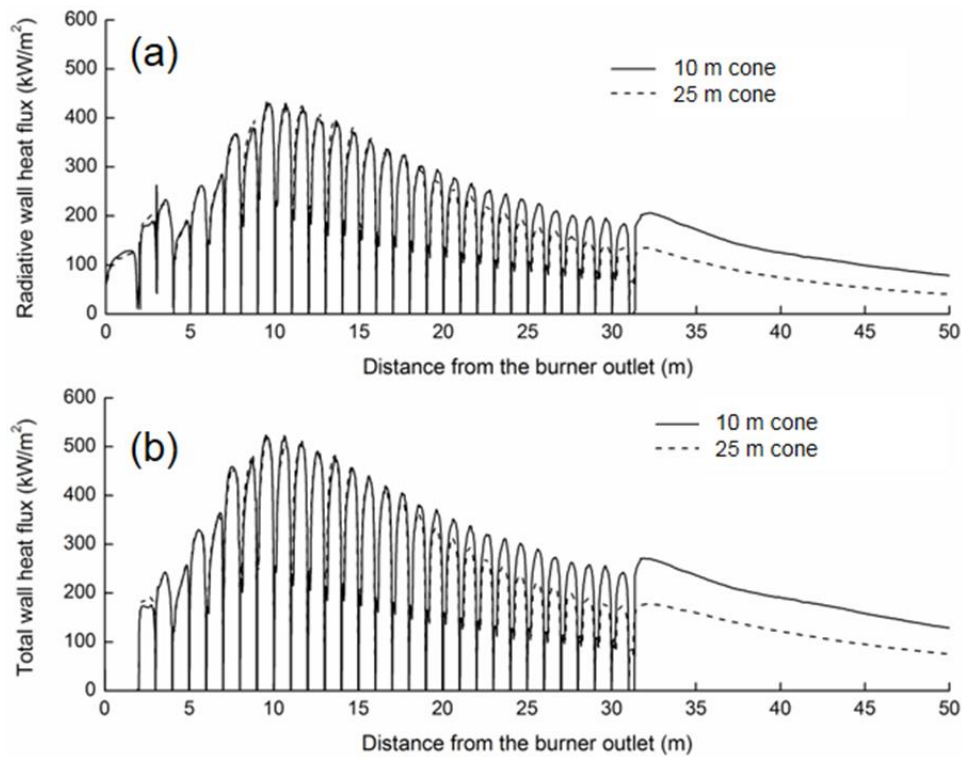


Figure 6-12. The (a) radiative, and (b) total heat flux profiles for the 40% thermal input case with wall-rings and a longer conical expansion.

In the previous design, the increase in boiler diameter to reduce the length could have been achieved by creating a second expansion downstream of the high temperature region, where the gases are sufficiently mixed, but it adds additional complexity. The design with rings enables a continued expansion of the conical frustum up to the final boiler diameter. Hence, a larger diameter boiler can be designed with less loss of surface area and a simpler construction.

Note that the number, size and shape of rings have not been optimized in this study since the primary purpose of this work is to illustrate the effectiveness of this structural change to allow for variable load operation of the SPOC boilers.

6.5 Conclusions

Staged, pressurized oxy-combustion can increase the efficiency of power generation with carbon capture by more than 6 %-pts. The performance of the SPOC boilers with varying thermal load was investigated in this work. The impact of turndown on wall heat flux in was studied for one stage, with the understanding that the results can be extended to the other stages as well.

It was observed that during turndown operations, excessive peak heat flux can occur in the flame region due to buoyancy-induced recirculation. This was overcome by incorporating wall-rings, which minimize the effect of buoyancy, and enhance the effectiveness of radiative trapping to control wall heat flux. The use of wall-rings increases bulk axial velocity without compromising the wall heat exchange area. The increased axial gas velocity caused by wall-rings allows for an increase in the size of the conical frustum section, so that the boiler diameter can be increased, without causing an increase in heat flux due to buoyancy-induced recirculation. Incorporating the

design modifications presented in this work reduces the maximum wall heat flux to less than 500 kW/m², for both full and part-load, thereby enabling the use of standard boiler tube material everywhere in the boilers.

While not considered in this work, the multi-stage-boiler design of SPOC has an additional benefit over a single-boiler design because, with SPOC, it is possible to shut down the last stage boiler during turndown. In this way, the difficulties in steam integration during turndown can be significantly reduced, and much lower turndown ratios are possible.

Chapter 7

Soot in Tri-axial Flames

7.1 Introduction

In the previous two chapters, a new burner and boiler design were presented for an oxy-coal combustion process with low flue gas recycle. The main controlling factors affecting the wall heat flux were parametrically varied to demonstrate the robustness of the design. Furthermore, the flexibility of the system was also discussed in terms of part-load operations. Since the burner was designed with three ports—for the inner oxidizer, fuel, and secondary oxidizer—a very brief introduction to tri-axial flame shapes was also provided in Chapter 5.

In Chapter 4, the last challenge of low-recycle systems mentioned was the control of soot from such systems. The various tri-axial flame shapes could produce different levels of soot, which could in turn be quite different from the levels produced by normal flames. In Appendix B, a method of controlling soot—and thereby radiative heat flux—in high temperature, turbulent, non-premixed flames is discussed. The primary method of soot control is through strategic distribution of inert between the fuel and oxidizer to control the soot inception by affecting the chemical mechanism. The inherent separation of the inert from oxygen in oxy-combustion makes this method naturally suited for controlling soot and radiative heat flux in low-recycle oxy-combustion systems.

The method of Appendix B can also be extended to tri-axial systems. However, in this chapter, the focus will be to compare a normal diffusion flame with a tri-axial flame in terms of soot formation and its emission from the flame. The chapter will be divided into two parts—first, a simplified analytical model will be used to identify the regions where soot inception could happen in these two burner configurations. Then, the differences in the emission of soot from these two types of flames will be experimentally demonstrated for a turbulent gas flame. The results of this chapter will form the preliminary base for future investigation, with detailed diagnostics, of soot inception and evolution in tri-axial flames.

7.2 Soot inception limits—C/O Ratio and Kinetic Temperature Limits.

In both small lab-scale laminar flames and larger turbulent flames, the effect of the relative placement of inert between the oxidizer and fuel streams has been shown to significantly affect soot inception [58, 141-149]. Varying the amount of inert placed in the fuel and oxidizer streams can change both the temperature of the flame as well as the stoichiometric mixture fraction (Z_{st}) of the flame, where Z_{st} is defined as

$$Z_{st} = \left(1 + \frac{\nu_{O_2} W_{O_2} Y_{F,f}}{\nu_F W_F Y_{O_2,o}} \right)^{-1} \quad (7-1)$$

and where Y_i , ν_i , and W_i , respectively indicate the mass fraction, stoichiometric coefficient, and molecular weight of species i , and the subscripts f and o represent the fuel and oxidizer inlet streams. The mixture fraction at any point can be conceptually understood as the fraction of the material at that point that originated in the fuel stream, and the stoichiometric mixture fraction is

the mixture fraction at the location of stoichiometry, *i.e.*, at the flame [150]. A typical fuel-air flame has a low Z_{st} (≈ 0.05 for methane). As seen from Eq. 7-1, increasing the oxygen concentration in the oxidizer and/or decreasing the fuel concentration in the fuel stream increases Z_{st} .

There are two temperature bounds for soot in a non-premixed flame, one a lower temperature bound deep inside the fuel rich region, and the other a high temperature bound near the flame front. Regions of high Z , *i.e.*, deep in the fuel-rich side of the flame, are dominated by *fuel-pyrolysis pathways* towards acetylene and PAH (polycyclic aromatic hydrocarbons), which are the immediate precursors of soot. Fuel pyrolysis leads to the formation of 2-butyne-1-yl (C_4H_5-2), which is converted to benzene by addition of acetylene [141],



Since this reaction for C_4H_5-2 is exothermic and involves acetylene, it is found in fuel-rich regions away from the flame [141]. This low-temperature, fuel-pyrolysis pathway to benzene scales with fuel concentration at the inlet [141], and fuel dilution, which reduces the fuel concentration at the inlet, increases Z_{st} . The fuel pyrolysis process, and thus soot formation, requires a minimum temperature to overcome the activation energy barrier, and this low-temperature bound is dependent on the fuel concentration and scalar dissipation rate (strain rate) [143].

Close to the flame, *i.e.*, at $Z \approx Z_{st}$, on the fuel-rich side, the *propargyl self-combination pathway* to soot precursor formation dominates the soot formation [141, 151]. Propargyl (C_3H_3) is produced via the reaction of acetylene with methyl and methylene radicals supplied from the oxidation (flame) region:



This pathway is endothermic and hence requires higher temperatures. This pathway also produces H-radicals, and hence in regions where the H-radical concentrations are high due to H supplied from the fuel-oxidation reactions, a reduction or even reversal of this pathway to soot precursor formation can occur [141]. The carbon-to-oxygen atom ratio (C/O ratio) is correlated with the presence of H-radicals, and each fuel has a critical C/O ratio at which the H-radical concentration is high enough to prevent soot formation via the propargyl self-combination pathway, which for methane is approximately 0.55 [141-143, 152]. This constitutes the high-temperature bound for soot formation.

Thus, soot inception in a non-premixed flame occurs in the region between the low temperature bound, which is dictated by the kinetic temperature, and the high temperature bound, which is dictated by the critical C/O ratio. A flame with a smaller gap between these two bounds will form less soot, while a flame with a larger gap between these two bounds will form more soot, all else being constant [58, 141].

7.3 Tri-axial Burke-Schumann Flame Model

The classical Burke-Schumann flame model is a simplified model for co-flowing laminar flames [153]. Chung and Law modified the original Burke-Schumann model to include the effects of stream-wise diffusion, extending the model for large Peclet number flows [154]. Limited theoretical work exists on co-axial burners with multi-port configuration [155]. Chao and Axelbaum extended the Burke-Schumann model, with Chung and Law's modification, to tri-axial

systems for applications in flame synthesis [59]. Kumfer [156] and Ko et al. [155] used this model for hydrocarbon flames to investigate flame shapes with varying oxygen concentrations.

The main assumptions of the Burke-Schumann model are listed below:

- 1) The mass flux and temperature in the streamwise direction are constant and equal for each port. These conditions reduce to equal and uniform exit velocities of the fuel and oxidizer streams if the densities are assumed constant.
- 2) All physical properties in the system are constant.
- 3) The Lewis number is unity.
- 4) The fuel and oxidizer react irreversibly in a single step, with an infinite Damkohler number (flame sheet assumption).
- 5) The flow is isobaric, and the wall impermeable and adiabatic.
- 6) Transverse momentum transfer is negligible.
- 7) Body forces are zero (no buoyancy).

The Burke-Schumann model requires the assumption of constant mass flux from each port in the co-axial burner. This restriction, along with the assumption of negligible radial velocity, eliminates the need to solve the momentum equation. The result is a simplified model which can be solved analytically. Ko et al. [15] have attempted an extension of the model for unequal velocities from different streams, by neglecting shearing force and momentum transfer between streams with different velocities. Strictly speaking, this assumption will violate mass conservation, unless the different streams are assumed to have different densities.

The fundamental assumptions for the Burke-Schumann model, though restrictive, when analyzed carefully, are quite suitable for the SPOC process. In Chapters 4–6, significant emphasis was

placed on minimizing the effects of buoyancy, and the proposed boiler design effectively achieved this goal. Similarly, low mixing rates were achieved by minimizing the velocity difference between the various streams at the burner outlet, resulting in low transverse momentum transport. For SPOC, the Lewis number can be assumed to be unity because of turbulence.

Although the Burke-Schumann model is not a turbulent flame model, the simplicity of the model, and the design of the SPOC boilers with a low-mixing co-axial burner, allow it to be used for a simple comparison between normal and tri-axial flames. The model will only be used to help identify the basic differences and trends, For a more rigorous analysis and to match experimental results precisely, a more detailed and comprehensive CFD model would be required.

The basic conservation equations that are solved for the extended Burke-Schumann model are:

$$\rho u c_p \frac{\partial T}{\partial z} - \left[\frac{\partial}{\partial z} \left(k \frac{\partial T}{\partial z} \right) + \frac{1}{r} \frac{\partial}{\partial r} \left(kr \frac{\partial T}{\partial r} \right) \right] = \nu_F W_F q_F \omega \quad (7-5)$$

$$\rho u \frac{\partial Y_i}{\partial z} - \left[\frac{\partial}{\partial z} \left(\rho D_i \frac{\partial Y_i}{\partial z} \right) + \frac{1}{r} \frac{\partial}{\partial r} \left(\rho D_i r \frac{\partial Y_i}{\partial r} \right) \right] = \nu_i W_i \omega \quad (7-6)$$

where ρ is the gas density, u is the axial velocity, c_p is the specific heat at constant pressure, T is the absolute temperature, z is the axial distance from the burner, k is the gas conductivity, r is the radial distance from the axis, ν_i is the stoichiometric coefficient in the combustion reaction, W_i is the molecular weight, q_i is the heat of combustion, ω is the reaction rate, D_i is the molecular diffusivity, and Y_i is the mass fraction, with the subscript $i = F$ for fuel, O for oxidizer, and I for inert.

Using the coupling function formulation [150] after appropriate non-dimensionalization (see Appendix C), the equations to be solved reduce to

$$Pe \frac{\partial(\tilde{T} + \tilde{Y}_F)}{\partial \tilde{z}} - \frac{\partial^2(\tilde{T} + \tilde{Y}_F)}{\partial \tilde{z}^2} - \frac{1}{\tilde{r}} \frac{\partial}{\partial \tilde{r}} \left[\tilde{r} \frac{\partial(\tilde{T} + \tilde{Y}_F)}{\partial \tilde{r}} \right] = 0 \quad (7-7)$$

$$Pe \frac{\partial(\tilde{Y}_F - \tilde{Y}_O)}{\partial \tilde{z}} - \frac{\partial^2(\tilde{Y}_F - \tilde{Y}_O)}{\partial \tilde{z}^2} - \frac{1}{\tilde{r}} \frac{\partial}{\partial \tilde{r}} \left[\tilde{r} \frac{\partial(\tilde{Y}_F - \tilde{Y}_O)}{\partial \tilde{r}} \right] = 0 \quad (7-8)$$

$$Pe \frac{\partial(\tilde{Y}_I)}{\partial \tilde{z}} - \frac{\partial^2(\tilde{Y}_I)}{\partial \tilde{z}^2} - \frac{1}{\tilde{r}} \frac{\partial}{\partial \tilde{r}} \left[\tilde{r} \frac{\partial(\tilde{Y}_I)}{\partial \tilde{r}} \right] = 0 \quad (7-9)$$

where Pe is the Peclet number ($= \rho u r_c c_p / k$) and is based on the SO diameter. The non-dimensionalized quantities of the ones mentioned in Eqs. 7-5 and 7-6 are shown by tilde. Here, the inert equation (Eq. 7-9) does not require coupling to another equation, since the reaction term in the inert equation is inherently zero, i.e., it is a conserved scalar. The analytical solutions to these equations (Eqs. 7-7–9) are in the form of series solutions with Bessel functions of the first kind. For a tri-axial burner, with an inner oxidizer, fuel in the middle tube, and a secondary oxidizer surrounding the fuel (Figure 7-1), the flame sheet location (\tilde{r}_f, \tilde{z}_f) is determined by the solution to

$$\begin{aligned} & \tilde{Y}_{F,0} (\tilde{r}_b^2 - \tilde{r}_a^2) - \tilde{Y}_{F,0} \tilde{r}_a^2 - \tilde{Y}_{O,c} (1 - \tilde{r}_b^2) \\ & + 2 \sum_{n=1}^{\infty} \frac{(\tilde{Y}_{F,0} + \tilde{Y}_{O,c}) \tilde{r}_b J_1(k_n \tilde{r}_b) - (\tilde{Y}_{F,0} - \tilde{Y}_{O,c}) \tilde{r}_a J_1(k_n \tilde{r}_a)}{k_n J_0^2(k_n)} J_0(k_n \tilde{r}_f) \exp \left[\left(Pe - \sqrt{Pe^2 + 4k_n^2} \right) \tilde{z}_f / 2 \right] = 0 \end{aligned} \quad (7-10)$$

where J_0 and J_1 are the 0th and 1st order Bessel functions of the first kind, and the subscript f denotes flame.

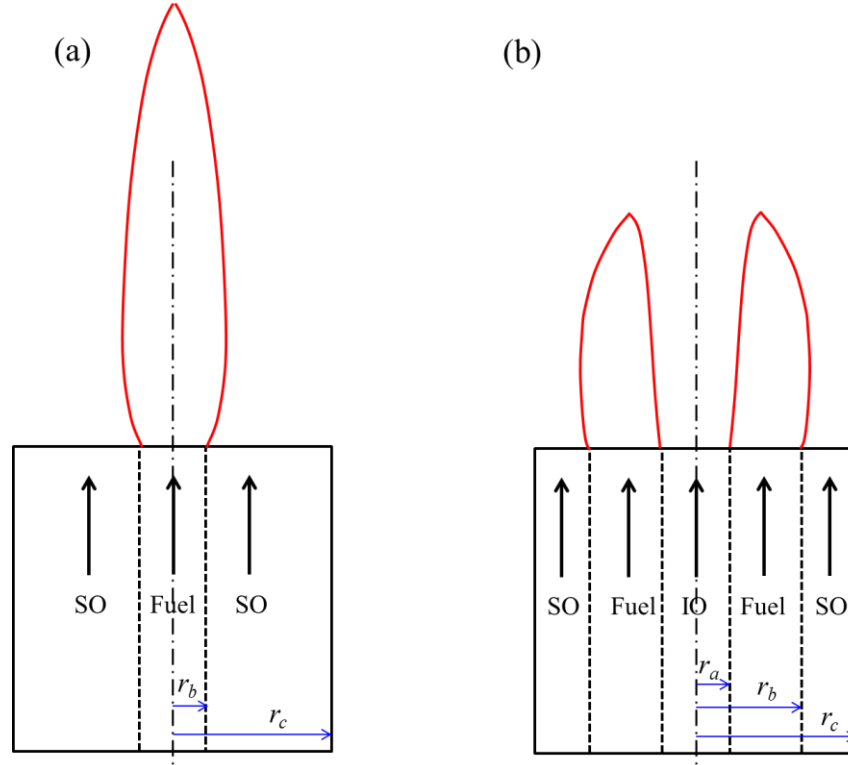


Figure 7-1. Schematic of (a) a normal flame and (b) a tri-axial flame. The red curves are shown as representatives of flames in the two configurations. Note: This is only a longitudinal section of an axisymmetric system.

Following the approach described in [143], the location for the minimum temperature for soot inception can be obtained, and the location (\tilde{r}, \tilde{z}) marking this low temperature boundary for soot inception can be obtained by setting the appropriate value of temperature in the equation below:

$$\tilde{T} = \tilde{T}_0 + \tilde{Y}_{O,0} \tilde{r}_a^2 + \tilde{Y}_{O,c} (1 - \tilde{r}_b^2) + 2 \sum_{n=1}^{\infty} \frac{\tilde{Y}_{O,0} \tilde{r}_a J_1(k_n \tilde{r}_a) - \tilde{Y}_{O,c} \tilde{r}_b J_1(k_n \tilde{r}_b)}{k_n J_0^2(k_n)} J_0(k_n \tilde{r}) \exp \left[\left(Pe - \sqrt{Pe^2 + 4k_n^2} \right) \frac{\tilde{z}}{2} \right] \quad (7-11)$$

The location of critical C/O ratio can be obtained by solving the distribution of the fuel and inert streams on the fuel side of the flame (Eqs. 7-12–14), and setting the appropriate value of the critical C/O—derived from [143]—in Eq. 7-14.

$$\begin{aligned} \tilde{Y}_F = & \tilde{Y}_{F,0}(\tilde{r}_b^2 - \tilde{r}_a^2) - \tilde{Y}_{F,0}\tilde{r}_a^2 - \tilde{Y}_{O,c}(1 - \tilde{r}_b^2) \\ & + 2 \sum_{n=1}^{\infty} \frac{(\tilde{Y}_{F,0} + \tilde{Y}_{O,c})\tilde{r}_b J_1(k_n \tilde{r}_b) - (\tilde{Y}_{F,0} - \tilde{Y}_{O,0})\tilde{r}_a J_1(k_n \tilde{r}_a)}{k_n J_0^2(k_n)} J_0(k_n \tilde{r}) \exp\left[\left(Pe - \sqrt{Pe^2 + 4k_n^2}\right) \frac{\tilde{z}}{2}\right] \end{aligned} \quad (7-12)$$

$$\begin{aligned} \tilde{Y}_I = & (\tilde{Y}_{I,a}\tilde{r}_a^2 + \tilde{Y}_{I,b}(\tilde{r}_b^2 - \tilde{r}_a^2) + \tilde{Y}_{I,c}(1 - \tilde{r}_b^2)) \\ & + 2 \sum_{n=1}^{\infty} \frac{\tilde{Y}_{I,a}\tilde{r}_a J_1(k_n \tilde{r}_a) + \tilde{Y}_{I,b}(\tilde{r}_b J_1(k_n \tilde{r}_b) - \tilde{r}_a J_1(k_n \tilde{r}_a)) - \tilde{Y}_{I,c}\tilde{r}_b J_1(k_n \tilde{r}_b)}{k_n J_0^2(k_n)} J_0(k_n \tilde{r}) \exp\left[\left(Pe - \sqrt{Pe^2 + 4k_n^2}\right) \frac{\tilde{z}}{2}\right] \end{aligned} \quad (7-13)$$

$$\left(\frac{C}{O}\right) = \frac{m(m+n/2)W_P}{(2m+n/2)W_F} \frac{\tilde{Y}_F}{1 - \tilde{Y}_I - \tilde{Y}_F} + \frac{m}{(2m+n/2)} \quad (7-14)$$

where \tilde{r}_i is the non-dimensionalized radius of the i^{th} tube as shown in Figure 7-1, m and n are the number of carbon and hydrogen atoms in the fuel respectively, W_P is the mean molecular weight of the product species (CO_2 and H_2O), and W_F is the molecular weight of the fuel.

The flame location, critical C/O ratio, and minimum temperature location for soot inception were obtained by solving these equations in MATLAB. The solutions for the normal Burke-Schumann flame are similar, and can be obtained by making appropriate adjustments to the sizes of the fuel and oxidizer tubes.

7.4 Comparison of Normal and Tri-axial Burke-Schumann Flame

To compare a normal and tri-axial flame in terms of soot inception limits, with SPOC as the application, the boundary conditions were chosen to have the same fuel, inert, and oxygen flow rate for the two configurations. For the tri-axial flame, pure oxygen is supplied through the innermost tube (inner oxidizer, IO), fuel is supplied through the middle tube with a composition of 63 vol% CH₄ and 37 vol% N₂, surrounded by the secondary oxidizer (SO) with a composition of 35 vol% O₂ and 65 vol% N₂. The total stoichiometric ratio is approximately 2.3, with an inner oxidizer stoichiometric ratio (SR_{IO}) of 0.68. This configuration of fuel, oxidizers and inert flow corresponds to Stage 1 in SPOC. The size of the burner (r_c) is set arbitrarily to 1 cm for the tri-axial configuration. The other tube sizes are then determined based on the stoichiometric ratios and the fuel and oxidizer compositions. The normal flame has no inner oxidizer, and the oxygen concentration of the surrounding oxidizer is 45.5 vol% to keep the same total oxygen and inert flow rates. The fuel composition is maintained the same at 63 vol% methane. The size of the burner (r_c) for the normal configuration is 0.995 cm to maintain the same fuel flow rate as the tri-axial case. The sizes of the various tubes for the two configurations are given in Table 7-1.

Table 7-1. Boundary conditions for the Burke-Schumann model.

Configuration	IO tube diameter, r_a (cm)	Fuel tube diameter, r_b (cm)	SO tube diameter, r_c (cm)	IO Stream [O ₂] (%v)	Fuel Stream [CH ₄] (%v)	SO Stream [O ₂] (%v)
Normal	0	0.308	0.995	-	62.7	36.8
Triaxial	0.357	0.472	1.000	100	62.7	45.5

When oxygen from the SO of the normal configuration is partially shifted to create a new IO stream of pure oxygen (i.e., the tri-axial configuration), a new flame front is created. The resulting double flame (as shown in Figure 7-1) has a larger surface area for the interaction of fuel with oxidizer, leading to faster burning, and a significantly reduced flame length. In Figure 7-2, the flame location for both normal and tri-axial flames is shown by the red curve. Compared to the normal flame, the tri-axial flame is not only shorter, but the fuel-rich region of the tri-axial flame is also narrower in the radial direction at any given axial location, due to an additional flame front.

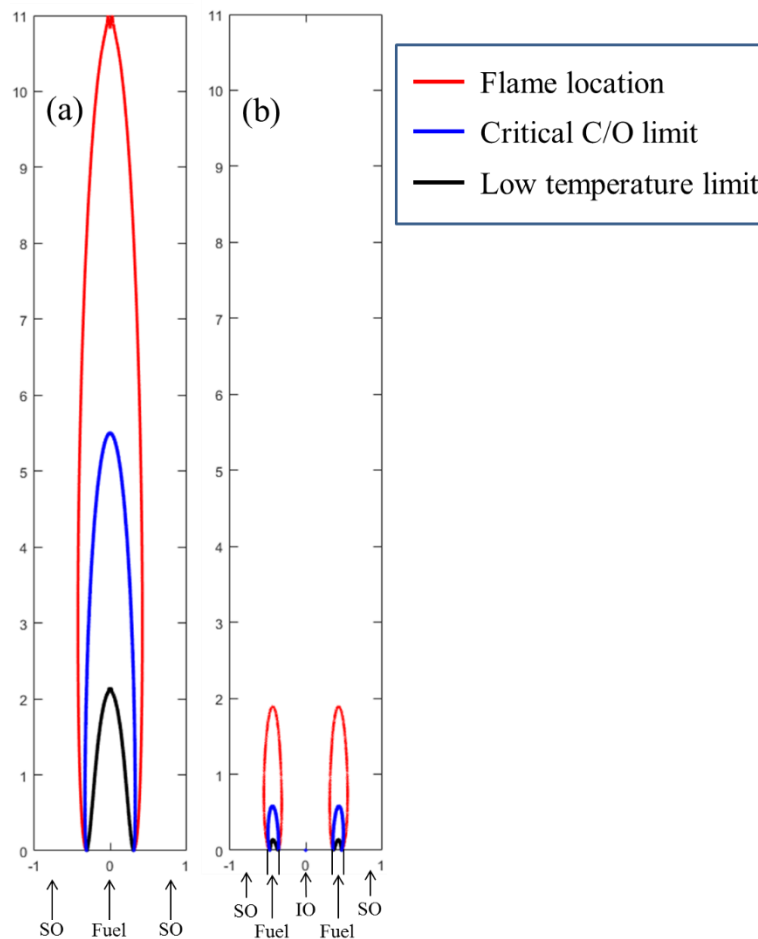


Figure 7-2. Comparison of (a) normal Burke-Schumann flame with (b) tri-axial Burke-Schumann flame. The region between the critical C/O limit and the low temperature limit marks the region for soot inception. Note: A 2D longitudinal section of an axisymmetric flame is shown here

In Figure 7-2, soot inception can occur in the region between the critical C/O ratio curve (blue) and the low temperature limit curve (black). Due to the reduced radial extent of the tri-axial fuel-rich region, and the increased penetration of the oxygen-containing species from the inner oxidizer side, the region for soot inception is significantly reduced. Furthermore, the shorter flame length also reduces the potential for growth of soot in the tri-axial flame.

It is important to note that there is a significant difference in the temperature profiles of the two cases, with the flame temperature in the normal configuration being lower than the inner flame of the tri-axial flame and higher than the outer flame. This could lead to difference in the soot inception rates. Though elegant and enlightening, the Burke-Schumann approximation cannot resolve these differences due to the simplifying assumptions in the model. To address this, the next section will focus on preliminary experimental results of exhaust soot measurements for the normal and tri-axial burner configurations.

7.5 Experimental Methods

All experiments were performed in a 2.44 m long, vertical, down-fired combustor (Figure 7-3). The shape of the first 0.86 m of the combustor is that of a frustum of a cone, with top and bottom diameters of 0.06 m and 0.14 m respectively. Downstream from this, the combustor is a cylinder 0.14 m in diameter and 1.58 m long. The exhaust gas from the combustor passes through a filter bag and is vented to the outside. The inner oxidizer is fed through a 0.022 m diameter central tube. The fuel (CH_4), along with the inert (N_2), is injected through a 0.032 m diameter co-axial annulus tube. The secondary oxidizer is fed through a co-axial annulus surrounding the fuel with a diameter of 0.06 m. The fuel and the two oxidizers are axially fed using flow straighteners. The burner was

sized to give sufficiently high velocity to minimize the effect of buoyancy at the inlet, and the conical shape was designed to minimize the effect of buoyancy even downstream by keeping the Richardson number low everywhere along the flame region, as described in Xia et al. [98] and demonstrated by Gopan et al. [157]. Briefly, the small initial reactor diameter ensures high velocity, and as the gases heat up and are generated during combustion, the diameter of the conical section is increased to accommodate the increased flow rate while maintaining a high velocity and thus low Richardson number. Along the axis, the combustor has 16 ports of 0.04 m diameter, located at every 0.15 m, starting 0.05 m downstream of the burner exit. When not being used for measurements, each port is plugged using the same refractory material as the combustor wall.

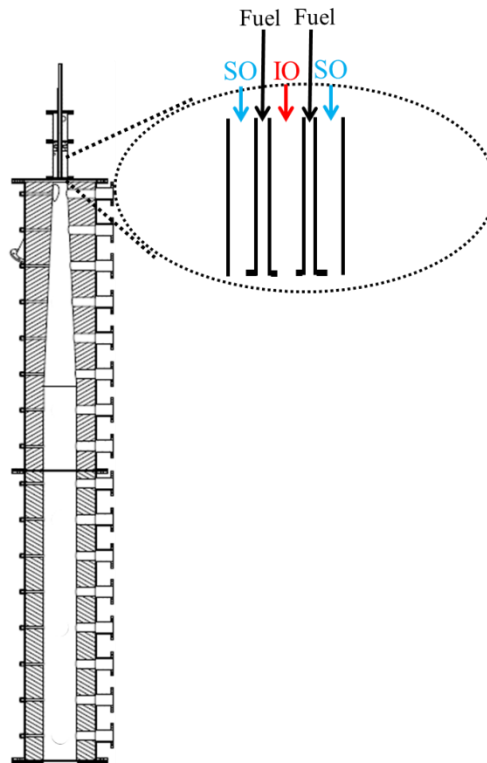


Figure 7-3. Combustor and burner design.

The operating conditions for the two burner configurations is provided in Table 7-2. In both cases the flames were turbulent. Similar to the Burke-Schumann modeling study, in both normal and tri-axial cases, the fuel, inert and oxygen flow were kept constant. The only difference between the normal and tri-axial configuration was the shifting of the placement of some oxygen from the SO to the IO. Thus, the oxygen concentration in the SO for tri-axial flames is lower. Overall, both flames had sufficient (and equal) excess oxygen. The measurements were conducted 2.18 m from the burner nozzle. In both cases, the experiment was conducted with “cold” (room temperature) reactor walls and was concluded within 15 min of start up to ensure that the wall temperature remained low, and post flame, the excess oxidizer acts as a quench to prevent ignition of soot particles downstream of the flame.

Table 7-2. Operating conditions for the two configurations.

Configuration	IO Flow (m ³ /h) ^a (pure oxygen)	Fuel stream flow (m ³ /h) ^a	Fuel stream [CH ₄] (%v)	SO Flow (m ³ /h) ^a	SO Stream [O ₂] (%v)	<i>SR</i> _{IO}	<i>SR</i> _{Total}
Normal	0	3.1	62.7	19.7	36.8	0	2.3
Triaxial	2.7	3.1	62.7	17.0	45.5	0.7	1.6

The primary objective of the experiments was to obtain the exhaust soot measurements (concentrations and size distribution) for the two flames. To obtain the total concentration and the size distribution of the soot particles in the exhaust gases, a differential mobility analyzer (DMA; model 3080, TSI inc.) was used as a classifier, with a sheath flow rate of 15 l/min and an aerosol flow rate of 1.5 l/min. The size classified particles transmitted through the DMA were sent to a condensation particle counter (CPC; model 3776, TSI Inc.) to obtain a number count for the particular size. The DMA and CPC were operated in tandem as a scanning mobility particle sizer (SMPS), with 60 s upward voltage scans applied, and 15 s downscans.

7.6 Experimental Results

The normal configuration resulted in a flame with a length of about 1.73 m, while the tri-axial flame had a length of about 0.45 m. This ratio is similar to that predicted from the Burke-Schumann model. The tri-axial flame has a very small amount of soot in the exhaust, with a total number concentration of about $1 \times 10^4 \text{ \#/cm}^3$, while the normal flame has a total concentration close to $1 \times 10^6 \text{ \#/cm}^3$. The high particle number concentration in the normal flame is also seen in the particle size distributions shown in Figure 7-4. The soot mode in the tri-axial configuration occurs at about 14 nm, while in the normal configuration it occurs at approximately 84 nm. The results clearly show that soot emissions in the normal flame is much higher than in the tri-axial flame.

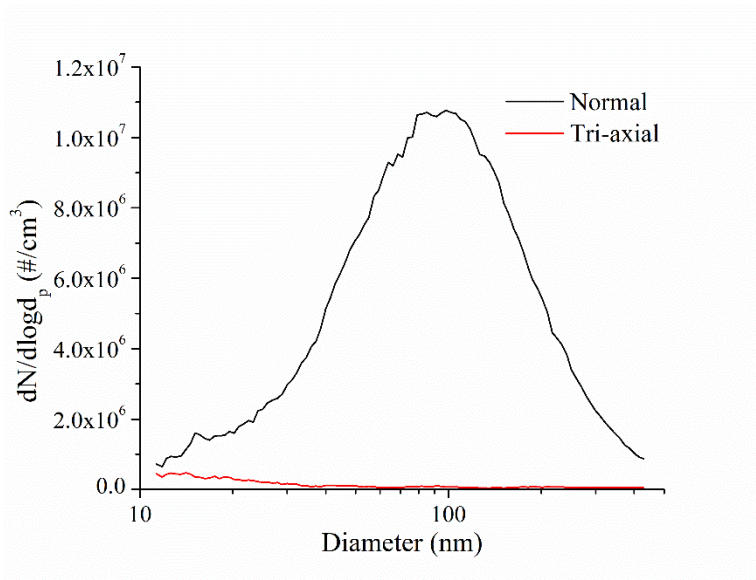


Figure 7-4. Particle size distribution of soot—comparison of normal configuration and tri-axial configuration.

7.7 Conclusions

A comparison of soot produced from methane flames in a normal configuration axial flow burner and a tri-axial burner—with pure oxygen as the inner oxidizer—shows much higher soot emission from the normal flame. A Burke-Schumann model extension into the tri-axial configuration shows that the region where soot inception could occur is significantly smaller for the tri-axial configuration than the normal configuration. While these results are preliminary, and are currently demonstrated only for gas flames, they can be extrapolated to solid fuel combustion. Most soot in solid-fuel combustion is formed within the volatile flame envelope. Using the chemical percolation devolatilization (CPD) model [129] to extract the volatile atomic composition, we can see that the carbon-to-hydrogen ratio of, for example, PRB coal (1.1:3.2) is close to that of methane (1:4). There are several differences between coal volatiles and methane, such as the presence of oxygen and a mixture of hydrocarbons in coal volatiles, as well as the difference in the release location of volatiles, which could affect the exact differences in the amount of soot inception. However, the comparison between a normal and tri-axial burner configuration using methane as a surrogate for coal volatiles can provide a reasonable first-approximation comparison.

Chapter 8

Summary and Recommendations for Future Work

The primary achievement of this work was the development of a new means of utilizing the vast and low cost coal resource in an efficient and economic manner to produce electric power with the least environmental burden.

The existing technologies for utilization of coal with reduced carbon dioxide emissions to minimize the anthropogenic impact on the global climate are both cost prohibitive and inefficient. Oxy-fuel combustion is one such method for minimizing the carbon dioxide emission from power plants. The primary causes for low efficiency and high cost in oxy-combustion are the auxiliary loads for air separation to produce oxygen, large recycle of flue gas to the boiler to control the flame temperature, and the carbon dioxide purification to meet the standards for utilization or sequestration. Although, advances are being made in the air separation and CO₂ purification technologies, those advances are not sufficient to reduce costs and increase efficiency enough for the acceptance of the process. On the other hand, the staged, pressurized oxy-combustion (SPOC) process proposed in this dissertation minimizes flue gas recycle and utilizes the latent heat of condensation of flue gas moisture to increase the plant efficiency by more than 6 %-pts. The cost of electricity from a SPOC plant with more than 90% CO₂ captured would be less than 35% higher

than an equivalent air-fired plant with no CO₂ capture, thereby meeting the U.S. Dept. of Energy target for carbon capture equipped power plants.

A brief summary of the dissertation is presented below.

8.1 Process Development

- A new staged, pressurized oxy-combustion (SPOC) process is proposed for power generation with carbon capture. The process pressurizes the oxy-combustion process to extract the latent heat of flue gas moisture condensation at a higher temperature, thereby integrating it into the steam Rankine cycle.
- SPOC also uses staging to reduce flue gas recycle. Multiple boilers are connected in series, with the exhaust gas from the first boiler (stage) entering the next stage and so on. Fuel and oxygen are staged in these multiple boilers, with the initial stages highly over-ventilated, while the final stage operates at near stoichiometry. The well-mixed temperature in each stage is maintained similar to air-fired combustion.
- In each stage, part of the heat from the combustion of the fuel in the stage with the oxidizer is transferred to the steam, until the heat transfer rate becomes low due to the reduced temperature of the gas stream. At this point, the gas stream is transferred to the next stage, where more fuel and oxygen are injected, and the same process is repeated.
- The flue gas from the final stage, after sufficient cooling in an economizer and particulate removal is fed to a direct contact column (DCC) for the extraction of latent heat of flue gas moisture.

- The combustion pressure is chosen to be at least 16 bar to utilize the same DCC as an integrated pollutant removal unit, capturing most of the SO_x, NO_x, and Hg. This integrated removal of pollutant is activated by the promotion of some lead-chamber-like reactions at high pressure (> 14 bar) and low temperature. The advantage of choosing a slightly higher combustion pressure is that all moving parts are eliminated between the production of the acid gases (SO_x and NO_x) and their cleanup, preventing damage to equipment due to acid condensation.
- The cleaned flue gas is purified in an auto-refrigeration CO₂ purification unit, with a distillation column to achieve the highest purity standards published.
- The net plant efficiency of the SPOC process operating at 16 bar combustion pressure, and a single reheat, supercritical steam Rankine cycle (242 bar/593°C/593°C) firing a low-rank, sub-bituminous, Powder River Basin (PRB) coal is 35.7% (HHV), and the increase in cost of electricity is less than the U.S. Dept. of Energy target of 35%.
- Replacing the low efficiency direct contact column by an indirect heat exchanger to extract the latent heat of condensation of flue gas moisture can increase the efficiency by about 0.5 %-pts., but will also lead to an increase in cost due to the requirement of expensive corrosion resistant materials of construction for such a heat exchanger.
- The operating pressure of the boilers has little impact on plant efficiency beyond 16 bar. On the other hand, the moisture content in the fuel can significantly impact the plant efficiency. The dependence of plant efficiency on the as-fired moisture content in the fuel is non-linear. The loss in plant efficiency with increasing moisture is small at low moisture content, but it sharply increases beyond the heat saturation point in the low pressure regenerators in the steam Rankine cycle. It is therefore recommended to not feed the coal as coal-water slurry, but to dry

feed the fuel. Note that SPOC is more efficient for all moisture levels than its atmospheric pressure counterpart.

- The impact of flue gas recycle ratio on plant efficiency is also non-linear, with low recycle ratios ($< \sim 35\%$) resulting in a small loss in efficiency ($< 1\%$ -pt.). However, further increase in recycle ratio can significantly reduce the plant efficiency by as much as 4 %-pts for a 70% flue gas recycle ratio.
- Process intensification by utilizing an advanced ultra-supercritical steam Rankine cycle with double reheat can lead to a net plant efficiency of almost 41% (HHV), while firing a low rank, sub-bituminous coal.
- The SPOC process, due to the flue gas moisture condensation and high efficiency, requires less fresh water than both air-fired combustion and atmospheric oxy-combustion as cooling water make-up. In fact, it produces more water than is required for cooling tower make-up.

8.2 Burner and Boiler Development

- Since the SPOC boilers are pressure vessels, they are designed mainly as cylinders with high aspect ratios, unlike the traditional cuboidal box type boilers. This high aspect ratio and the high flame temperature resulting from the reduced flue gas recycle lead to a number of burner and boiler design requirements, such as:
 - Avoid flame impingement.
 - Reduce mixing between the streams to distribute heat release.
 - Control wall heat flux from the high temperature, low recycle oxy-combustion flame.

- Control near wall oxygen concentration even with low flue gas recycle, to provide safe operating conditions.
- Avoiding external or internal recirculation to avoid flame impingement and to minimize slagging and fouling. This includes minimizing buoyancy effects.
- The burner proposed for the SPOC process is a low mixing (low relative velocity between streams), tri-axial burner with fuel in the middle tube, an inner oxidizer (pure oxygen), and an outer oxidizer (controlled composition, set to 35 vol% O₂ as an example).
- The high optical density in the boiler, created by the increased pressure and reduced flue gas recycle, is utilized in the design to control wall radiative heat flux in the high temperature system to manageable levels using radiative trapping.
- The importance of the radiation penetration layer in the control of radiative heat transfer to the walls is discussed. This layer can be thought of as a radiation boundary layer, and to a high degree of accuracy, the temperature in this layer dictates the radiative heat flux to the wall.
- Buoyancy-induced internal recirculation can result in a high wall heat flux due to increase in temperature in the radiation penetration layer. To avoid buoyancy induced recirculation, an initial section in the shape of a conical frustum is proposed, such that the Richardson number is kept low throughout the boiler.
- Boiler modifications in the form of small wall-rings are proposed to allow for flexible operation. The wall-rings increase advection and maintaining a low Richardson number at various thermal loads (turndowns).
- A high wall heat flux is maintained throughout the SPOC boilers to maximize heat transfer rates (while not exceeding material constraints) to minimize boiler tube surface area. Since the

boiler cost is dictated by the tube surface area required, a lower tube surface area will lead to lower cost boilers.

- Since the SPOC boilers have high temperature flames with low mixing, their sooting tendencies were studied using methane as the surrogate for coal volatiles. A simplified laminar flame analytical model was used to compare the potential regions of soot inception between a normal diffusion flame and a tri-axial flame configuration. The tri-axial flame was shown to have a much smaller region for soot inception. An experimental investigation into the exhaust soot concentration and particle size distribution from a turbulent methane flame with SPOC type conditions also showed negligible soot in the tri-axial configuration, while much higher soot was observed with the normal configuration, proving the effectiveness of the tri-axial arrangement to minimize soot in SPOC.

8.3 Recommendations for Future Works

- In recent years, significant interest has been generated by the potential of supercritical CO₂ cycles to increase plant efficiency. The sCO₂ was originally designed for nuclear power plant applications, but has also been proposed recently for natural gas and coal combustion as a means to achieve very high efficiencies. However, the sCO₂ cycles are not suited for low grade heat utilization. Since SPOC process relies on the efficient integration of low grade heat into the steam Rankine cycle to create the highest efficiency oxy-coal process, direct utilization of these proposed cycles may not be suitable. However, experience from low grade heat utilization in process industry can be applied in the SPOC process to design a combined cycle power plant with sCO₂ in the topping cycle and an organic Rankine cycle

(ORC) or a Kalina cycle as the bottoming cycle. Preliminary analysis has indicated that such a combined cycle could result in a very high efficiency power plant.

- The radiative characteristics are related to the particle size distribution of ash in the SPOC boilers. In pressurized systems, ash fragments more than in atmospheric pressure systems. High temperatures, resulting from low flue gas recycle ratio, also promote ash fragmentation. It is important to determine the level of fragmentation of the ash particles in the SPOC boilers as that can help better model the level of control provided by radiative trapping. Higher fragmentation will increase the trapping efficiency.
- The CFD models used have not yet been fully validated under the conditions of SPOC. They have been reasonably validated under atmospheric pressure conditions, however due to lack of extensive experimental work under SPOC type conditions, complete validation is lacking. With the recent commissioning of the pressurized reactor at Washington University, complete validation should be undertaken and the model constants adjusted accordingly.
- Soot in tri-axial flames is not studied very well. A more extensive experimental investigation of soot in tri-axial flames using laser induced incandescence (LII) can provide insights into the inception regions and volume fraction, which can then be modeled and compared with the theory of soot inception limits.

References

- [1] International Energy Outlook. 2011. U.S. Energy Information Administration.
- [2] World Population Prospects: The 2015 revision. 2015. United Nations.
- [3] Larcher, D. and Tarascon, J., Towards greener and more sustainable batteries for electrical energy storage. *Nature chemistry*. 2015. 7(1): p. 19-29.
- [4] Key world energy statistics. 2016. International Energy Agency.
- [5] World energy scenarios. 2016. World Energy Council.
- [6] The sustainable development agenda. Retrieved June 7th, 2017.; Available from: <http://www.un.org/sustainabledevelopment/development-agenda/>.
- [7] Annual energy outlook 2011 with projections to 2035. 2011. U.S. Energy Information Administration.
- [8] India Energy Outlook. 2015. International Energy Agency.
- [9] International Energy Outlook. 2016. U.S. Energy Information Agency.
- [10] China - International energy data and analysis. 2015. U.S. Energy Information Administration.
- [11] India, R. O., Intended nationally determined contribution (INDC) for the UNFCCC, 2015.
- [12] China, P. S. R. O., Intended nationally determined contribution (INDC) for the UNFCCC, 2015.
- [13] Houghton, J. T., et al., *Climate change 2001: the scientific basis*. Vol. 881. 2001: Cambridge University Press Cambridge.
- [14] Karl, T. R. and Trenberth, K. E., Modern Global Climate Change. *Science*. 2003. 302(5651): p. 1719-1723.
- [15] Pacala, S. and Socolow, R., Stabilization Wedges: Solving the Climate Problem for the Next 50 Years with Current Technologies. *Science*. 2004. 305(5686): p. 968-972.
- [16] Ghoniem, A. F., Needs, resources and climate change: Clean and efficient conversion technologies. *Progress in Energy and Combustion Science*. 2011. 37(1): p. 15-51.
- [17] Thiruvengkatachari, R., et al., Post combustion CO₂ capture by carbon fibre monolithic adsorbents. *Progress in Energy and Combustion Science*. 2009. 35(5): p. 438-455.

- [18] Lawal, A., et al., Dynamic modelling and analysis of post-combustion CO₂ chemical absorption process for coal-fired power plants. *Fuel*. 2010. 89(10): p. 2791-2801.
- [19] Rao, A. B. and Rubin, E. S., A technical, economic, and environmental assessment of amine-based CO₂ capture technology for power plant greenhouse gas control. *Environmental Science & Technology*. 2002. 36(20): p. 4467-4475.
- [20] Aboudheir, A., et al., Kinetics of the reactive absorption of carbon dioxide in high CO₂-loaded, concentrated aqueous monoethanolamine solutions. *Chemical engineering science*. 2003. 58(23): p. 5195-5210.
- [21] Ko, J.-J. and Li, M.-H., Kinetics of absorption of carbon dioxide into solutions of N-methyldiethanolamine+ water. *Chemical engineering science*. 2000. 55(19): p. 4139-4147.
- [22] Mandal, B., Biswas, A. and Bandyopadhyay, S., Absorption of carbon dioxide into aqueous blends of 2-amino-2-methyl-1-propanol and diethanolamine. *Chemical engineering science*. 2003. 58(18): p. 4137-4144.
- [23] Bobicki, E. R., et al., Carbon capture and storage using alkaline industrial wastes. *Progress in Energy and Combustion Science*. 2012. 38(2): p. 302-320.
- [24] Zhao, C., et al., Capturing CO₂ in flue gas from fossil fuel-fired power plants using dry regenerable alkali metal-based sorbent. *Progress in Energy and Combustion Science*. 2013. 39(6): p. 515-534.
- [25] Brown, T., Coal gasification—combined cycles for electricity production. *Progress in Energy and Combustion Science*. 1982. 8(4): p. 277-301.
- [26] Craig, K. R. and Mann, M. K., Cost and performance analysis of biomass-based integrated gasification combined-cycle (BIGCC) power systems. 1996: National Renewable Energy Laboratory Golden, CO.
- [27] Descamps, C., Bouallou, C. and Kanniche, M., Efficiency of an Integrated Gasification Combined Cycle (IGCC) power plant including CO₂ removal. *Energy*. 2008. 33(6): p. 874-881.
- [28] Emun, F., et al., Integrated gasification combined cycle (IGCC) process simulation and optimization. *Computers & chemical engineering*. 2010. 34(3): p. 331-338.
- [29] Joshi, M. M. and Lee, S., Integrated gasification combined cycle—a review of IGCC technology. *Energy Sources*. 1996. 18(5): p. 537-568.
- [30] Kanniche, M. and Bouallou, C., CO₂ capture study in advanced integrated gasification combined cycle. *Applied Thermal Engineering*. 2007. 27(16): p. 2693-2702.

- [31] Manzoloni, G., Macchi, E. and Gazzani, M., CO₂ capture in Integrated Gasification Combined Cycle with SEWGS–Part B: Economic assessment. *Fuel*. 2013. 105: p. 220-227.
- [32] Maurstad, O., An overview of coal based integrated gasification combined cycle (IGCC) technology. Massachusetts Institute of Technology, Laboratory for Energy and the Environment, Report No. LFEE. 2005. 2.
- [33] Chen, L., Yong, S. Z. and Ghoniem, A. F., Oxy-fuel combustion of pulverized coal: Characterization, fundamentals, stabilization and CFD modeling. *Progress in Energy and Combustion Science*. 2012. 38(2): p. 156-214.
- [34] \$7.5 billion Kemper power plant suspends coal gasification. 2017 07/19/2017]; Available from: <https://arstechnica.com/business/2017/06/7-5-billion-kemper-power-plant-suspends-coal-gasification/>.
- [35] Pulverized Coal Oxycombustion Power Plants. Vol. 1: Bituminous Coal to Electricity, rev. 2; Report DOE/NETL-2007/1291. 2008. U.S. Department of Energy National Energy Technology Laboratory.
- [36] Abraham, B., et al., Coal-oxygen process provides CO₂ for enhanced recovery. *Oil Gas J. (United States)*. 1982. 80(11).
- [37] Steinberg, M., History of CO₂ greenhouse gas mitigation technologies. *Energy conversion and management*. 1992. 33(5): p. 311-315.
- [38] Horn, F. L. and Steinberg, M., Control of carbon dioxide emissions from a power plant (and use in enhanced oil recovery). *Fuel*. 1982. 61(5): p. 415-422.
- [39] Stanger, R., et al., Oxyfuel combustion for CO₂ capture in power plants. *International Journal of Greenhouse Gas Control*. 2015.
- [40] Matuszewski, M., Brasington, R. and Woods, M. Advancing oxycombustion technology for bituminous coal power plants: An R&D guide. in *Carbon Management Technology Conference*. 2012. Carbon Management Technology Conference.
- [41] Zebian, H., Gazzino, M. and Mitsos, A., Multi-variable optimization of pressurized oxy-coal combustion. *Energy*. 2012. 38(1): p. 37-57.
- [42] Zheng, L., *Oxy-fuel combustion for power generation and carbon dioxide (CO₂) capture*. 2011: Elsevier.
- [43] Gao, X., et al., Roles of Inherent Fine Included Mineral Particles in the Emission of PM₁₀ during Pulverized Coal Combustion. *Energy & Fuels*. 2012. 26(11): p. 6783-6791.

- [44] Quality Guidelines for Energy System Studies: CO₂ Impurity Design Parameters; Report DOE/NETL - 341/081911. 2012. U.S. Department of Energy National Energy Technology Laboratory.
- [45] Gopan, A., Kumfer, B. M. and Axelbaum, R. L., Effect of Operating Pressure and Fuel Moisture on Net Plant Efficiency of a Staged, Pressurized Oxy-Combustion Power Plant. *International Journal of Greenhouse Gas Control*. 2015.
- [46] Gopan, A., et al., Process design and performance analysis of a Staged, Pressurized Oxy-Combustion (SPOC) power plant for carbon capture. *Applied Energy*. 2014. 125(0): p. 179-188.
- [47] Cost and Performance for Low-Rank Pulverized Coal Oxycombustion Energy Plants; Report DOE/NETL - 401/093010. 2010. U.S. Department of Energy National Energy Technology Laboratory.
- [48] Deng, S. M. and Hynes, R., Thermodynamic Analysis and Comparison on Oxy-Fuel Power Generation Process. *Journal of Engineering for Gas Turbines and Power-Transactions of the Asme*. 2009. 131(5).
- [49] Hong, J., et al. Performance of the pressurized oxy-fuel combustion power cycle with increasing operating pressures. in *The 34th International Technical Conference on Clean Coal & Fuel Systems*. 2009. Clearwater, FL.
- [50] Hong, J. S., et al., Analysis of oxy-fuel combustion power cycle utilizing a pressurized coal combustor. *Energy*. 2009. 34(9): p. 1332-1340.
- [51] White, V., personal communication, May 2013., 2013.
- [52] Gazzino, M. and Benelli, G. Pressurised Oxy-Coal Combustion Rankine-Cycle for Future Zero Emission Power Plants: Process Design and Energy Analysis. in *ASME Conference Proceedings*. 2008.
- [53] Benelli, G., et al. ISOTHERM®: a new oxy-combustion process to match the zero emission challenge in power generation. in *The 7 th High Temperature Air Combustion and Gasification International Symposium, Phuket, Thailand*. 2008.
- [54] Hagi, H., et al. Towards Second Generation Oxy-Pulverized Coal Power Plants: Energy Penalty Reduction Potential of Pressurized Oxy-Combustion Systems. in *International Conference on Greenhouse Gas Technologies (GHGT)*. 2014. Austin, TX: Energy Procedia.

- [55] Kobayashi, S. and Bool, L. E., Direct oxy-coal combustion with minimum or no flue gas recycle, in Oxy-fuel combustion for power generation and carbon dioxide capture, Zheng, L., Editor. 2011. Woodhead Publishing.
- [56] Goanta, A., et al. Controlled Staging with Non-Stoichiometric Burners for Oxy-fuel Processes - Numerical Validation. in 33rd International Technical Conference on Coal Utilization & Fuel Systems. 2008.
- [57] Becher, V., et al., A combustion concept for oxyfuel processes with low recirculation rate - Experimental validation. *Combustion and Flame*. 2011. 158(8): p. 1542-1552.
- [58] Gopan, A., et al., Effects of Inert Placement (Zst) on Soot and Radiative Heat Flux in Turbulent Diffusion Flames. *Energy & Fuels*. 2017.
- [59] Chao, B. H. and Axelbaum, R. L., Triaxial Burke-Schumann Flames with Applications to Flame Synthesis. *Combustion Science and Technology*. 2000. 156(1): p. 291-314.
- [60] Bohn, J. P., et al., Flame temperatures and species concentrations in non-stoichiometric oxycoal flames. *Fuel*. 2011. 90(10): p. 3109-3117.
- [61] Morehead, H., Siemens Global Gasification Update, in *Designing & Operating US Substitue Natural Gas Plants 2008*: Houston, TX.
- [62] Maroto-Valer, M. M., ed. *Developments and innovation in carbon dioxide (CO₂) capture and storage technology*. Vol. Volume 1: Carbon dioxide (CO₂) capture, transport and industrial applications. 2010. Woodhead Publishing Limited.
- [63] Topical Report, Linear Extrusion 400 Tons/Day Dry Solids Pump. 2008.
- [64] Final Report, Proof of principal test to feed and meter granular coal into 450 psig gas pressure. 2000.
- [65] Quality Guidelines for Energy System Studies: Specifications for Selected Feedstocks; Report DOE/NETL - 341/081911. 2012. U.S. Department of Energy National Energy Technology Laboratory.
- [66] Quality Guidelines for Energy System Studies: Process Modeling Design Parameters; Report DOE/NETL - 341/042613. 2013. U.S. Department of Energy National Energy Technology Laboratory.
- [67] Quality Guidelines for Energy System Studies: Process Modeling Design Parameters, rev. 2; Report DOE/NETL - 341/081911. 2012. U.S. Department of Energy National Energy Technology Lab.

- [68] Advancing Oxycombustion Technology for Bituminous Coal Power Plants: An R&D Guide; Report DOE/NETL - 2010/1405. 2012. U.S. Department of Energy National Energy Technology Laboratory.
- [69] White, V., et al., The Air Products Vattenfall Oxyfuel CO₂ Compression and Purification Pilot Plant at Schwarze Pumpe. *Energy Procedia*. 2013. 37: p. 1490-1499.
- [70] White, V., et al., Purification of oxyfuel-derived CO₂. *International Journal of Greenhouse Gas Control*. 2010. 4(2): p. 137-142.
- [71] Bell, D. A., Towler, B. F. and Fan, M., *Coal gasification and its applications*. 2010: William Andrew.
- [72] Xiong, J., et al., Simulation Study of an 800 MWe Oxy-combustion Pulverized-Coal-Fired Power Plant. *Energy & Fuels*. 2011. 25(5): p. 2405-2415.
- [73] Verhoff, F. and Banchemo, J., Predicting dew points of flue gases. *Chem. Eng. Prog.* 1974. 70(8): p. 71-72.
- [74] Okkes, A. G., Get acid dew point of flue gas. *Journal Name: Hydrocarbon Process.; (United States); Journal Volume: 66:7. 1987: p. Medium: X; Size: Pages: 53-56.*
- [75] Zheng, L., Pomalis, R. and Clements, B. Technical feasibility study of TIPS process and comparison with other CO₂ capture power generation processes. in *The 32nd International Technical Conference on Coal Utilization and Fuel Systems*. 2007. Clearwater, FL.
- [76] Ellison, T. K. and Eckert, C. A., The oxidation of aqueous sulfur dioxide. 4. The influence of nitrogen dioxide at low pH. *J. Phys. Chem.* 1984. 88(11): p. 2335-2339.
- [77] White, V., Allam, R. and Miller, E. Purification of Oxyfuel-Derived CO₂ for Sequestration or EOR. in *Technical paper, 8th International Conference on Greenhouse Gas Control Technologies*. 2006. Trondheim, Norway.
- [78] Iloje, C., et al. Process modeling and analysis of CO₂ purification for oxy-coal combustion. in *The 35th International Technical Conference on Clean Coal & Fuel Systems*. 2010. Clearwater, FL.
- [79] Liémans, I., et al., SO_x and NO_x absorption based removal into acidic conditions for the flue gas treatment in oxy-fuel combustion. *Energy Procedia*. 2011. 4(0): p. 2847-2854.
- [80] Normann, F., et al., Nitrogen and sulphur chemistry in pressurised flue gas systems: A comparison of modelling and experiments. *International Journal of Greenhouse Gas Control*. 2013. 12(0): p. 26-34.

- [81] Pétrissans, S. M., Pétrissans, A. and Zoulalian, A., Experimental study and modelling of mass transfer during simultaneous absorption of SO₂ and NO₂ with chemical reaction. *Chemical Engineering and Processing: Process Intensification*. 2005. 44(10): p. 1075-1081.
- [82] Lee, S., Speight, J. G. and Loyalka, S. K., *Handbook of alternative fuel technologies*. 2007: crc Press.
- [83] Salvador, C. Modeling, design, and pilot-scale experiments of CANMET's advanced oxy-fuel/steam burner. in *2nd Workshop of the IEA GHG International Oxy-Combustion Research Network*. 2007. Wndsor, CT.
- [84] Zebian, H., et al., Optimal design and operation of pressurized oxy-coal combustion with a direct contact separation column. *Energy*. 2012.
- [85] Shah, M. M., Carbon dioxide compression and purification technology, in *Oxy-fuel combustion for power generation and carbon dioxide (CO₂) capture*, Zheng, L., Editor. 2011. Woodhead Publishing, Limited.
- [86] *Engineering and Economic Evaluation of 1300°F (700°C) Series Oxy-PC Power Plant: Interim Report #1023870*. 2012. EPRI.
- [87] Karabulut, H. and Ataer, Ö. E., Numerical solution of boundary layer equations in compressible cross-flow to a cylinder. *International journal of heat and mass transfer*. 1998. 41(17): p. 2677-2685.
- [88] *Current and Future Technologies for Power Generation with Post-Combustion Carbon Capture; Report DOE/NETL - 2012/1557*. 2012. U.S. Department of Energy National Energy Technology Laboratory.
- [89] De Visser, E., et al., Dynamis CO₂ quality recommendations. *International Journal of Greenhouse Gas Control*. 2008. 2(4): p. 478-484.
- [90] Hagi, H., et al., Optimal Integration of the Flue Gas Heat for the Minimization of the Energy Penalty of Oxy-fired Power Plants. *Energy Procedia*. 2014. 63: p. 7359-7366.
- [91] Hagi, H., Neveux, T. and Le Moullec, Y., Efficiency evaluation procedure of coal-fired power plants with CO₂ capture, cogeneration and hybridization. *Energy*. 2015. 91: p. 306-323.
- [92] *Updated Costs (June 2011 Basis) for Selected Bituminous Baseline Cases; Report DOE/NETL - 341/082312*. 2012. U.S. Department of Energy National Energy Technology Laboratory.

- [93] Quality Guidelines for Energy System Studies: Capital Cost Scaling Methodology; Report DOE/NETL - 341/013113. 2013. U.S. Department of Energy National Energy Technology Laboratory.
- [94] Roberts, D., Harris, D. and Wall, T., Total pressure effects on chemical reaction rates of chars with O₂, CO₂ and H₂O. *Fuel*. 2000. 79(15): p. 1997-1998.
- [95] Improving the Efficiency of Coal-Fired Power Plants for Near Term Greenhouse Gas Emissions Reductions; Report DOE/NETL - 2010/1411. 2010. U.S. Department of Energy National Energy Technology Laboratory.
- [96] Zheng, L., et al. Optimization of a high pressure oxy-fuel combustion process for power generation and CO₂ capture. in International Technical Conference on Coal Utilization & Fuel Systems. 2010. Clearwater, Florida, USA.
- [97] Hong, J., et al., Operating Pressure dependence of the pressurized oxy-fuel combustion power cycle. *Energy*. 2010. 35: p. 9.
- [98] Xia, F., et al., Pressurized oxy-combustion with low flue gas recycle: Computational fluid dynamic simulations of radiant boilers. *Fuel*. 2016. 181: p. 1170-1178.
- [99] Murciano, L. T., et al., Sour compression process for the removal of SO_x and NO_x from oxyfuel-derived CO₂. *Energy Procedia*. 2011. 4(0): p. 908-916.
- [100] Ajdari, S., et al., On the liquid phase chemistry in pressurized flue gas cleaning systems: the effect of process design parameters, in The 39th International Technical Conference on Clean Coal & Fuel Systems 2014: Clearwater, FL.
- [101] Yi, F., Gopan, A. and Axelbaum, R. L., Characterization of coal water slurry prepared for PRB coal. *Journal of Fuel Chemistry and Technology*. 2014. 42(10).
- [102] Efficient Use of Coal Water Fuels Technology Assessment Report 74. 2008. CSIRO Energy Technology.
- [103] Wang, R. K., et al., The Slurrying Properties of Coal Water Slurries Containing Raw Sewage Sludge. *Energy & Fuels*. 2011. 25: p. 747-752.
- [104] Laskowski, J. S., Chapter 3 Coal surface properties, in *Developments in Mineral Processing*. 2001. Elsevier. p. 31-94.
- [105] Toftegaard, M. B., et al., Oxy-fuel combustion of solid fuels. *Progress in Energy and Combustion Science*. 2010. 36(5): p. 581-625.

- [106] Nikzat, H., et al., Characteristics of Pulverized Coal Burner Using a High-Oxygen Partial Pressure. *Chemical Engineering Research and Design*. 2004. 82(1): p. 99-104.
- [107] Xia, F., et al., Staged, pressurized oxy-combustion: computational fluid dynamics simulations of a novel burner design, in Eastern States Section of the Combustion Institute 2013: Clemson, SC.
- [108] Yang, Z., Gopan, A. and Axelbaum, R. L. Predicting ash deposition from non-isothermal, turbulent parallel flows. in 10th US National Combustion Meeting. 2017. College Park, Maryland.
- [109] Mullinger, P. and Jenkins, B., *Industrial and process furnaces : principles, design and operation*. Butterworth-Heinemann/ICHEME series. 2008. Amsterdam: Elsevier/Butterworth-Heinemann. 524.
- [110] Xia, F., et al., Control of radiative heat transfer in high-temperature environments via radiative trapping—Part I: Theoretical analysis applied to pressurized oxy-combustion. *Fuel*. 2016. 172: p. 81-88.
- [111] Xia, F., et al., Trapping B. In prep.
- [112] Siegel, R. and Howell, J. R., *Thermal radiation heat transfer*. 3rd ed. 2001: Hemisphere Publishing Corporation.
- [113] Friedlander, S. K., *Smoke, Dust, and Haze: Fundamentals of Aerosol Dynamics*. Topics in Chemical Engineering, 2000. Oxford University Press, New York.
- [114] Yang, Z., et al., Dynamic model for an oxygen-staged slagging entrained flow gasifier. *Energy & Fuels*. 2011. 25(8): p. 3646-3656.
- [115] Yang, Z., et al., Use of a reactor network model in the design and operation of a new type of membrane wall entrained flow gasifier. *Energy & Fuels*. 2013. 27(10): p. 6322-6332.
- [116] Study of the off-design performance of integrated coal gasification combined-cycle power plants. 1986. Stanford Univ., CA (USA).
- [117] Damage to power plant due to cyclic operation and guidelines for best practices. ETD report # 1096-gsp-81. 2009. European Technology Development Ltd.
- [118] Hentschel, J., Babić, U. A. and Spliethoff, H., A parametric approach for the valuation of power plant flexibility options. *Energy Reports*. 2016. 2: p. 40-47.
- [119] Arias, B., An analysis of the operation of a flexible oxy-fired CFB power plant integrated with a thermal energy storage system. *International Journal of Greenhouse Gas Control*. 2016. 45: p. 172-180.

- [120] Chalmers, H., et al., Valuing flexible operation of power plants with CO₂ capture. *Energy Procedia*. 2009. 1(1): p. 4289-4296.
- [121] Cohen, S. M., Rochelle, G. T. and Webber, M. E., Optimal operation of flexible post-combustion CO₂ capture in response to volatile electricity prices. *Energy Procedia*. 2011. 4: p. 2604-2611.
- [122] Lucquiaud, M., et al., Enhanced Operating Flexibility and Optimised Off-design Operation of Coal Plants with Post-combustion Capture. *Energy Procedia*. 2014. 63: p. 7494-7507.
- [123] Al-Abbas, A. H., Naser, J. and Hussein, E. K., Numerical simulation of brown coal combustion in a 550 MW tangentially-fired furnace under different operating conditions. *Fuel*. 2013. 107: p. 688-698.
- [124] Cao, Q., et al., Numerical Study of Furnace Process of a 600 MW Pulverized Coal Boiler Under Low Load with SNCR Application, in *Cleaner Combustion and Sustainable World*. 2013. Springer. p. 137-142.
- [125] Gopan, A., et al. Effect of stoichiometric ratio and oxygen concentration on heat flux profiles in oxy-coal combustion. in *9th U.S. National Combustion Meeting*. 2015. Cincinnati, Ohio.
- [126] Baumgartner, A., et al. Impact of direct oxygen injection on flame stability and overall burnout during oxyfuel combustion. in *18th IFRF Members' Conference: Flexible and clean fuel conversion in industry*. 2015. Freising, Germany.
- [127] Menter, F. R., Two-equation eddy-viscosity turbulence models for engineering applications. *AIAA Journal*. 1994. 32(8): p. 1598-1605.
- [128] Fluent, A., 12.0 Theory Guide. Ansys Inc. 2009. 5.
- [129] Fletcher, T. H., et al., Chemical percolation model for devolatilization. 2. Temperature and heating rate effects on product yields. *Energy & Fuels*. 1990. 4(1): p. 54-60.
- [130] Chui, E. and Raithby, G., Computation of radiant heat transfer on a nonorthogonal mesh using the finite-volume method. *Numerical Heat Transfer*. 1993. 23(3): p. 269-288.
- [131] Raithby, G. and Chui, E., A finite-volume method for predicting a radiant heat transfer in enclosures with participating media. *ASME, Transactions, Journal of Heat Transfer*. 1990. 112: p. 415-423.
- [132] Shen, Z. and Friedman, J., Evaluation of Coefficients for the Weighted Sum of Gray Gases Model. 1982.

- [133] Yin, C., On gas and particle radiation in pulverized fuel combustion furnaces. *Applied Energy*. 2015.
- [134] Backreedy, R., et al., Modelling pulverised coal combustion using a detailed coal combustion model. *Combustion Science and Technology*. 2006. 178(4): p. 763-787.
- [135] Wall, T., et al., The properties and thermal effects of ash deposits in coal-fired furnaces. *Progress in Energy and Combustion Science*. 1993. 19(6): p. 487-504.
- [136] Basu, P., Kefa, C. and Jestin, L., *Boilers and burners: design and theory*. 2012: Springer Science & Business Media.
- [137] Pickard, A. and Meinecke, G., The future role of fossil power generation.
- [138] Finley, R. A Base Load Free Power System. 2012 [cited 2017 07-06-2017]; Available from: <http://www.energytrendsinsider.com/2012/04/05/a-base-load-free-power-system/>.
- [139] Zebian, H. and Mitsos, A., Pressurized OCC (oxy-coal combustion) process ideally flexible to the thermal load. *Energy*. 2014. 73: p. 416-429.
- [140] Viswanathan, V., Purgert, R. and Rawls, P., Coal-fired power materials. *Adv. Mater. Processes*. 2008. 166(8): p. 47-49.
- [141] Skeen, S. A., Yablonsky, G. and Axelbaum, R. L., Characteristics of non-premixed oxygen-enhanced combustion: II. Flame structure effects on soot precursor kinetics resulting in soot-free flames. *Combustion and Flame*. 2010. 157(9): p. 1745-1752.
- [142] Skeen, S. A., Yablonsky, G. and Axelbaum, R. L., Characteristics of non-premixed oxygen-enhanced combustion: I. The presence of appreciable oxygen at the location of maximum temperature. *Combustion and Flame*. 2009. 156(11): p. 2145-2152.
- [143] Kumfer, B. M., Skeen, S. A. and Axelbaum, R. L., Soot inception limits in laminar diffusion flames with application to oxy-fuel combustion. *Combustion and Flame*. 2008. 154(3): p. 546-556.
- [144] Chao, B. H., Liu, S. and Axelbaum, R. L., On soot inception in nonpremixed flames and the effects of flame structure. *Combustion Science and Technology*. 1998. 138(1-6): p. 105-135.
- [145] Sunderland, P. B., et al., Sooting limits of microgravity spherical diffusion flames in oxygen-enhanced air and diluted fuel. *Combustion Science and Technology*. 2004. 176(12): p. 2143-2164.
- [146] Sunderland, P. B., et al., Effects of structure and hydrodynamics on the sooting behavior of spherical microgravity diffusion flames. *Combustion and Flame*. 2003. 132(1-2): p. 25-33.

- [147] Lin, K. C. and Faeth, G. M., Hydrodynamic suppression of soot emissions in laminar diffusion flames. *Journal of Propulsion and Power*. 1996. 12(1): p. 10-17.
- [148] Sugiyama, G., Twenty-Fifth Symposium (International) on Combustion Nonluminous diffusion flame of diluted acetylene in oxygen-enriched air. *Symposium (International) on Combustion*. 1994. 25(1): p. 601-608.
- [149] Glassman, I., Sooting laminar diffusion flames: Effect of dilution, additives, pressure, and microgravity. *Symposium (International) on Combustion*. 1998. 27(1): p. 1589-1596.
- [150] Law, C. K., *Combustion physics*. 2010: Cambridge university press.
- [151] Calcote, H. F., Olson, D. B. and Keil, D. G., Are ions important in soot formation? *Energy & Fuels*. 1988. 2(4): p. 494-504.
- [152] Kumfer, B. M., et al., Measurement and analysis of soot inception limits of oxygen-enriched coflow flames. *Combustion and Flame*. 2006. 147(3): p. 233-242.
- [153] Burke, S. and Schumann, T., *Diffusion flames*. *Industrial & Engineering Chemistry*. 1928. 20(10): p. 998-1004.
- [154] Chung, S. H. and Law, C. K., Burke–Schumann Flame with Streamwise and Preferential Diffusion. *Combustion Science and Technology*. 1984. 37(1-2): p. 21-46.
- [155] Ko, Y.-C., Hou, S.-S. and Lin, T.-H., Laminar diffusion flames in a multiport burner. *Combustion Science and Technology*. 2005. 177(8): p. 1463-1484.
- [156] Kumfer, B. M., Design of diffusion flame structure for reduced soot using oxygen-enriched combustion. 2006.
- [157] Gopan, A., et al., Effect of stoichiometric ratio and oxygen concentration on heat flux profiles in oxy-coal combustion, in 9th U.S. National Combustion Meeting 2015: Cincinnati, Ohio.
- [158] Edge, P., et al., Combustion modelling opportunities and challenges for oxy-coal carbon capture technology. *Chemical Engineering Research and Design*. 2011. 89(9): p. 1470-1493.
- [159] Smoot, L. D., Modeling of coal-combustion processes. *Progress in Energy and Combustion Science*. 1984. 10(2): p. 229-267.
- [160] Yin, C., et al., Use of numerical modeling in design for co-firing biomass in wall-fired burners. *Chemical engineering science*. 2004. 59(16): p. 3281-3292.
- [161] Eastwick, C., Pickering, S. and Aroussi, A., Comparisons of two commercial computational fluid dynamics codes in modelling pulverised coal combustion for a 2.5 MW burner. *Applied Mathematical Modelling*. 1999. 23(6): p. 437-446.

- [162] Vuthaluru, R. and Vuthaluru, H., Modelling of a wall fired furnace for different operating conditions using FLUENT. *Fuel Processing Technology*. 2006. 87(7): p. 633-639.
- [163] Ghenai, C. and Janajreh, I., CFD analysis of the effects of co-firing biomass with coal. *Energy conversion and management*. 2010. 51(8): p. 1694-1701.
- [164] Backreedy, R., et al., Co-firing pulverised coal and biomass: a modeling approach. *Proceedings of the Combustion Institute*. 2005. 30(2): p. 2955-2964.
- [165] Tian, Z., et al., Comparison of two-equation turbulence models in simulation of a non-swirl coal flame in a pilot-scale furnace. *Combustion Science and Technology*. 2009. 181(7): p. 954-983.
- [166] Tian, Z., et al., Modeling issues in CFD simulation of brown coal combustion in a utility furnace. *The Journal of Computational Multiphase Flows*. 2010. 2(2): p. 73-88.
- [167] Kangwanpongpan, T., Da Silva, R. C. and Krautz, H. J., Prediction of oxy-coal combustion through an optimized weighted sum of gray gases model. *Energy*. 2012. 41(1): p. 244-251.
- [168] Yin, C., Rosendahl, L. A. and Kær, S. K., Chemistry and radiation in oxy-fuel combustion: a computational fluid dynamics modeling study. *Fuel*. 2011. 90(7): p. 2519-2529.
- [169] Chen, L., Gazzino, M. and Ghoniem, A. F. Characteristics of pressurized oxy-coal combustion under increasing swirl number. in *Proceedings of the 35th international technical conference on clean coal & fuel systems*. 2010.
- [170] Andersen, J., et al., Global Combustion Mechanisms for Use in CFD Modeling under Oxy-Fuel Conditions. *Energy & Fuels*. 2009. 23(3): p. 1379-1389.
- [171] Genetti, D., Fletcher, T. H. and Pugmire, R. J., Development and application of a correlation of ¹³C NMR chemical structural analyses of coal based on elemental composition and volatile matter content. *Energy & Fuels*. 1999. 13(1): p. 60-68.
- [172] Chui, E. H. and Raithby, G. D., computation of radiant heat transfer on a nonorthogonal mesh using the finite-volume method. *Numerical Heat Transfer, Part B: Fundamentals*. 1993. 23(3): p. 269-288.
- [173] Raithby, G. D. and Chui, E. H., A Finite-Volume Method for Predicting a Radiant Heat Transfer in Enclosures With Participating Media. *Journal of Heat Transfer*. 1990. 112(2): p. 415-423.
- [174] Modest, M. F., The weighted-sum-of-gray-gases model for arbitrary solution methods in radiative transfer. *Journal of Heat Transfer*. 1991. 113(3): p. 650-656.

- [175] Anderson, R., et al., Oxy-Fuel Turbo Machinery Development for Energy Intensive Industrial Applications. *Energy Procedia*. 2014. 63: p. 511.
- [176] Climent Barba, F., et al., A technical evaluation, performance analysis and risk assessment of multiple novel oxy-turbine power cycles with complete CO₂ capture. *J. Cleaner Prod.* 2016. 133: p. 971.
- [177] Ditaranto, M. and Oppelt, T., Radiative heat flux characteristics of methane flames in oxy-fuel atmospheres. *Exp. Therm. Fluid Sci.* 2011. 35(7): p. 1343.
- [178] Kez, V., et al., A comprehensive evaluation of different radiation models in a gas turbine combustor under conditions of oxy-fuel combustion with dry recycle. *J. Quant. Spectrosc. Radiat. Transfer*. 2016. 172: p. 121.
- [179] Habib, M. A., Nemitallah, M. and Ben-Mansour, R., Recent Development in Oxy-Combustion Technology and Its Applications to Gas Turbine Combustors and ITM Reactors. *Energy Fuels*. 2013. 27(1): p. 2.
- [180] Saanum, I. and Ditaranto, M., Experimental Study of Oxy-fuel Combustion under Gas Turbine Conditions. *Energy & Fuels*. 2017.
- [181] Bi, X., Qiao, X. and Lee, C.-F. F., Investigation about Temperature Effects on Soot Mechanisms Using a Phenomenological Soot Model of Real Biodiesel. *Energy & Fuels*. 2013. 27(9): p. 5320-5331.
- [182] Hjærtstam, S., et al., Computational Fluid Dynamics Modeling of Oxy-Fuel Flames: The Role of Soot and Gas Radiation. *Energy & Fuels*. 2012. 26(5): p. 2786-2797.
- [183] Andersson, K., et al., Radiation Intensity of Propane-Fired Oxy-Fuel Flames: Implications for Soot Formation. *Energy & Fuels*. 2008. 22(3): p. 1535-1541.
- [184] De Joannon, M., et al., Mild Combustion: Process Features and Technological Constrains. *Combustion Science and Technology*. 2000. 153(1): p. 33-50.
- [185] Effuggi, A., et al., Mild Combustion of Methane-Derived Fuel Mixtures: Natural Gas and Biogas. *Combustion Science and Technology*. 2008. 180(3): p. 481-493.
- [186] Khalil, A. E. E. and Gupta, A. K., The role of CO₂ on oxy-colorless distributed combustion. *Applied Energy*. 2017. 188: p. 466-474.
- [187] Du, J. and Axelbaum, R. L., The effect of flame structure on soot-particle inception in diffusion flames. *Combustion and Flame*. 1995. 100(3): p. 367-375.

- [188] Chen, R. and Axelbaum, R. L., Scalar dissipation rate at extinction and the effects of oxygen-enriched combustion. *Combustion and Flame*. 2005. 142(1–2): p. 62-71.
- [189] Leusden, C. P. and Peters, N., Experimental and numerical analysis of the influence of oxygen on soot formation in laminar counterflow flames of acetylene. *Proceedings of the Combustion Institute*. 2000. 28(2): p. 2619-2625.
- [190] Donbar, J. M., Driscoll, J. F. and Carter, C. D., Strain rates measured along the wrinkled flame contour within turbulent non-premixed jet flames. *Combustion and Flame*. 2001. 125(4): p. 1239-1257.
- [191] Figura, L. and Gomez, A., Structure of incipiently sooting ethylene–nitrogen counterflow diffusion flames at high pressures. *Combustion and Flame*. 2014. 161(6): p. 1587-1603.
- [192] Kent, J. H. and Honnery, D., Soot and Mixture Fraction in Turbulent Diffusion Flames. *Combustion Science and Technology*. 1987. 54(1-6): p. 383-398.
- [193] Attili, A., et al., Formation, growth, and transport of soot in a three-dimensional turbulent non-premixed jet flame. *Combustion and Flame*. 2014. 161(7): p. 1849-1865.
- [194] Bisetti, F., et al., On the formation and early evolution of soot in turbulent nonpremixed flames. *Combustion and Flame*. 2012. 159(1): p. 317-335.
- [195] Mueller, M. E., et al., Experimental and computational study of soot evolution in a turbulent nonpremixed bluff body ethylene flame. *Combustion and Flame*. 2013. 160(7): p. 1298-1309.
- [196] Mueller, M. E. and Pitsch, H., LES model for sooting turbulent nonpremixed flames. *Combustion and Flame*. 2012. 159(6): p. 2166-2180.
- [197] Mueller, M. E. and Raman, V., Effects of turbulent combustion modeling errors on soot evolution in a turbulent nonpremixed jet flame. *Combustion and Flame*. 2014. 161(7): p. 1842-1848.
- [198] Du, D. X., Axelbaum, R. L. and Law, C. K., The influence of carbon dioxide and oxygen as additives on soot formation in diffusion flames. *Symposium (International) on Combustion*. 1991. 23(1): p. 1501-1507.
- [199] Alexander Schumaker, S. and Driscoll, J. F., Mixing properties of coaxial jets with large velocity ratios and large inverse density ratios. *Physics of Fluids*. 2012. 24(5): p. 055101.
- [200] Villiermaux, E. and Rehab, H., Mixing in coaxial jets. *Journal of Fluid Mechanics*. 2000. 425: p. 161-185.

- [201] Markstein, G. H., Scaling of radiative characteristics of turbulent diffusion flames. Symposium (International) on Combustion. 1977. 16(1): p. 1407-1419.
- [202] Du, D. X., Axelbaum, R. L. and Law, C. K., Experiments on the sooting limits of aerodynamically-strained diffusion flames. Symposium (International) on Combustion. 1989. 22(1): p. 387-394.
- [203] Modest, M. F., Radiative heat transfer. 2013: Academic press.
- [204] Davis, S. G., Law, C. K. and Wang, H., Propene pyrolysis and oxidation kinetics in a flow reactor and laminar flames. Combustion and Flame. 1999. 119(4): p. 375-399.
- [205] Nussbaumer, T., Combustion and Co-combustion of Biomass: Fundamentals, Technologies, and Primary Measures for Emission Reduction. Energy Fuels. 2003. 17(6): p. 1510-1521.
- [206] Annamalai, Co-firing of coal and feedlot biomass (FB) in a laboratory scale boiler burner. Proceedings - Annual International Pittsburgh Coal Conference. 2000. 17th: p. 1200.
- [207] Hunt, E. F. F., The shawville coal/biomass cofiring test: A coal/power industry cooperative test of direct fossil-fuel CO₂ mitigation. Energy conversion and management. 1997. 38(suppl., proceedings of the third international conference on carbon dioxide removal, 1996): p. S551-S556.
- [208] Mun, T.-Y., Lee, J. W. and Yang, W., Approaches to biomass co-firing in a pulverized coal boiler. Int. Tech. Conf. Clean Coal Fuel Syst. 2014. 39: p. 465-472.
- [209] Mahr, D. Biomass Attributes, Handling, and Processing Issues for Large Power Plants. in ASME 2010 Power Conference. 2012. Chicago, IL, USA.
- [210] Giuliano Grassi, A. S., Marco Maltagliati, Sefano Capacciolo, Large Scale Supply and International Trading of Refined Biomass. European Biomass Conference and Exhibition. 2012. 20(B): p. 2373-2375.
- [211] Mann, M. K., The environmental benefits of cofiring biomass and coal. Proceedings of the International Technical Conference on Coal Utilization&Fuel Systems. 2002. 27th(vol. 1): p. 205.
- [212] Robinson, A. L., Junker, H. and Baxter, L. L., Pilot-Scale Investigation of the Influence of Coal-Biomass Cofiring on Ash Deposition. Energy & Fuels. 2002. 16(2): p. 343-355.
- [213] Roper, F. G., Smith, C. and Cunningham, A. C., The prediction of laminar jet diffusion flame sizes: Part II. Experimental verification. Combustion and Flame. 1977. 29(0): p. 227-234.

- [214] Essenhigh, R. H., Foertsch, D. and Klimesh, H. E., Combustion Characteristics of Carbon: Influence of the Zone I-Zone II Transition on Burn-Out in Pulverized Coal Flames. *Energy Fuels*. 1999. 13(5): p. 955-960.
- [215] Holtmeyer, M. L. L., Effects of biomass particle size during cofiring under air-fired and oxyfuel conditions. *Applied Energy*. 2012. 93: p. 606-613.
- [216] Holtmeyer, M. L., et al., The Impact of Biomass Cofiring on Volatile Flame Length. *Energy & Fuels*. 2013. 27(12): p. 7762-7771.
- [217] Robinson, A. L., Rhodes, J. S. and Keith, D. W., Assessment of Potential Carbon Dioxide Reductions Due to Biomass–Coal Cofiring in the United States. *Environmental Science & Technology*. 2003. 37(22): p. 5081-5089.
- [218] Loeffler, D. and Anderson, N., Emissions tradeoffs associated with cofiring forest biomass with coal: A case study in Colorado, USA. *Applied energy*. 2014. 113(0): p. 67-77.
- [219] Holtmeyer, M. L., Characteristics of biomass fuels and their impact on volatile flame length during biomass cofiring combustion. *International Technical Conference on Clean Coal and Fuel Systems*. 2012. 37: p. 206.
- [220] Darold E. Ward, W. M. H., Projections of Emissions from Burning of Biomass for Use in Studies of Global Climate and Atmospheric Chemistry, in *The 84th Annual Meeting and Exhibition of the Air & Waste Management Association* 1991: Vancouver, British Columbia. p. 91-128.
- [221] Annamalai, K., Ryan, W. and Dhanapalan, S., Interactive processes in gasification and combustion - Part III: Coal / char particle arrays, streams and clouds. *Progress in Energy and Combustion Science*. 1994. 20: p. 487-618.
- [222] Ryan, W. and Annamalai, K., Group ignition of a cloud of coal particles. *Journal of Heat Transfer*. 1991. 113.
- [223] Christopher D. Risbrudt, M. a. R., Theodore H. Wagner, *Wood Handbook: Wood as an Engineering Material Wood Handbook*, ed. Ross, R. J. 2010. Madison, Wisconsin Forest Product Laboratory. 508.
- [224] Clark, A. Estimating Moisture Content Of Tree-Length Roundwood. in *Pulping/Process and Product Quality Conference*. 2000.
- [225] Eckelman, C. A., The Shrinking and Swelling of Wood and Its Effect on Furniture. *Forest and Natural Resources*. 1998. 163: p. 26.

Appendix A

Computational Fluid Dynamics (CFD)

Sub-Model Selection Criteria

ANSYS FLUENT version 13.0 was used to simulate the different burner designs and operating conditions. The flow field was modeled using the Reynolds-Averaged Navier-Stokes (RANS) equations with the Semi-Implicit Method for Pressure Linked Equations (SIMPLE) algorithm to address pressure-velocity coupling. RANS has been used extensively to study flame behavior for pulverized fuels [158-160] and the sub-models have been extensively validated for the atmospheric-pressure oxy-coal combustion environment [33, 161-166]. While it has been shown that RANS simulations provide reasonable agreement with experiments under atmospheric pressure oxy-combustion conditions, to date, the solid-fuel combustion submodels have not been validated for pressurized oxy-combustion.

The shear stress transport (SST) $k-\omega$ model was used in this simulation, which has been shown to be the combination of the best aspects of the two standard models, $k-\epsilon$ and $k-\omega$ [127]. The finite rate/eddy dissipation model, which has been extensively utilized for oxy-combustion [167-169], was used for turbulence-chemistry interactions. A two-step global reaction mechanism was used

to capture the gaseous volatile reaction. The first step was volatile oxidation to carbon monoxide, and the second step was oxidation of carbon monoxide to carbon dioxide. More detailed reaction mechanisms [170], together with a more advanced reaction model, i.e. eddy dissipation concept (EDC) model have been tested. The EDC model takes into account CO_2 and H_2O dissociation and thus gives a lower flame temperature, and slightly lower peak wall heat flux than the finite rate/eddy dissipation model. Thus, in this work, the more conservative results with respect to peak wall heat flux, obtained from the finite rate/eddy dissipation model, are presented.

Particle trajectories were computed in the Lagrangian frame and were coupled to the gas phase. All discrete particles were assumed to be spherical. The pulverized coal particle size was assumed to follow the Rosin-Rammler distribution, with an average diameter of $65 \mu\text{m}$. The minimum and maximum particle sizes were $10 \mu\text{m}$ and $200 \mu\text{m}$, respectively, and the spread parameter of the distribution was 3.5. The effect of turbulence on the particle trajectories was accounted for with the Discrete Random Walk (DRW) model. The devolatilization rate of the coal particles was calculated using the Chemical Percolation Devolatilization (CPD) model [129]. NMR chemical structure parameters were calculated according to the correlations in [171]. The char surface oxidation rate with molecular oxygen was modeled by a kinetics/diffusion-limited model.

The Discrete Ordinates (DO) [172, 173] radiation model was used to solve the radiative transfer equation (RTE). Each octant of the entire 4π angular space was discretized at each spatial location into 5×5 solid angles (i.e. control angles), leading to a total of 200 directions. Further refined discretization did not show any noticeable improvement in terms of the distributions of temperature and incident radiation. Gaseous emission and absorption were considered using the domain-based Weighted Sum of Gray Gases model (WSGGM) [174]. The emissivity of coal particles is approximately 1, while that of fly ash is 0.6 [133]. Based on a sensitivity analysis, it

was found that, counterintuitively, a lower emissivity leads to a higher wall heat flux due to radiative trapping. Thus, a conservative value of 0.6 was chosen for the emissivity of all particles so that the results reported indicate the maximum incident wall heat flux. The particle scattering factor was set to be 0.6, which is widely used in modeling studies for pulverized fuel combustion [134].

The surface temperature of the boiler wall was assumed to be 700 K. This is a reasonable, yet slightly conservative assumption because the boiler feed water entering the combustor is at a temperature of about 564 K. A higher wall temperature would lead to a lower wall heat flux and a lower temperature would lead to a higher wall heat flux. A sensitivity analysis of wall temperature was conducted and showed that a variation from 100 K to 1000 K produced only about an 8% difference in wall heat flux. For wall emissivity, it was assumed that during operation the walls would accumulate a small amount of ash. Depending on the properties of the ash, and whether the deposit is loose, sintered or fused, values between 0.37 to 0.93 have been reported in the literature [135]. In the current study, a relatively conservative value of 0.8 was chosen for the emissivity of the wall. A high emissivity implies a less reflective wall, and hence a higher net heat flux to the wall.

A 2-D axisymmetric model was built based on the burner and boiler geometry, taking advantage of the axisymmetric nature of the boiler. Simulation results for cases with 30,000, 150,000, 230,000 and 350,000 cells were compared. Negligible differences in velocity, temperature and heat transfer were observed for the last two cases. Moreover, a 3-D model with 10 million cells was constructed, and the difference between the results of the 3-D model and those of the 2-D model with 230,000 cells was negligible. Thus, only results for the 2-D model with 230,000 cells are reported.

Appendix B

Effects of inert-placement (Z_{st}) on soot and radiative heat flux in turbulent diffusion flames

*Akshay Gopan, Zhiwei Yang, Benjamin M. Kumfer, Richard L. Axelbaum**

AUTHOR ADDRESS:

Department of Energy, Environmental & Chemical Engineering, Washington University in St.
Louis, St. Louis, Missouri-63130, USA

* *Corresponding author. Tel: +1 314-935-7560; Fax: +1 314-935-5464.*

Email: axelbaum@wustl.edu (Prof. Richard L. Axelbaum)

Published in Energy & Fuels (2017). DOI: 10.1021/acs.energyfuels.7b01092

ABSTRACT

Oxy-fuel combustion is one of the major strategies for reducing carbon dioxide emissions from combustion sources, as well as in applications requiring high temperature and stable flames. Currently in oxy-combustion, a large amount of flue gas (~ 70%) is recycled to control the heat flux by reducing the flame temperature. This reduces the efficiency of the process, and is unsuitable for processes requiring high temperature gases at the outlet of the combustor, such as gas turbines. Controlling the soot formation and growth at high temperatures could offer another means of controlling the heat flux without reducing the temperature. The separation of the inert from oxygen, in oxy-combustion, offers a unique advantage for burner design. Shifting the inert from the oxidizer to the fuel side in appropriate stoichiometric proportions increases the stoichiometric mixture fraction (Z_{st}) while maintaining the same adiabatic flame temperature. In this work, the impact of Z_{st} on the characteristics of a non-premixed, turbulent-jet flame was studied. With increasing Z_{st} , soot inception is delayed, and the overall soot volume fraction and radiative heat flux are also drastically reduced. This is a consequence of not just the reduction in fuel concentration, but also the change in the flame structure, which has a dramatic effect on the kinetics of soot formation. This method could provide an effective means of reducing the flue gas recycle in oxy-combustion, without resulting in drastically high heat flux.

KEYWORDS

Turbulent flames; Oxy-fuel combustion; Soot; Heat Flux.

B.1 Introduction

Oxy-fuel combustion is one of three major strategies to capture carbon dioxide from power plants and other industrial furnaces [175, 176]. The most common oxy-fuel concept that is employed for carbon capture and storage (CCS) is to combust the fuel in a stream of oxygen that is diluted with a large amount of recycled flue gas (~ 70%) [39]. The purpose of flue gas recycling is to ensure that the flame temperature and heat flux are similar to those of air-fired combustion, where the oxygen is naturally diluted with nitrogen [177, 178]. This allows either the retrofit of existing air-fired boilers or the use of similar construction materials for the walls, or the boiler tubes in the case of power plants. A number of new developments have occurred in terms of burner design due to the increased understanding of the effect of oxy-fuel combustion on the combustion characteristics in various combustors, especially gas turbines [177-180].

In recent years, there has been interest in reducing the amount of flue gas recycle in order to increase the process efficiency [45, 46, 56, 57]. Reducing the amount of inert (recycled flue gas) leads to increased flame temperature, which can increase the amount of soot [181, 182]. The increase in soot and the higher flame temperatures lead to higher radiative heat flux emitted from the flame [177, 183]. If the heat flux at the wall is too high, expensive alloys may be required in power plants, while industrial process could face challenges in terms of product degradation. Some methods, such as moderate or intense low-oxygen dilution (MILD) combustion can reduce soot in combustion systems [184, 185]. However, achieving MILD conditions will be challenging in reduced flue gas recycle [186]. Thus, a means to control heat flux from high temperature flames is required if flue gas recycle is to be reduced.

In oxy-combustion, the separation of the inert from oxygen offers a unique advantage for burner design, with independent control of the amount of inert and a choice in terms of placement in the oxidizer and fuel streams. In lab-scale laminar flames, the effect of the relative placement of inert between the oxidizer and fuel streams has shown to significantly affect soot inception [141-149]. Varying the amount of inert placed in the fuel and oxidizer streams can change both the temperature of the flame as well as the stoichiometric mixture fraction (Z_{st}) of the flame, where Z_{st} is defined as

$$Z_{st} = \left(1 + \frac{\nu_{O_2} W_{O_2} Y_{F,f}}{\nu_F W_F Y_{O_2,o}} \right)^{-1} \quad (\text{B-1})$$

where Y_i , ν_i , and W_i , respectively indicate the mass fraction, stoichiometric coefficient, and molecular weight of species i , and the subscripts f and o represent the fuel and oxidizer inlet streams. The mixture fraction at any point can be conceptually understood as the fraction of the material at that point that originated in the fuel stream, and the stoichiometric mixture fraction is the mixture fraction at the location of stoichiometry, *i.e.*, at the flame [150]. A typical fuel-air flame has a low Z_{st} (≈ 0.06 for propane). Increasing the oxygen concentration in the oxidizer and/or decreasing the fuel concentration in the fuel stream increases Z_{st} .

Non-premixed laminar flames are quite sensitive to the stoichiometric mixture fraction, with an increase in Z_{st} reducing or even eliminating soot formation for traditionally sooty fuels, with some studies identifying permanently blue flames (soot-free flames at near-zero strain rates) even at high temperatures [187]. Several explanations for this dramatic inhibition of soot have been proposed, including fuel-dilution and varying thermal diffusivities [149], fluid dynamic effects [147], and changes in flame structure [187]. Changes in flame structure refer to alterations of the species and

temperature profiles in the high-temperature reaction zone. Higher Z_{st} leads to higher oxygen concentrations in the high temperature region, which changes the chemistry for soot inception [141]. Through a series of studies it was found that for laminar flames the most significant impact on soot inception was from the change in flame structure, and this is the reason that permanently blue flames can be observed [141-144, 152, 187, 188]. Using spherical flames in microgravity, Sunderland et al. [145, 146], were able to isolate the effects of hydrodynamics and flame structure, and confirmed that flame structure variations played a predominant role in affecting the soot concentrations at high Z_{st} . In laminar co-flow systems, criteria for soot inception and predictive models for soot inception limits have been developed [143, 152]. Furthermore, it has been shown that at high Z_{st} , flame strength significantly increases [188].

Despite significant literature on soot inception limits of laminar diffusion flames for various Z_{st} [141-146, 149, 152, 187-189], and the utilization of Z_{st} to increase or decrease soot in flames [190, 191], to our knowledge there have been no systematic studies on the impact of Z_{st} on turbulent flames. The characteristic times, mixing rates and soot particle history experienced in turbulent flames are quite different from those of laminar flames, and thus the impact of Z_{st} on soot formation could be quite different [192]. The soot formation and growth mechanisms in turbulent flames have also been shown to be dependent on the combustion system. In other words, different mechanisms could dominate in different types of turbulent flames. For example, Pitsch and co-workers [193-197] studied co-axial turbulent jet flames and bluff-body stabilized flames using experiments and numerical simulations, including direct numerical simulation (DNS) and large-eddy simulation (LES), and showed that for turbulent jet flames, soot formation and growth is primarily dependent on PAH formation and condensation on existing soot, whereas for a bluff-body-stabilized flames, PAH growth is dependent on the acetylene-based hydrogen-abstraction

carbon-addition (HACA) mechanism near the bluff body, and PAH condensation at larger distances.

Since most industrial processes and power plants are turbulent, there is a need to understand the effects of inert placement, and hence Z_{st} , on soot formation in turbulent flames. In addition, oxy-combustion, wherein oxygen is available as the oxidizer, can intrinsically be operated under a wide range of Z_{st} , and thus the effect of Z_{st} on the heat-flux profiles needs to be studied under these conditions as well. In this work, we study the impact of inert placement (Z_{st}) on the soot and radiative heat flux of a turbulent, high temperature propane flame, by isolating the impact of inert placement from all other affecting parameters, such as temperature, velocity and mixing.

B.2 Experimental Methods

B.2.1 Reactor

All experiments were performed in a 2.44 m long, vertical, down-fired combustor (Figure 1). The shape of the first 0.86 m of the combustor is that of a frustum of a cone, with top and bottom diameters of 0.06 m and 0.14 m respectively. Downstream from this, the combustor is a cylinder 0.14 m in diameter and 1.58 m long. The exhaust gas from the combustor passes through a filter bag and is vented to the outside. The fuel, along with the inert (if any), is injected through a 0.013 m diameter central tube. The oxidizer is fed through a co-axial annulus with inner and outer diameters of 0.019 m and 0.06 m respectively. Both the fuel and the oxidizer are axially fed using flow straighteners. A small stabilization ring of dimensions 0.003 m (streamwise) and 0.004 m (normal) was installed in the inner diameter of the secondary annulus to ensure flame attachment. The burner was sized to give sufficiently high velocity to minimize the effect of buoyancy at the

inlet, and the conical shape was designed to minimize the effect of buoyancy even downstream by keeping the Richardson number low everywhere along the flame region, as described in Xia et al. [98] and demonstrated in Gopan et al. [157]. Briefly, the small initial reactor diameter ensures high velocity, and as the gases heat up and are generated during combustion, the diameter of the conical section is increased to accommodate the increased flow rate. Along the axis, the combustor has 16 ports of 0.04 m diameter, located at every 0.15 m, starting 0.05 m downstream of the burner exit. When not being used for measurements, each port is plugged using the same refractory material as the combustor wall.

Each experiment was initiated with cold-wall (room-temperature) conditions and was completed within 20 mins to ensure the wall temperature was low and wall radiative emission minimal. This was further confirmed at the end of the experiment by noting the location of the maximum heat flux, switching the flame off, and measuring the heat flux at the noted location with no flame.

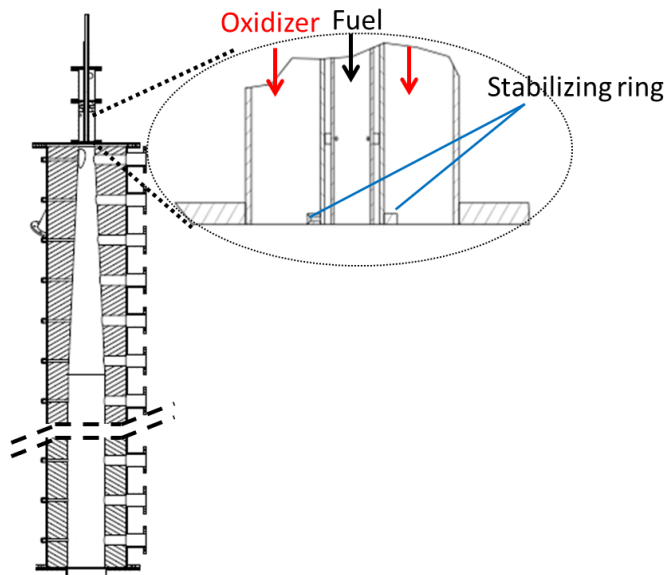
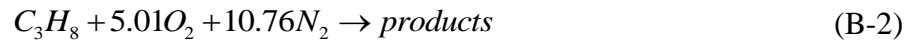


Figure B-1. Combustor and burner design.

B.2.2 Experimental Conditions

The input flow rates of the fuel, oxidizer, and inert for each of the cases are given in Table 1. Both the oxidizer and the fuel for all cases were turbulent, with the fuel and oxidizer Reynolds numbers greater than 7200 and 6200, respectively, for all cases. The stoichiometric adiabatic flame temperature (T_{ad}), calculated using an equilibrium based calculator [187], was 2595 K. In the limit of infinite Damkohler number, in an equi-diffusional system (*i.e.*, unity Lewis number), the stoichiometry uniquely defines the adiabatic flame temperature. For the propane flames studied in this work, the stoichiometry is given by



with the fraction of the N_2 supplied with the fuel and oxidizer changing to change the Z_{st} without changing the flame temperature. The inert used in this experiment was nitrogen and not CO_2 , in order to avoid complications of the different heat capacity and chemical effects of CO_2 in soot gasification [198]. The Z_{st} was varied between 0.38 and 0.68. In all cases the overall stoichiometric ratio was kept sufficiently high (> 3) so as to not affect the combustion characteristics in the near-field region where measurements were taken (*i.e.*, the flames were over-ventilated). The excess O_2 in the exhaust in the experimental conditions are not representative of the requirement for practical boilers and furnace operations, but only a means to control for other sources of impact on soot and radiative heat flux in the laboratory experiments.

In order to isolate the effect of Z_{st} from other parameters the conditions were carefully designed: (1) the adiabatic flame temperature was maintained constant at 2595 K, while varying the amount of nitrogen in the fuel and oxidizer stream to allow Z_{st} to be varied. This was accomplished as described in Du et al. [187]. For flames that are not very intense radiators, as in the near-field, this

has been shown to be a reasonable means to maintain the same flame temperature to leading order. (2) To minimize the impact of mixing, the velocities of the gases from each stream were kept nearly constant between the cases. This ensured that the relative velocities were the same, and hence the near-field mixing was similar [199, 200]. The Reynolds numbers were also similar. Similar velocities for all cases also ensured that the local residence times (related to mixing and hence strain rate) and global residence times (related to superficial velocities) were similar. Hence, the measurements in the flame region for any case, at any given location could be easily compared with another case at the same location.

To maintain similar velocities, the thermal input was changed between the cases (as can be seen from Table 1). This does not affect the radiative heat flux in the rising region of the radiative heat flux [201]. In other words, changing thermal input only affects the flame length. In the flame region, while the radiative heat flux is still rising, there is minimal impact on the radiative heat flux. All measurements were conducted only up to 0.51 m from the burner, i.e. until the location of port 4, which is less than the flame length of the shortest flame (corresponding to the highest Z_{st}), so as to ensure that the radiative heat flux of the three cases could be compared.

Thus, the experimental conditions were carefully designed to isolate and study the impact of stoichiometric mixture fraction on soot formation in turbulent diffusion flames. The impact of flame temperature, superficial velocities (and hence residence time), mixing between fuel and oxidizer, were kept constant between the three cases studied. The lower limit of Z_{st} was set to 0.38 due to a limitation on the maximum propane thermal input that could be supplied, based on the reactor's feed gas control systems, while keeping the velocity of the gas constant. As will be seen in the results section, the range of Z_{st} considered in this study clearly shows the sought-after trends.

Finally, it is important to note that unlike industrial boilers and furnaces, which will operate with 3-5% O₂ in the exhaust gas, and CO₂ as the most likely inert for oxy-combustion, these experimental conditions were chosen to minimize the effect of all parameters other than Z_{st} that can affect soot and radiative heat flux. Thus, the experimental conditions are not practical operating conditions, but a means to isolate and clarify the role of Z_{st} .

Table B-1. Operating condition parameters.

Z_{st}	Fuel stream (central tube)			Oxidizer stream (co-annular tube)		
	Q (m ³ /h) ^a	C ₃ H ₈ (%v)	Vel (m/s) ^b	Q (m ³ /h) ^a	O ₂ (%v)	Vel (m/s) ^b
0.38	2.8	15.9	8.3	14	47.8	1.5
0.48	2.8	12.4	8.3	14	57.7	1.5
0.68	2.8	8.5	8.4	14	100	1.6

^aAt room temperature and pressure, corresponding to 293 K and 1 bar.

^bVelocities are superficial velocities.

B.2.3 Measurement Instruments

Photographs – Camera Settings:

In order to get a visual sense of the effect of Z_{st} on the flame, and to qualitatively understand the impact on soot inception, concentration, and flame emission intensities, a Nikon D3200 digital camera was used to photograph the flame at each port, down to port 4 (0.51 m from the burner). All photographs were taken using the same camera settings. The exposure time was 1/30 s, the aperture was set at f/9, and the ISO was 200. Focus was adjusted manually to obtain the best image of the flame. For each condition, at each port, multiple pictures were taken, and one representative picture for each condition-port combination is shown in this paper.

Heat Flux:

Radiative heat flux was measured using a Gardon Gage Sensor with a sapphire window, manufactured by Medtherm Corporation (part number for sensor: 64-50-20, and window: SW-1C-150). The sensor nominal absorptance is 0.92 from 0.6 μm to 15.0 μm . The sapphire window eliminates convective heat transfer and allows radiative heat flux to be measured. The sapphire window has a nominal transmittance of 0.85. The arrangement has a 150° view angle. The sensor body and casing are water cooled. The heat flux sensor's voltage output was converted into a heat flux reading in kW/m^2 using NIST traceable calibration curves, and recorded in LabView. The calibration was done using a blackbody furnace by the sensor supplier (Medtherm Corp.).

Spectrometer:

Radiative emission from gas species in a flame is restricted to certain narrow bands, while radiation from soot is broadband. The intensity of the broadband emission is a function of both temperature and emissivity, and the soot emissivity is related to the soot volume fraction. Emission from the flame in the UV-visible region was measured using a modular spectrometer – USB2000+ UV-Vis-ES, manufactured by Ocean Optics. The measurement range of the spectrometer is from 200 nm to 800 nm, and the spectral resolution is 1.5 nm FWHM. The integration time was varied based on the emission intensity. To obtain a line-of-sight measurement, a collimating lens with a 9.6° view-angle was fixed to the center of a flange, which could be moved from port-to-port on the reactor, and thus the lens could be centered at each port. A 600 μm fiber bundle was used to transmit the light from the collimating lens to the spectrometer.

The raw output of the spectrometer is converted to absolute units by calibration using a halogen lamp (HL-200), also manufactured by Ocean Optics, with a known emission spectrum. Further confirmation of the calibration was performed using a black body furnace (Newport, model

number 67032) in a dark room, at two different temperatures, 1273 K and 1473 K, with all the optics as in the actual experiment. The distance between the black body furnace and the collimating lens was the same as that between the flame and the collimating lens during experiments. The difference between the black body test and halogen lamp calibration was less than 5%.

The absolute irradiance calculated from the spectrometer measurement was then fit to Planck's black body equation with appropriate modifications, , i.e.,

$$I_P = \frac{\varepsilon \Omega C_1}{\lambda^5} \frac{1}{e^{\frac{C_2}{\lambda T}} - 1} \quad (\text{B-3})$$

where I_P is the absolute irradiance from the flame at a wavelength, λ , ε is the emissivity of the medium, Ω is the solid angle, T is the temperature, and C_1 and C_2 are the Planck's law constants.

For each condition at each port, 100 scans were taken. Each scan, consisting of the distribution of intensity of emission from the soot, was then fit to the theoretical Planck's equation in the red region of the visible range (650 nm – 700 nm). In this wavelength range, the variation in the imaginary part of the refractive index is less than 0.08%, and hence ε can be approximated to be constant in this wavelength range. Then values for ε and T were obtained, and the mean and standard deviation were calculated. The wavelength range for the curve fit was further reduced to 20 nm to confirm that the wavelength dependence is negligible. Because the soot volume fraction is directly related to the emissivity of the emitting medium (soot) in the visible range, this calculated emissivity was used as a measure of the relative amounts of soot at each port for each condition.

B.3 Results

The effect of Z_{st} on the visible flame emission is shown in Figure 2, which contains images obtained from the digital camera. This can provide insight into the location of soot inception, since visual observation of the onset of soot luminosity is an effective means of detecting the location of soot inception, and is, in many cases more sensitive than inception obtained by laser scattering measurements, as noted by Du et al. [202]. The camera settings were held constant so that the image intensities can be directly compared. The aperture was set such that the blue zone was visible, which in some cases caused the yellow region to become saturated. The blue emission is due to the flame radicals, while the yellow emission is due to soot.

Since the camera settings and the adiabatic flame temperature were kept the same, intensity of the luminosity (or intensity) of the yellow light is an indicator of the amount of soot. From Figure 2 it can be inferred that as Z_{st} is increased, the soot inception location is pushed downstream, and the overall soot volume fraction is also reduced. At low Z_{st} ($Z_{st} = 0.38$), the flame is predominantly blue for much of the first port but yellow emission rapidly increases until the flame has a pronounced bright yellow emission at Ports 3 (0.36 m) and 4 (0.51 m). At high Z_{st} ($Z_{st} = 0.68$), the flame has a predominantly blue color for a long length, and even at distances as long as 0.36 m (Port 3) and 0.51 m (Port 4) the flame is blue with dull yellow emission, in clear contrast to the lower Z_{st} flames.

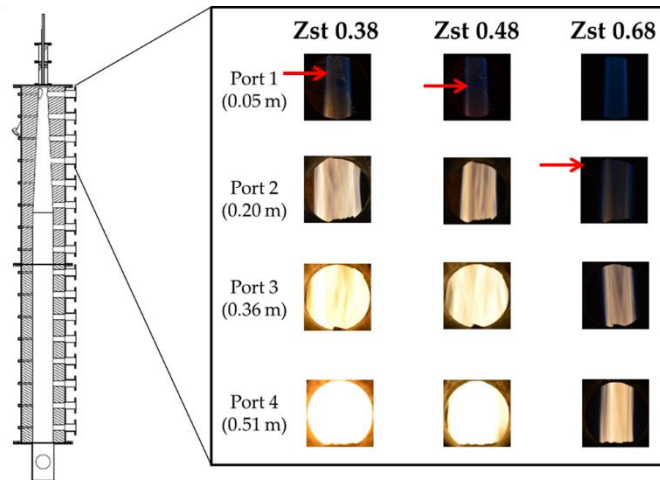


Figure B-2. The effect of Z_{st} on the soot inception location and soot volume fraction at various axial locations, as seen from the luminosity of the flame. Red arrows mark soot inception location.

Figure 3 shows the line-of-sight emissivities from the flames in the narrow wavelength range between 650 nm – 700 nm. The error bars represent one standard deviation from the mean. All the relevant gases in the flame (CO_2 and H_2O) are narrow-band emitters in the infrared. Also, emission from flame radicals is limited to the UV and blue regions of the spectrum. Thus, the emissivity shown in Figure 3 can be considered to be solely due to soot. As Z_{st} is increased, the line-of-sight intensity and emissivity decrease at each axial position. At shorter axial distances, the emissivity is low and increases significantly with axial distance for the lower Z_{st} cases, whereas for the highest Z_{st} , the increase is rather limited. For all three cases, due to negligible soot and hence very low emission at port 1 (0.05 m from the burner), the signal to noise ratio was too low to calculate the emissivities. For the highest Z_{st} case, the broadband emission was not intense enough even at port 2 (0.2 m) and hence for this case the emissivity is only shown for ports 3 and 4 (0.36 m and 0.51 m).

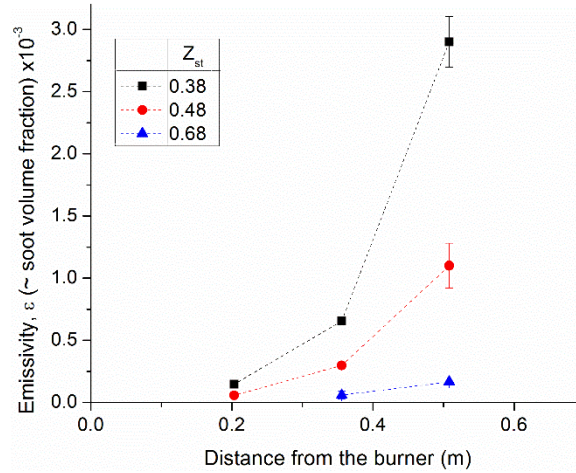


Figure B-3. Line of sight emissivity at various axial position for three different Z_{st} cases. Soot volume fraction is proportional to the emissivity.

Since the emissivities are low, the soot volume fractions are directly proportional to emissivity. The derivation follows from Beer–Lambert’s law and Kirchhoff’s law combined, and by assuming soot falls under the Rayleigh regime in the visible wavelength spectrum. The soot volume fraction can then be approximated to be [203]

$$f_v \approx \frac{\lambda}{6\pi L} \left| \frac{m^2 + 2}{m^2 - 1} \right| \varepsilon \quad (\text{B-4})$$

where, λ is the wavelength of light used for this calculation (the same as used for the calculation of ε), and m is the complex refractive index of soot. Thus, the ordinate in Figure 3 (emissivity) is proportional to the soot volume fraction.

Figure 4 shows the radiative heat flux from the flame for the three Z_{st} conditions. The error bars represent one standard deviation on each side. Increasing Z_{st} reduces the radiative heat flux at a given port. The radiative heat flux at 0.05 m (Port 1) is similar for all three cases, but the profiles diverge along the reactor. The radiative heat fluxes for the two lower Z_{st} cases increase sharply with distance from the burner, whereas that for the highest Z_{st} is relatively flat. The increase in

radiative heat flux between 0.05 and 0.51 m is more than three times greater for $Z_{st} = 0.38$ than for $Z_{st} = 0.68$.

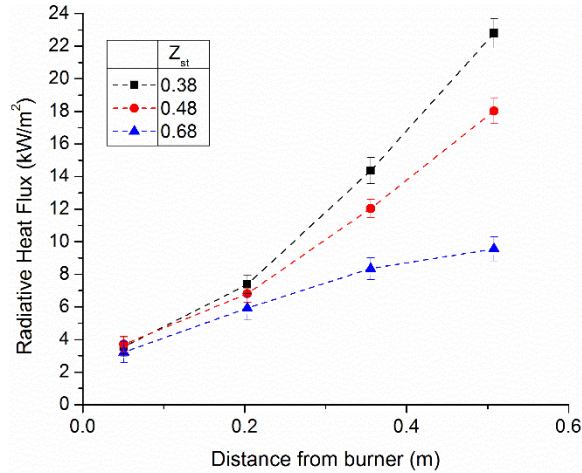


Figure B-4. Radiant heat flux profiles for the three Z_{st} cases.

The extremely low soot volume fraction along the reactor for $Z_{st} = 0.68$ as shown by the emissivity data (Figure 3) as well as the photographs (Figure 2), indicates that the radiative emission from this flame is primarily due to gaseous radiation. The radiative heat flux results illustrate that very effective control of radiation heat transfer can be achieved without compromising flame temperature by controlling the placement of inert gases. For example, at a position of 0.5 m from the burner, the radiative heat flux for $Z_{st} = 0.68$ is reduced by approximately 60% from that of $Z_{st} = 0.38$.

B.4 Discussion

In this study, we showed that for a high temperature flame ($T_{ad} \sim 2600$ K), radiative heat flux and soot can be reduced by strategic placement of the inert, such that Z_{st} is increased, without changing the adiabatic flame temperature. Increasing Z_{st} of the flame also delayed soot inception. An explanation of the way Z_{st} affects soot and radiative heat flux in turbulent jet flames is provided below. Since for a given adiabatic flame temperature, the radiative heat flux is primarily related to the amount of soot, emphasis is placed on understanding soot inception and growth.

In any non-premixed flame, soot inception is dominant in the region closest to the burner nozzle, and the increase in soot mass is primarily due to nucleation [196]. Further downstream, soot mass addition is due to growth on existing soot nuclei, before it finally gets oxidized. A comparison of the reduction in soot with changing Z_{st} in the early regions of the flame, where soot mass growth is dominated by soot inception (or nucleation), could provide an insight into the mechanism driving soot inception in a turbulent jet diffusion flame.

Regions of high Z , *i.e.*, deep in the fuel-rich side of the flame, are dominated by *fuel-pyrolysis pathways* towards PAH (polycyclic aromatic hydrocarbons), which are the immediate precursors of soot. Fuel pyrolysis leads to the formation of but-2-yn-1-yl (C_4H_5-2), which is converted to benzene by addition of acetylene [141],



Since this reaction for C_4H_5-2 is exothermic and involves acetylene, it is found in fuel-rich regions away from the flame [141]. The low-temperature, fuel-pyrolysis pathway to benzene scales with fuel concentration at the inlet [141]. Increasing Z_{st} also increases fuel dilution, which reduces the fuel mass fraction at inlet, and reduces soot formation via the fuel-pyrolysis pathway.

The experimental results indicate that the reduction in soot volume fraction between the three cases is much more than can be explained by fuel dilution alone. For example, the soot volume fraction reduces 3 times more than the fuel inlet concentration when Z_{st} is changed from 0.38 to 0.48. When compared to Z_{st} 0.68, the differences are even greater. Thus, it can be concluded that a different mechanism for soot inception must be dominant in such systems.

To better understand the effect of Z_{st} on soot formation, a computational fluid dynamic (CFD) simulation of the flame was performed using the Reynolds-Averaged Navier-Stokes equations with the SST $k-\omega$ turbulence model [127], and a detailed chemical mechanism for propane combustion [204]. The simulation performed was primarily to compare the variation in flame structure of the three cases in the early region of the flame (Port 1) where soot inception is the dominant path of soot addition. Figure 5 shows the species and temperature profile in the mixture fraction space, as obtained from the simulations, at the first port for the three cases. In this zone, in mixture fraction space, or even physical space in the radial direction, further classification is possible. Close to the flame, i.e., at $Z \approx Z_{st}$, on the fuel-rich side, the *propargyl self-combination pathway* to soot precursor formation dominates the soot formation [141, 151]. Propargyl (C_3H_3) is produced via the oxidation (removal of H-radicals) of acetylene by methyl and methylene radicals supplied from the oxidation (flame) region:



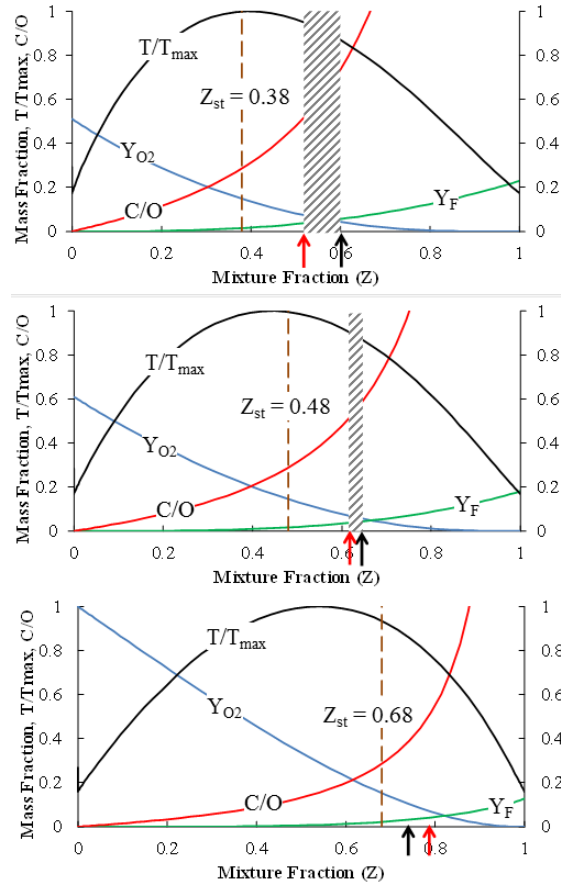


Figure B-5. Flame structure, i.e., species and temperature profiles in mixture fraction (Z) space at 0.05 m from the burner. The black and red arrow mark the locations of the low temperature and C/O ratio bounds for ring formation respectively. Between them is the shaded region where soot can form. Note: For $Z_{st} = 0.68$, the temperature limit is on the other side of the C/O limit, thus no soot can form.

This pathway is endothermic and hence requires higher temperatures. This pathway also produces H-radicals, and hence in regions where the H-radical concentrations are high due to H supplied from the fuel oxidation reactions, a reduction or even reversal of this pathway to soot precursor formation can occur [141]. The carbon to oxygen atom ratio (C/O ratio) is correlated with the presence of H-radicals, and each fuel has a critical C/O ratio at which the H-radical concentration is high enough to prevent soot formation via the propargyl self-combination pathway, which for propane is approximately 0.51 [141-143, 152]. As can be seen in Figure 5, with increasing Z_{st} , the location of $(C/O)_{cr}$ (marked by the red arrow on the abscissa) shifts further towards the right, i.e.,

the fuel side. This is because with increasing Z_{st} the flame structure changes, and the flame is closer to the fuel boundary. Furthermore, soot formation requires a minimum temperature to overcome the activation energy barrier. This low-temperature bound is dependent on the fuel concentration [143], and is shown in Figure 5 by the black arrow on the abscissa. The simulation results show that at Port 1, for $Z_{st} = 0.38$, a small zone exists where soot can form (shaded region in Figure 5), and with increasing Z_{st} the zone shrinks, and for high enough Z_{st} ($Z_{st} = 0.68$) the two boundaries cross over, thereby preventing any soot formation via the propargyl self-combination pathway. This pathway to soot inception in turbulent jet diffusion flames is the dominant pathway, similar to laminar counter-flow systems [141]. With increasing Z_{st} , in this pathway, the flame structure changes, such that the two bounds for this pathway – the high temperature region and the high C/O region – are brought closer and closer together, reducing the time for propargyl formation, and subsequently soot inception.

Furthermore, the reduced soot nucleation that is observed at high Z_{st} is expected to yield slower soot growth downstream due to the reduction in nuclei for growth. However, there is likely an additional reason that the soot volume fraction is so low at high Z_{st} . Mueller et al. [196] have shown that in turbulent jet flames the primary mechanism for soot growth is via PAH condensation, rather than acetylene-based surface reactions. Thus, the mechanism of reduction of PAH with increasing Z_{st} , which was described above, could further exacerbate the reduction in soot growth because the PAH concentration is reduced at high Z_{st} . This implies that high Z_{st} suppresses both soot nucleation and growth by reducing PAH.

B.5 Conclusions

This is the first controlled study to isolate the effect of varying Z_{st} in a turbulent non-premixed flame, and also the first study to directly measure the impact of Z_{st} on overall soot volume fraction and radiative heat flux. At low Z_{st} , soot inception starts early and soot grows rapidly with distance from the burner. As the stoichiometric mixture fraction was increased, the soot concentration and radiative heat flux decreased drastically, and the region of soot inception was forced downstream. At high Z_{st} , nearly blue, soot-free, flames were maintained for a much longer length along the furnace.

The push to mitigate greenhouse gas emissions from fossil fuel combustion, and the potential of oxy-combustion as a possible strategy for this, emphasizes the need to understand the role of inert placement (Z_{st}) on soot formation and radiative heat flux in turbulent flames. The ability to independently decide on the amount of inert supplied to the oxidizer and fuel during oxy-combustion makes strategic placement of inert to control Z_{st} an important tool for controlling radiative heat flux. While we have shown that soot formation and radiative heat flux can be reduced for a given flame temperature, a natural corollary of this is that the same radiative heat flux can be achieved at higher flame temperature (i.e., with less inert, or less flue-gas recycle). By controlling Z_{st} , the control of wall radiative heat flux can shift from relying on control of flame temperature to controlling the soot concentration, because by controlling Z_{st} , soot formation and growth can be reduced, while still maintaining a high flame temperature. In practical oxy-combustion furnaces and boilers, since recycled flue gas (CO_2) will be used as the inert, the reduction in soot will be even more due to the increased gasification (consumption) of soot by CO_2 . The reduced inert requirement could increase the process efficiency and reduce costs for practical industrial processes or power plants.

B.6 Acknowledgements

The authors would like to thank Prof. P. B. Sunderland and Mr. Zhengyang Wang at University of Maryland for their help in the blackbody calibration of the spectrometer. The authors would also like to acknowledge the efforts of Mr. George Pires for the help during the construction of the test facility.

Funding

The financial support for the project was provided by the Consortium for Clean Coal Utilization at Washington University in St. Louis.

Appendix C

Burke-Schumann Model Formulation for Tri-Axial Flames

The Burke-Schumann model is a flame model for non-premixed laminar flames. Originally it was derived for a burner configuration with the fuel in the center and oxidizer surrounding the fuel coaxially (normal configuration) [153]. In Chapter 7, the theoretical analysis of a tri-axial flame with the fuel in the middle tube was carried out (see Figure C-1). This analysis utilized the tri-axial flame formulation of Chao and Axelbaum [59], and extended the model to include the solution to the C/O atomic ratio to predict soot inception limits. Below, the basic formulation from [59] is presented along with the relevant additions. Since the burner and the flame are axi-symmetric, the equations solved are axi-symmetric with cylindrical coordinates.

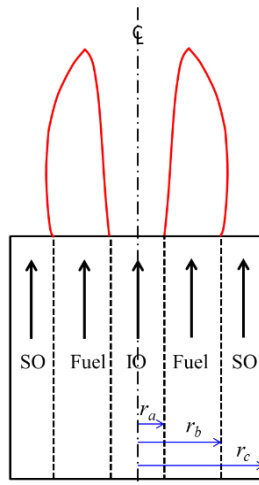


Figure C-1. Schematic of the tri-axial burner configuration

ASSUMPTIONS

- (1) same mass flux and temperature at the burner exit
- (2) λ , c_p and ρD_i are constants
- (3) unity Lewis number $Le_i = (\lambda / c_p) / (\rho D_i) = 1$ or $\rho D_F = \rho D_O = \lambda / c_p$
- (3) body force is negligible
- (4) flame sheet model
- (5) the external wall is adiabatic
- (6) isobaric flow
- (7) One-step, overall, irreversible reaction given by $v_F F + v_O O \rightarrow v_P P$

Inner tube : oxidizer + inert

Middle tube : fuel + inert (diluted fuel)

NOMENCLATURE

c_p	specific heat at constant pressure
D_i	mass diffusion coefficient of species i
F	fuel
O	oxidizer
P	combustion products
Pe	Peclet number defined as $\rho u r_c / (\lambda / c_p)$
q_F	heat of combustion per unit mass of the fuel consumed
r	radial spatial coordinate
r_a	radius of the inner tube
r_b	radius of the middle tube
r_c	radius of the outer tube
T	temperature
T_f	flame temperature
u	flow velocity
W_i	molecular weight of species i
$Y_{F,0}$	mass fraction of the fuel at the burner exit in the region $r_a < r < r_b$
Y_i	mass fraction of species i
$Y_{O,0}$	mass fraction of the oxidizer at the burner exit in the region $0 < r < r_a$
$Y_{O,c}$	mass fraction of the oxidizer at the burner exit in the region $r_b < r < r_c$
z	axial spatial coordinate
(r_f, z_f)	flame location
v_i	stoichiometric coefficient of species i
ρ	gas density
λ	thermal conductivity
ω	reaction rate function
\sim	nondimensional quantities

FORMULATION

(A) Non-dimensionalization

$$\tilde{T} = \frac{c_p T}{q_F}, \quad \tilde{Y}_F = Y_F, \quad \tilde{Y}_O = \frac{v_F W_F}{W_O} Y_O, \quad \tilde{r} = \frac{r}{r_c}, \quad \tilde{r}_a = \frac{r_a}{r_c}, \quad \tilde{r}_b = \frac{r_b}{r_c}, \quad \tilde{z} = \frac{z}{r_c}$$

$$\tilde{\omega} = \frac{v_F W_F r_c^2}{\lambda / c_p} \omega, \quad Pe = \frac{\rho u r_c}{\lambda / c_p} = \text{Peclet number}$$

(B) Conservation Equations

Applying the assumptions $\rho D_F = \rho D_O = \lambda / c_p$ with λ and c_p to be constants,

$$\rho u c_p \frac{\partial T}{\partial z} - \left[\frac{\partial}{\partial z} \left(\lambda \frac{\partial T}{\partial z} \right) + \frac{1}{r} \frac{\partial}{\partial r} \left(\lambda r \frac{\partial T}{\partial r} \right) \right] = v_F W_F q_F \omega$$

$$\rho u \frac{\partial Y_F}{\partial z} - \left[\frac{\partial}{\partial z} \left(\rho D_F \frac{\partial Y_F}{\partial z} \right) + \frac{1}{r} \frac{\partial}{\partial r} \left(\rho D_F r \frac{\partial Y_F}{\partial r} \right) \right] = -v_F W_F \omega$$

$$\rho u \frac{\partial Y_O}{\partial z} - \left[\frac{\partial}{\partial z} \left(\rho D_O \frac{\partial Y_O}{\partial z} \right) + \frac{1}{r} \frac{\partial}{\partial r} \left(\rho D_O r \frac{\partial Y_O}{\partial r} \right) \right] = -v_O W_O \omega$$

$$\rho u \frac{\partial Y_I}{\partial z} - \left[\frac{\partial}{\partial z} \left(\rho D_I \frac{\partial Y_I}{\partial z} \right) + \frac{1}{r} \frac{\partial}{\partial r} \left(\rho D_I r \frac{\partial Y_I}{\partial r} \right) \right] = 0$$

(C) Boundary Conditions

$$0 < r < r_c, \quad z = 0: \quad T = T_0$$

$$r_b < r < r_c, \quad z = 0: \quad Y_F = 0, \quad Y_O = Y_{O,c}$$

$$r = 0, \quad z > 0: \quad \partial T / \partial r = \partial Y_F / \partial r = \partial Y_O / \partial r = 0 \quad (\text{symmetric at the centerline})$$

$$r = r_c, \quad z > 0: \quad \partial T / \partial r = \partial Y_F / \partial r = \partial Y_O / \partial r = 0 \quad (\text{adiabatic})$$

$$0 < r < r_c, \quad z \rightarrow \infty: \quad \partial T / \partial z = \partial Y_F / \partial z = \partial Y_O / \partial z = 0 \quad (\text{solutions are bounded})$$

$$0 < r < r_a, \quad z = 0: \quad Y_F = 0, \quad Y_O = Y_{O,0}$$

$$r_a < r < r_b, \quad z = 0: \quad Y_F = Y_{F,0}, \quad Y_O = 0$$

Non-dimensional boundary conditions and conservation equations:

$$0 < \tilde{r} < \tilde{r}_a, \quad \tilde{z} = 0: \quad \tilde{Y}_F = \tilde{Y}_{F,0}, \quad \tilde{Y}_O = 0$$

$$\tilde{r}_a < \tilde{r} < \tilde{r}_b, \quad \tilde{z} = 0: \quad \tilde{Y}_F = 0, \quad \tilde{Y}_O = \tilde{Y}_{O,0}$$

$$0 < \tilde{r} < 1, \quad \tilde{z} = 0: \quad \tilde{T} = \tilde{T}_0$$

$$\tilde{r}_b < \tilde{r} < 1, \quad \tilde{z} = 0: \quad \tilde{Y}_F = 0, \quad \tilde{Y}_O = \tilde{Y}_{O,c}$$

$$\tilde{r} = 0, \quad \tilde{z} > 0: \quad \tilde{Y}_F = 0, \quad \partial \tilde{T} / \partial \tilde{r} = \partial \tilde{Y}_F / \partial \tilde{r} = \partial \tilde{Y}_O / \partial \tilde{r} = 0$$

$$\tilde{r} = 1, \quad \tilde{z} > 0: \quad \partial \tilde{T} / \partial \tilde{r} = \partial \tilde{Y}_F / \partial \tilde{r} = \partial \tilde{Y}_O / \partial \tilde{r} = 0$$

$$0 < \tilde{r} < 1, \quad \tilde{z} \rightarrow \infty: \quad \partial \tilde{T} / \partial \tilde{z} = \partial \tilde{Y}_F / \partial \tilde{z} = \partial \tilde{Y}_O / \partial \tilde{z} = 0$$

$$\begin{aligned}
(1) \quad & \rho u \frac{\partial T}{\partial z} - \frac{\lambda}{c_p} \left[\frac{\partial^2 T}{\partial z^2} + \frac{1}{r} \frac{\partial}{\partial r} \left(r \frac{\partial T}{\partial r} \right) \right] = \nu_F W_F (q_F / c_p) \omega \\
& \frac{q_F}{c_p} \left\{ \frac{\lambda / c_p}{r_c} P e \frac{\partial \tilde{T}}{r_c \partial \tilde{z}} - \frac{\lambda}{c_p} \frac{1}{r_c^2} \left[\frac{\partial^2 \tilde{T}}{\partial \tilde{z}^2} + \frac{1}{\tilde{r}} \frac{\partial}{\partial \tilde{r}} \left(\tilde{r} \frac{\partial \tilde{T}}{\partial \tilde{r}} \right) \right] \right\} = \nu_F W_F \frac{q_F}{c_p} \frac{\lambda / c_p}{\nu_F W_F r_c^2} \tilde{\omega} \Rightarrow P e \frac{\partial \tilde{T}}{\partial \tilde{z}} - \frac{\partial^2 \tilde{T}}{\partial \tilde{z}^2} - \frac{1}{\tilde{r}} \frac{\partial}{\partial \tilde{r}} \left(\tilde{r} \frac{\partial \tilde{T}}{\partial \tilde{r}} \right) = \tilde{\omega} \\
(2) \quad & \rho u \frac{\partial Y_F}{\partial z} - \frac{\lambda}{c_p} \left[\frac{\partial^2 Y_F}{\partial z^2} + \frac{1}{r} \frac{\partial}{\partial r} \left(r \frac{\partial Y_F}{\partial r} \right) \right] = -\nu_F W_F \omega \\
& \frac{\lambda / c_p}{r_c} P e \frac{\partial \tilde{Y}_F}{r_c \partial \tilde{z}} - \frac{\lambda}{c_p} \frac{1}{r_c^2} \left[\frac{\partial^2 \tilde{Y}_F}{\partial \tilde{z}^2} + \frac{1}{\tilde{r}} \frac{\partial}{\partial \tilde{r}} \left(\tilde{r} \frac{\partial \tilde{Y}_F}{\partial \tilde{r}} \right) \right] = -\nu_F W_F \frac{\lambda / c_p}{\nu_F W_F r_c^2} \tilde{\omega} \Rightarrow P e \frac{\partial \tilde{Y}_F}{\partial \tilde{z}} - \frac{\partial^2 \tilde{Y}_F}{\partial \tilde{z}^2} - \frac{1}{\tilde{r}} \frac{\partial}{\partial \tilde{r}} \left(\tilde{r} \frac{\partial \tilde{Y}_F}{\partial \tilde{r}} \right) = -\tilde{\omega} \\
(1) + (2) : \quad & P e \frac{\partial (\tilde{T} + \tilde{Y}_F)}{\partial \tilde{z}} - \frac{\partial^2 (\tilde{T} + \tilde{Y}_F)}{\partial \tilde{z}^2} - \frac{1}{\tilde{r}} \frac{\partial}{\partial \tilde{r}} \left[\tilde{r} \frac{\partial (\tilde{T} + \tilde{Y}_F)}{\partial \tilde{r}} \right] = 0 \\
(3) \quad & \rho u \frac{\partial Y_O}{\partial z} - \frac{\lambda}{c_p} \left[\frac{\partial^2 Y_O}{\partial z^2} + \frac{1}{r} \frac{\partial}{\partial r} \left(r \frac{\partial Y_O}{\partial r} \right) \right] = -\nu_O W_O \omega \\
& \frac{\nu_O W_O}{\nu_F W_F} \left\{ \frac{\lambda / c_p}{r_c} P e \frac{\partial \tilde{Y}_O}{r_c \partial \tilde{z}} - \frac{\lambda}{c_p} \frac{1}{r_c^2} \left[\frac{\partial^2 \tilde{Y}_O}{\partial \tilde{z}^2} + \frac{1}{\tilde{r}} \frac{\partial}{\partial \tilde{r}} \left(\tilde{r} \frac{\partial \tilde{Y}_O}{\partial \tilde{r}} \right) \right] \right\} = -\nu_O W_O \frac{\lambda / c_p}{\nu_F W_F r_c^2} \tilde{\omega} \\
& \Rightarrow P e \frac{\partial \tilde{Y}_O}{\partial \tilde{z}} - \frac{\partial^2 \tilde{Y}_O}{\partial \tilde{z}^2} - \frac{1}{\tilde{r}} \frac{\partial}{\partial \tilde{r}} \left(\tilde{r} \frac{\partial \tilde{Y}_O}{\partial \tilde{r}} \right) = -\tilde{\omega} \\
(2) - (3) : \quad & P e \frac{\partial (\tilde{Y}_F - \tilde{Y}_O)}{\partial \tilde{z}} - \frac{\partial^2 (\tilde{Y}_F - \tilde{Y}_O)}{\partial \tilde{z}^2} - \frac{1}{\tilde{r}} \frac{\partial}{\partial \tilde{r}} \left[\tilde{r} \frac{\partial (\tilde{Y}_F - \tilde{Y}_O)}{\partial \tilde{r}} \right] = 0 \\
(4) \quad & \rho u \frac{\partial Y_I}{\partial z} - \left[\frac{\partial}{\partial z} \left(\rho D_I \frac{\partial Y_I}{\partial z} \right) + \frac{1}{r} \frac{\partial}{\partial r} \left(\rho D_I r \frac{\partial Y_I}{\partial r} \right) \right] = 0 \Rightarrow P e \frac{\partial (\tilde{Y}_I)}{\partial \tilde{z}} - \frac{\partial^2 (\tilde{Y}_I)}{\partial \tilde{z}^2} - \frac{1}{\tilde{r}} \frac{\partial}{\partial \tilde{r}} \left[\tilde{r} \frac{\partial (\tilde{Y}_I)}{\partial \tilde{r}} \right] = 0
\end{aligned}$$

(H) Summary

Coupling Functions

$$\begin{aligned}
\tilde{Y}_F - \tilde{Y}_O = & \tilde{Y}_{F,0}(\tilde{r}_b^2 - \tilde{r}_a^2) - \tilde{Y}_{O,0}\tilde{r}_a^2 - \tilde{Y}_{O,c}(1 - \tilde{r}_b^2) \\
& + 2 \sum_{n=1}^{\infty} \frac{(\tilde{Y}_{F,0} + \tilde{Y}_{O,c})\tilde{r}_b J_1(k_n \tilde{r}_b) - (\tilde{Y}_{F,0} + \tilde{Y}_{O,0})\tilde{r}_a J_1(k_n \tilde{r}_a)}{k_n J_0^2(k_n)} J_0(k_n \tilde{r}) \exp \left[\left(P e - \sqrt{P e^2 + 4k_n^2} \right) \tilde{z} / 2 \right]
\end{aligned}$$

$$\tilde{T} + \tilde{Y}_F = \tilde{T}_0 + \tilde{Y}_{F,0}(\tilde{r}_b^2 - \tilde{r}_a^2) + 2\tilde{Y}_{F,0} \sum_{n=1}^{\infty} \frac{\tilde{r}_b J_1(k_n \tilde{r}_b) - \tilde{r}_a J_1(k_n \tilde{r}_a)}{k_n J_0^2(k_n)} J_0(k_n \tilde{r}) \exp \left[\left(P e - \sqrt{P e^2 + 4k_n^2} \right) \tilde{z} / 2 \right]$$

Flame Sheet Location and Flame Temperature

$$\begin{aligned}
0 = & \tilde{Y}_{F,0}(\tilde{r}_b^2 - \tilde{r}_a^2) - \tilde{Y}_{O,0}\tilde{r}_a^2 - \tilde{Y}_{O,c}(1 - \tilde{r}_b^2) \\
& + 2 \sum_{n=1}^{\infty} \frac{(\tilde{Y}_{F,0} + \tilde{Y}_{O,c})\tilde{r}_b J_1(k_n \tilde{r}_b) - (\tilde{Y}_{F,0} + \tilde{Y}_{O,0})\tilde{r}_a J_1(k_n \tilde{r}_a)}{k_n J_0^2(k_n)} J_0(k_n \tilde{r}_f) \exp \left[\left(P e - \sqrt{P e^2 + 4k_n^2} \right) \tilde{z}_f / 2 \right]
\end{aligned}$$

$$\tilde{T}_f = \tilde{T}_0 + \tilde{Y}_{F,0}(\tilde{r}_b^2 - \tilde{r}_a^2) + 2\tilde{Y}_{F,0} \sum_{n=1}^{\infty} \frac{\tilde{r}_b J_1(k_n \tilde{r}_b) - \tilde{r}_a J_1(k_n \tilde{r}_a)}{k_n J_0^2(k_n)} J_0(k_n \tilde{r}_f) \exp \left[\left(P e - \sqrt{P e^2 + 4k_n^2} \right) \tilde{z}_f / 2 \right]$$

Transition between the over-ventilated and under-ventilated flames occurs when

$$\tilde{Y}_{F,0}(\tilde{r}_b^2 - \tilde{r}_a^2) - \tilde{Y}_{O,0}\tilde{r}_a^2 - \tilde{Y}_{O,c}(1 - \tilde{r}_b^2) = 0$$

Temperature and Species Distribution at any z , $\tilde{r} < \tilde{r}_{f,i}$ and $\tilde{r} > \tilde{r}_{f,o}$

$$\tilde{Y}_F = 0$$

$$\begin{aligned} \tilde{Y}_O &= \tilde{Y}_{O,0}\tilde{r}_a^2 + \tilde{Y}_{O,c}(1 - \tilde{r}_b^2) - \tilde{Y}_{F,0}(\tilde{r}_b^2 - \tilde{r}_a^2) \\ &- 2 \sum_{n=1}^{\infty} \frac{(\tilde{Y}_{F,0} + \tilde{Y}_{O,c})\tilde{r}_b J_1(k_n \tilde{r}_b) - (\tilde{Y}_{F,0} + \tilde{Y}_{O,0})\tilde{r}_a J_1(k_n \tilde{r}_a)}{k_n J_0^2(k_n)} J_0(k_n \tilde{r}) \exp\left[\left(\text{Pe} - \sqrt{\text{Pe}^2 + 4k_n^2}\right)\tilde{z}/2\right] \\ \tilde{T} &= \tilde{T}_0 + \tilde{Y}_{F,0}(\tilde{r}_b^2 - \tilde{r}_a^2) + 2\tilde{Y}_{F,0} \sum_{n=1}^{\infty} \frac{\tilde{r}_b J_1(k_n \tilde{r}_b) - \tilde{r}_a J_1(k_n \tilde{r}_a)}{k_n J_0^2(k_n)} J_0(k_n \tilde{r}) \exp\left[\left(\text{Pe} - \sqrt{\text{Pe}^2 + 4k_n^2}\right)\tilde{z}/2\right] \end{aligned}$$

Temperature and Species Distribution at any z , $\tilde{r}_{f,i} < \tilde{r} < \tilde{r}_{f,o}$

$$\tilde{Y}_O = 0$$

$$\begin{aligned} \tilde{Y}_F &= \tilde{Y}_{F,0}(\tilde{r}_b^2 - \tilde{r}_a^2) - \tilde{Y}_{O,0}\tilde{r}_a^2 - \tilde{Y}_{O,c}(1 - \tilde{r}_b^2) \\ &+ 2 \sum_{n=1}^{\infty} \frac{(\tilde{Y}_{F,0} + \tilde{Y}_{O,c})\tilde{r}_b J_1(k_n \tilde{r}_b) - (\tilde{Y}_{F,0} + \tilde{Y}_{O,0})\tilde{r}_a J_1(k_n \tilde{r}_a)}{k_n J_0^2(k_n)} J_0(k_n \tilde{r}) \exp\left[\left(\text{Pe} - \sqrt{\text{Pe}^2 + 4k_n^2}\right)\tilde{z}/2\right] \\ \tilde{T} &= \tilde{T}_0 + \tilde{Y}_{O,0}\tilde{r}_a^2 + \tilde{Y}_{O,c}(1 - \tilde{r}_b^2) + 2 \sum_{n=1}^{\infty} \frac{\tilde{Y}_{O,0}\tilde{r}_a J_1(k_n \tilde{r}_a) - \tilde{Y}_{O,c}\tilde{r}_b J_1(k_n \tilde{r}_b)}{k_n J_0^2(k_n)} J_0(k_n \tilde{r}) \exp\left[\left(\text{Pe} - \sqrt{\text{Pe}^2 + 4k_n^2}\right)\tilde{z}/2\right] \end{aligned}$$

Appendix D

Effects of biomass moisture content on volatile flame length during co-firing with coal

Akshay Gopan, Matthew M. Pollard, Zhiwei Yang, Melissa L. Holtmeyer, and Richard L.

*Axelbaum**

**Corresponding Author*

Department of Energy, Environmental and Chemical Engineering
Washington University in St. Louis
One Brookings Drive, Campus Box 1180
St. Louis, MO 63130, U.S.A.

Keywords: Biomass co-firing; flame length; moisture; volatile breakthrough

Abstract

Co-firing biomass with coal can reduce pollutant emissions and consumption of fossil fuels and, where applicable, contribute to meeting Renewable Portfolio Standards (RPS). The physical characteristics and composition of biomass can vary significantly, and these can affect the combustion characteristics. When co-firing biomass with coal, these differences can impact the

structure of the volatile flame, the region where combustion of volatiles dominates. The length and size of the volatile flame are important to flame stability and are dependent upon the location and extent of volatile release. This, in turn, has an effect on emission of pollutants, such as NO_x (nitrogen oxides). Previously, the effects of co-firing ratio, particle size and air-fired versus oxyfuel conditions on volatile flame length and breakthrough were studied. Breakthrough is the phenomenon whereby fuel particles pass through the volatile flame without completely releasing their volatiles. This paper focuses on the effects of biomass moisture content on flame length and volatile breakthrough when firing PRB coal with oakwood sawdust. Experiments were performed at $18 \text{ kW}_{\text{th}}$ net thermal input, with 80 wt% coal/20 wt.% sawdust. The sawdust moisture content was varied from 10 to 30%. The volatile flame length was determined by CO and CO_2 profile measurements along the centerline of the flame. Volatile breakthrough was measured by particle sampling immediately downstream of the volatile flame. Contrary to what might be expected, volatile flame length reduces as biomass moisture increases. Increasing moisture leads to more volatile breakthrough, which results in a shorter volatile flame. Moisture influences the time for drying as well as the particle size distribution due to swelling and clumping. A characteristic time analysis was used to determine the mechanism by which moisture content affects the volatile flame length; either by increasing the drying time, particle swelling or particle clumping (increased particle size). The results indicate, for the cases under consideration, moisture vaporization has an order of magnitude lower impact on devolatilization delay as compared to the delay due to the larger clump size and the corresponding longer particle heating times.

D.1 Introduction

Coal continues to be a major source of energy in the world, but contributes to global climate change as it produces more CO₂ per unit energy than any other fuel. Co-firing biomass with coal can reduce not only emissions of criteria pollutants, like SO_x and NO_x [205, 206], but also net carbon dioxide emissions [207]. As the carbon released from biomass combustion is fixed at relatively small time scales, its considered to be carbon neutral. Several facilities in the United States and Europe are currently implementing biomass co-firing, predominantly at low co-firing ratios, as part of their Renewable Portfolio Standards (RPS) or equivalent [208-210]. Furthermore, it has the potential for carbon negative power generation if combined with Carbon Capture, Utilization and Sequestration (CCUS) [211, 212]. Even though biomass co-firing provides a renewable alternative to coal-only operations, there are challenges when implementing it on an industrial scale.

Pulverized fuel flames typically have two distinct combustion zones: the volatile flame zone and the heterogeneous (char) combustion zone [213, 214]. The volatile flame zone, otherwise known as the volatile reaction zone, is characterized by rapid release of volatiles and their subsequent combustion with oxygen, and is the primary region of soot formation and radiation. Fuel enters the furnace, being carried by the primary oxidizer (PO), and after exiting the nozzle, the fuel particles experience heating, moisture evaporation, and devolatilization. The released volatiles react with the oxygen in the PO such that the local oxygen is consumed quickly, but the majority of the volatiles are not consumed. The fuel continues to devolatilize and travel through the furnace and the volatiles subsequently react with the secondary oxidizer (SO). The end of this “non-premixed” volatile reaction zone marks the end of the volatile flame. The distance from the injection nozzle to the end of the volatile flame is known as the volatile flame length.

Solid fuel particles can pass through the volatile flame and enter the heterogeneous combustion zone without being completely devolatilized, a phenomena known as “volatile breakthrough” [215]. Breakthrough may result in incomplete combustion, leading to lower boiler efficiency. The length of the volatile flame is a key factor affecting volatile breakthrough, as it affects particle residence time in the volatile flame zone [216]. The heterogeneous combustion zone is characterized as an oxygen-rich environment where char burnout occurs.

Previously, in the same experimental facility, the effects of biomass co-firing ratio, biomass particle size, and air-fired versus oxy-fuel combustion on the volatile flame length and volatile breakthrough were studied [215, 216]. Moisture content of biomass fuels is another important parameter, and one that varies significantly between fuels and even for the same fuel. And, unlike the previously studied parameters, moisture content can also be strongly affected by the history of the biomass, and the local ambient conditions.

Since vaporization of moisture is one of the first steps leading to volatile release, it is important to understand its impact on volatile flame length and volatile breakthrough. Using experiments and analytical methods, this work seeks to understand the impact of varying biomass moisture content on the volatile flame length and volatile breakthrough during co-firing of biomass with coal, for low co-firing ratios.

D.2 Experimental Methods

D.2.1 Reactor

All experiments were performed in a swirl-stabilized combustor, fully described in [215] and shown in Fig. 1. The combustion section of the furnace is 0.17 m ID and 2.44 m in length, followed by an additional section with 0.36 m ID and 1.2 m length to ensure burnout. The fuels were carried by the primary oxidizer (PO) and entered the system through the burner nozzle. Swirl in the secondary oxidizer (SO) flow was generated and controlled by axial and tangential flows to assist flame stability. The coal and sawdust were metered using volumetric screw feeders (K-Tron and Schenk AccuRate, respectively) and fed into the PO with the assistance of a shaker and an eductor. The two fuels were combined prior to entering the eductor. The shaker acted to ensure a steady feed and prevent clogging. All experiments were performed at a nominal thermal input of 18 kW.

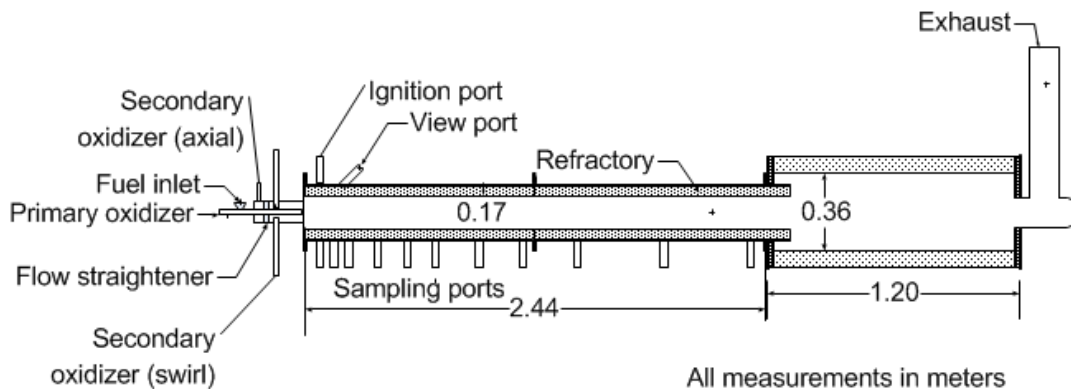


Figure D-1. Schematic of the reactor

The experiments were conducted with pulverized Powder River Basin (PRB) coal that had an as-fired moisture content of 17 wt.%. Co-firing experiments were performed with 80 wt.% PRB coal

/ 20 wt.% sawdust, and the sawdust had an as-fired moisture content of 10, 20, or 30 wt.%. The co-firing ratio of 20 wt.% is on the high side, but not uncommon in pilot and industrial scale systems [217, 218]. To obtain the three biomass samples, oak wood sawdust was collected from a local sawmill in Missouri at a moisture content of 45 wt.%. The samples were sieved with a No. 18 mesh sieve (1.0 mm nominal particle diameter) to remove branches, wood chips, and large particles. The samples were then air-dried to the desired moisture content. A high resolution thermogravimetric analyzer (TGA) (TA Instruments Inc.) was used to determine moisture content for the biomass by heating the sample from room temperature up to 105 °C and then holding for 30 minutes under nitrogen gas flow. The same method was used to reconfirm the moisture just prior to each experiment.

Co-firing was conducted on a total mass (i.e. wet) basis and the thermal input was maintained the same for all conditions. Based on volatile content for the fuels and the mass flow rates at each operating condition, there is less than a 5 wt.% difference in total volatile content between the extreme cases of 10% moisture and 30% moisture co-firing, and this difference was considered to be insignificant.

Proximate and ultimate analyses were performed independently by Standard Labs, which used ASTM methods to obtain results. Sieve analysis for particle size distribution was done with a DuraTap 168 Sieve Shaker (ATM Corporation).

D.2.2 Gas Sampling

Concentrations of CO, CO₂, and O₂ were obtained from a Portable Gas Analyzer (PGA-250, Horiba Inc.). Gas sampling was performed at seven sampling ports located along the length of the combustion chamber as seen in Fig. 1. The gas sampling probe consisted of two concentric tubes

with the inner tube (ID 4.5 mm) as the sample tube and the outer tube (ID 10.2 mm) as the dilution tube. Dilution gas flowed in the annulus between the two tubes before meeting the sampled gas. The dilution gas had the dual role of diluting and quenching the gas sample to prevent further reaction within the probe, and to keep the probe cool. The gas exiting the probe was dried in a condensation trap and filtered prior to analysis.

D.2.3 Volatile Flame Length—Measurement Technique

Concentrations of CO, CO₂, and O₂ are strong indicators of flame structure in diffusion flames [213]. Moving along the centerline through the fuel-rich volatile flame zone, both CO concentration and volatile reaction rate initially increase, and then decrease as the conditions become fuel-lean near the end of the volatile flame. Thus CO concentration can be used to determine the volatile flame length. In this study, we use the procedure developed in [216, 219] for flame length measurement. The CO ratio is given by

$$CO \text{ Ratio} = \frac{[CO]}{[CO] + [CO_2]} \times 100 \quad (D-1)$$

There are several advantages of using the CO ratio over the CO concentration to identify the end of the flame. The CO ratio is a more sensitive indicator of the end of the volatile flame because it incorporates CO₂, which will increase as CO is consumed and converted to CO₂ towards the end of the flame. In addition, the parameter is dimensionless and independent of the amount of dilution used in the probe. The above definition for CO ratio is similar to that of combustion efficiency when evaluated for the flue gas [220]. However, the term combustion efficiency is not appropriate in the context of local quantities, and to prevent confusion, the term CO ratio will be used instead.

Centerline gas composition was sampled along the combustor axis, and the discrete data of CO ratio was curve fit to obtain a smooth curve. The slope of the CO ratio with axial distance within

the volatile flame is driven by volatile oxidation in the fuel-rich environment, while the slope outside of the volatile flame is associated with char oxidation. Based on previous work, the end of the volatile flame was defined as the location along the profile where the slope of the CO ratio is $33 \pm 1\%$ of the maximum negative slope [216].

Figure 2 illustrates the flame structure and the end of the volatile flame. Figure 2a shows the case where devolatilization is complete before the end of the volatile flame. Figure 2b shows a case where the end of the volatile flame occurs prior to the end of volatile release and in this case, since complete devolatilization has not occurred prior to the end of volatile flame, volatile breakthrough occurs. In this case, the volatile flame is shorter than the case with no volatile breakthrough (Fig. 2a), due to a reduced amount of volatiles (fuel) in the near burner region. Note that the reduced flame length exacerbates the volatile breakthrough by giving less time for devolatilization.

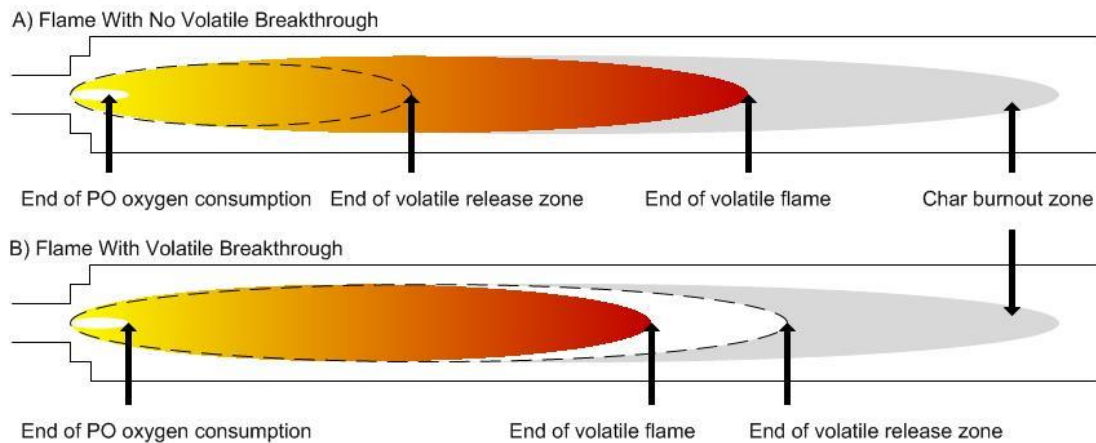


Figure D-2. Visual representation of the volatile flame: a) No volatile breakthrough: the end of the volatile flame is downstream of the end of volatile release. b) Volatile breakthrough: the end of the volatile flame is upstream of the end of the volatile release zone. Reproduced from [191].

D.2.4 Particle Sampling

Once the volatile flame length was determined, particles were sampled isokinetically from the sampling port closest to the end of the volatile flame with a stainless steel sampling probe (shown in Fig. 3). The probe was constructed with an outer tube of 14.8 mm ID and an inner tube of 10.2 mm ID. Nitrogen dilution gas, cooled in a liquid nitrogen chiller, was supplied to the probe and flowed through the annulus of the two concentric tubes and then through an orifice plate to force mixing with the gas sample to dilute and quench the flue gas to temperatures below 180 °C, to ensure no further release of volatiles. This 180 °C threshold for release of volatiles was determined using the Modulated TGA (MTGA) method with high resolution. A blower (Fuji Electric, Inc.) was used to control the sampling flow rate. Glass microfiber thimbles (GE Healthcare Life Sciences, Whatman) were used as particle collection filters.

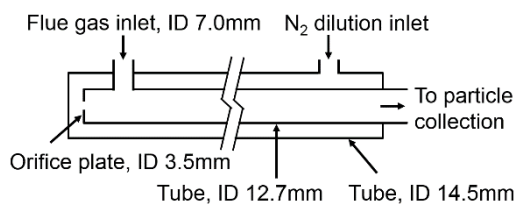


Figure D-3. Isokinetic particle sampling probe schematic.

The collected samples were ground and analyzed for moisture and volatile content. To determine volatile content, a method of proximate analysis for coal and coke was used (TA-129, TA Instruments Inc.). The moisture was removed from the sample by the same method described previously. The sample was then heated to 900 °C and held at isothermal conditions for 15 minutes under nitrogen to remove volatile carbon.

D.3 Analytical Methods

In the experimental system, as with industrial systems, solid fuel enters the furnace at high velocity with the primary gas. The secondary gas is supplied, usually with a swirl component, to create intense mixing and flame stabilization. The smaller particles interact with the fluid and are entrained in the turbulent eddies generated by the swirl. The heat and mass transfer characteristics of these particles are described by Annamalai et al. [221, 222]. Typically, biomass particles are much larger than coal particles. And the larger of these biomass particles have Stokes numbers sufficiently high that the particles have enough momentum to shoot straight through. These are the particles of interest when dealing with volatile breakthrough due to their limited residence time in the volatile flame region.

During devolatilization, there are several time scales that need to be considered: – 1) heat transfer through the gas, 2) gas to particle heat transfer, 3) heat penetration in the solid particle, 4) moisture vaporization, and 5) pyrolysis. These time scales, when compared with the particle residence time in the volatile flame, can provide insights into the amount of volatile breakthrough under different conditions and the controlling parameters. In this paper, only the particle heating and moisture vaporization time scales will be discussed. A more detailed discussion of a characteristic-time based approach to determine volatile breakthrough, and to determine co-firing parameters to minimize breakthrough, will be presented in a future publication.

There are two different time scales associated with particle heating – firstly, the heat transfer from the surrounding gas, and secondly, the thermal wave penetration into the particle. Typically, solid fuel particle heating is assumed to proceed in a layered type of process as the heat diffuses to the center of the particle and the mass of the particle begins to increase in temperature. In this analysis,

for simplicity, a lumped capacitance approach is assumed for the particles. If the lumped capacitance assumption is invalid for some particles due to their large size, the characteristic time will increase. The time scale for heat diffusion to the center of the particle is given by [221]

$$t_d = d_p^2/4\alpha_p \quad (\text{D-2})$$

where d_p is the particle diameter and α_p is the thermal diffusivity of the particle. The time required to heat the particle mass is derived from the heat transfer equation and is given by [221]

$$t_h = \frac{\rho_p d_p^2 c_p}{6\lambda_p Nu} \quad (\text{D-3})$$

where ρ_p is the particle density, c_p is the particle specific heat capacity, λ_p is the particle thermal conductivity, and Nu is the Nusselt number assuming heat transfer by conduction. The sum of these two characteristic times gives us the characteristic time associated with particle heating.

In the meantime, moisture will be released from the particles, and the time scale associated with that release is calculated based on a heat balance between moisture vaporization and heat transfer to the particle. The surrounding gas was assumed to be at 1500 K [216] and the particle to be at 373 K. The moisture time is given by

$$t_m = \frac{f_m \rho_p d_p^2 L_v}{6Nu\lambda_g(T_g - T_p)} \quad (\text{D-4})$$

where, f_m is the moisture fraction in the particle and T_g and T_p are the gas and particle temperatures respectively. For this simplified analysis, the effect of particle moisture content on surrounding gas temperature is neglected.

D.4 Results and Discussion

D.4.1 Coal and biomass properties

The results from proximate and heating value analysis are shown in Table 1. The sieve analysis results, along with the mass mean diameters calculated by fitting the results to a Rosin-Rammler distribution, are shown in Fig. 4. There are significant differences between the coal and sawdust. The coal has a larger heating value than sawdust and the sawdust has almost twice the volatile content of the coal. Importantly, the mass mean diameter of the biomass is an order of magnitude larger than coal, with more than 70% of the biomass weight contained in particles that are larger than the largest coal particles, and this is true for all three cases of biomass.

When sawdust particles absorb moisture, swelling can result. For hardwoods, swelling due to moisture absorption has limited impact on volume beyond 30% moisture [223]. When comparing oakwood having 30% moisture to dry oakwood, the change in size is less than 5% [223-225]. Thus, it is believed that particle aggregation (clumping) is the primary cause for the measured differences in particle size distributions for the different moisture cases.

Table D-1. Coal and biomass properties.

	PRB Coal	Sawdust
HHV MJ/kg (DAF)	29.7	20.2
<i>Proximate Analysis</i>	<i>wt.% (dry)</i>	<i>wt.% (dry)</i>
Ash	7.59	1.30
Volatile Matter	45.40	80.24
Fixed Carbon	47.01	18.46

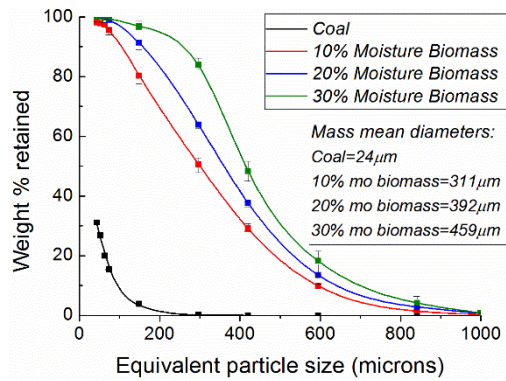


Figure D-4. Fuel particle size distributions using sieves, and the mass-mean diameters calculated using Rosin-Rammler curve fit.

D.4.2 Volatile Flame Length and Breakthrough

Figure 5 shows the centerline CO ratio profile along the length of the reactor as measured experimentally. The measurements were curve fit to obtain a smooth profile to estimate the volatile flame length. The curve fit applied is given by,

$$CO \text{ Ratio} = \exp(a + bx + cx^2) \quad (D-5)$$

Here, x is the distance downstream from the injection nozzle. This equation best fits the CO ratio profile at both small and large x values.

Experimental results show a significant impact of moisture content on both the CO ratio profile and the flame length. The coal-only volatile flame, at 1.02 m in length, is longer than all the co-firing volatile flames. The flame length decreases 0.17 m for the 10% moisture co-firing flame, 0.31 m for the 20% case, and 0.36 m for the 30% case (see arrows in Fig. 5). The 20% and 30% moisture biomass cases are so close in flame length, that they are considered to be the same within experimental uncertainty.

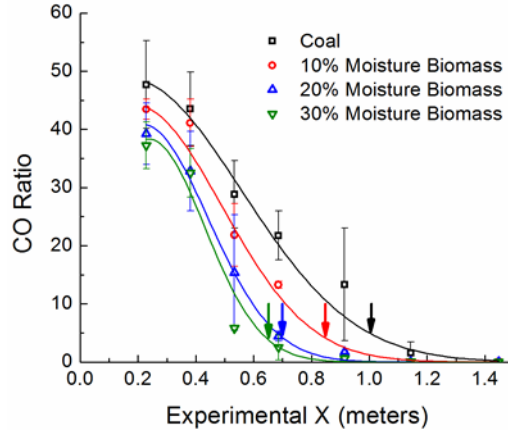


Figure D-5. Experimental CO ratio profiles (symbols) and curve fit (lines). Error bars show the maximum and minimum values for that port. The arrows denote the end of flame.

Though sawdust has twice the volatile content as coal, which suggests that replacing coal with sawdust should increase the volatile flame length, co-firing leads to shorter volatile flames. There are multiple parameters, apart from fuel volatile content, that control flame length. The sawdust particles, on average, are larger than the coal particles. Larger particles have larger momentum and longer heating times, both of which lead to volatile release farther from the near-burner zone, reducing the amount of volatiles in the near-burner zone. This reduced near-burner volatile release leads to a shorter volatile flame, where the length is primarily controlled by the coal and smaller biomass particles, counteracting the larger fuel-volatile content [216]. As the amount of moisture in the biomass increases, the heating time further increases, which delays devolatilization. With increasing moisture content, the particle size also increases (Fig. 4), which leads to slower heating rates, increased devolatilization delay and shorter flames.

For the coal-only case, the particles sampled at the end of volatile flame showed negligible volatile matter because the coal particles are small and their residence time in the flame is long because they are retained in the swirl-induced recirculation zones [215]. In co-firing, the biomass particles, due to their larger size and resulting high Stokes number, have volatiles breaking through the

flame. The 10% moisture biomass case had some volatile matter after the end of volatile flame, but it was lower than the other two biomass cases, as shown in Fig. 6. Since, for the 20% and 30% moisture biomass cases, as discussed above, the flame length was nearly the same, particle collection for both the cases was performed from the same port on the furnace. The port itself was immediately downstream of the 30% co-firing end of flame (as required for volatile breakthrough measurement) and just upstream of the 20% co-firing end of flame. This was done since the next possible location for particle sampling for the 20% moisture case (slightly longer flame length compared to 30% moisture case) would otherwise be 0.2 m downstream of the end of flame. Thus the particles for the 20% moisture case were collected prior to passing through the flame, and the particles for the 30% moisture case were collected immediately after they exit the flame. This difference in the relative location of particle sampling – inside vs. outside the volatile flame envelope, predictably led to a disparity in the amount of volatile breakthrough with respect to expectation of increasing volatile breakthrough with increasing moisture content. Neglecting the 20% case particle sampling results due to inability to sample at the relevant location (immediately downstream of the volatile flame), the results of the coal, 10% moisture biomass co-firing, and the 30% moisture biomass co-firing results confirm the expected trend: volatile breakthrough increases with increasing moisture content.

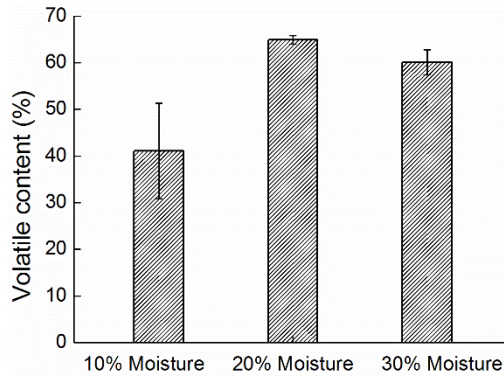


Figure D-6. Volatile content measured in particle samples taken immediately downstream of the volatile flame during the co-firing cases. Note: For the 20% moisture case, particles were sampled before the end of volatile flame.

D.4.3 Analytical Results

The experimental results clearly show that the volatile flame is shortened and volatile breakthrough increased as we move from low moisture biomass to high moisture biomass. As moisture increases, particle clumping increases and the mean particle size increases as well. Thus, the increase in breakthrough with increase in biomass moisture can be a result of both increased particle heating time due to the larger particle size, as well as increased time for moisture vaporization. From the above experiments, it is not possible to ascertain the relative influence of the two. A characteristic-time analysis, on the other hand, will clarify this by comparing the characteristic times of the two parameters: heating time due to the increase in particle size and time for moisture vaporization. Figure 7 shows the breakdown of the impact of the different characteristic times. Increasing moisture content increases the devolatilization delay and hence could lead to breakthrough, as expected and also shown by experiments. It can also be seen that on an absolute basis, the time scale for particle heating is an order of magnitude larger than that for moisture vaporization. Thus, for the cases considered here, the impact of moisture is primarily seen through its effect on particle size. On the other hand, the ratio of particle heating time to the moisture vaporization time

decreases with increasing moisture, thus making the direct impact of moisture vaporization time more significant at higher moisture levels. Furthermore, as the biomass moisture content increases, the volatile flame length is reduced and the particle residence time in the volatile flame envelope is reduced. Thus, as the biomass moisture increases, the reduced particle residence time may lead to situations wherein the devolatilization delay is significant enough that virtually no volatiles are released from the biomass in the volatile flame zone. Therefore, the flame length reduction or increase in volatile breakthrough would asymptote, as was seen experimentally in Fig. 5.

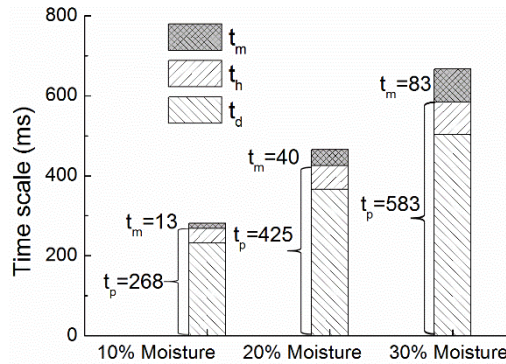


Figure D-7. Characteristic times for biomass particle heating (t_p), divided into heat diffusion to the center (t_d) and heating of particle mass (t_h), and moisture vaporization (t_m).

This simplified analysis should be used with caution because when the moisture content is high or the particle size increases significantly, other secondary effects may be significant. For example, as particle size increases, the lumped capacitance model will not hold true, and hence the characteristic time will increase more than predicted by this model, while as the moisture content increases, the surrounding gas temperature might decrease prompting an increase in vaporization time.

D.5 Conclusions

This study analyzed the effects of moisture content of biomass in a co-firing system with oakwood sawdust and PRB coal. Experiments were performed at 18 kW_{th} in a swirl-stabilized furnace. Operating conditions included coal-only, and 20 wt.% co-firing biomass with coal. The biomass moisture contents were varied from 10 to 30 wt.% moisture. Center line gas sampling was conducted to determine the CO ratio, which was used to characterize the volatile flame length. The CO ratio profile was curve fit to closely match the rapid increase in the CO ratio along the reactor in the devolatilization region, followed by a rapid decrease, due to conversion of CO to CO₂ further downstream in the combustor. The end of the volatile flame was taken to be the location where the slope of the CO ratio curve fit was 33% of the maximum negative slope. At low co-firing ratios, increasing the biomass moisture content reduces the volatile flame length and enhances volatile breakthrough. Particle sampling at the end of the volatile flame confirmed the hypothesis that, with increasing biomass moisture, there is an increase in the volatile content of the particles downstream of the volatile flame (i.e., there is greater volatile breakthrough). Sieve analysis showed a difference in the size distribution of the biomass with changing moisture content. Comparing this difference to the potential swelling of oakwood with moisture showed that swelling is negligible, while clumping is likely the main cause of increased size. Previous studies done by the same group have shown that particle size negatively influences flame length.

To isolate the causes of devolatilization delay and compare their relative importance, a characteristic-time scale analysis was done, where the characteristic time for particle heating (including heat transfer to the particle and thermal wave penetration) was compared to the characteristic time for moisture evaporation. The analysis showed an order of magnitude difference between the devolatilization time delay caused by the difference in particle size (mass mean

diameter) and the time delay caused by moisture vaporization. Particle size differences due to clumping had a much higher impact on devolatilization delay than purely moisture vaporization. Furthermore, when the moisture content was high (20%), further increases in moisture content led to only a minor reduction in flame length or increase in volatile breakthrough, a result that indicates these biomass particles are not releasing volatiles in the volatile flame zone.

D.6 Acknowledgements

Funding was provided by the Consortium for Clean Coal Utilization at Washington University in St. Louis.

Curriculum Vitae

Akshay Gopan

One Brookings Drive, Campus Box #1180, St. Louis, MO 63130, USA, akshay.gopan@wustl.edu

SUMMARY

Research focus on process development, and equipment design for multi-phase, turbulent reacting flows for industrial and utility application. Experience in computational fluid dynamic simulations, and experimental studies—including design, construction and commissioning of lab and pilot scale combustion reactors, as well as process design and techno-economic analysis.

EDUCATION

		Year
Ph.D.	Energy, Env. & Chemical Eng., Washington Univ. in St. Louis, USA	2017
M.S.	Energy, Env. & Chemical Eng., Washington Univ. in St. Louis, USA	2015
B. Tech.	Chemical Eng., Indian Institute of Technology Bombay (IIT-B), India	2011

HIGHLIGHTS

- CFD design of reactors for multi-phase, turbulent combustion with a focus on heat transfer control.
- Experimental experience in turbulent combustion reactors from lab to pilot scale
- Process development of a novel high efficiency, low-cost power plant—using Aspen Plus.
- Industrial collaborations for process and equipment design, and cost analysis.
- International research experience—US, Germany, Denmark, and India.

RESEARCH EXPERIENCE

Ph.D., WASHINGTON UNIVERSITY IN ST. LOUIS, MO, USA 2011–2017

Development of staged, pressurized oxy-combustion for carbon capture *Advisor: Prof. R.L. Axelbaum*

- Development and techno-economic analysis of the staged, pressurized oxy-combustion (SPOC) process for high-efficiency power generation with carbon capture—net plant efficiency increased by more than 25%.
- Design of burner and boiler for low-recycle, SPOC process for flexible operation—control of heat transfer.
- Burner testing and validation with atmospheric pressure experiments at 20 kW_{th} to 1 MW_{th}.
- Control of radiative heat transfer and soot in high temperature, turbulent gas flames—experiments, analytical modeling and numerical simulations—in single and multi-port burner furnaces/combustors.

Other Relevant Research at Washington University in St. Louis

- Design, construction and commissioning of multiple 10–100 kW_{th} combustion test reactors for SPOC.
- Deposition rate and temperature of aerosols from non-isothermal, turbulent flows.
- Design of a two-stage flat-flame burner to better mimic the true temperature-time-gas composition history of reacting solid fuel particles in full scale furnaces/boilers to study early stage combustion processes.
- Experimental studies on the effect of fuel properties on the volatile flame during co-firing biomass & coal.
- Coal water slurry preparation, stabilization, and combustion experiments.

WORK EXPERIENCE

SCIENTIST, INST. OF COMB. & POWER PLANT TECH. (IFK), UNIV. OF STUTTGART Spring 2014

- Experimental study on slagging and fouling in solid-fuel combustion in high O₂ environments at 20 kW_{th}.
- Model development for mineral transformation during solid-fuel combustion.

PROCESS EXECUTION (INTERN.), LURGI INC. Summer 2010

- Involved in development of advanced engineering package for gas cleanup in a liquefied natural gas plant.
- Heat & mass balance calculations and equipment design, including heat exchangers, pumps, columns, etc.

RESEARCH INTERN., DEPT. OF CHEMISTRY, UNIVERSITY OF COPENHAGEN Summer 2009

- Synthesis and spectral characterization of a chiral mercury coordination compound.
- Gained experience with many spectroscopic techniques, e.g., UV-Vis, circular dichroism, FTIR, and NMR

TECHNICAL SKILLS

- Softwares Ansys Fluent, Aspen Plus, Matlab, Maple, FactSage, LabView
- Languages C, Python
- Scientific Instruments
 - Particle Sampling* Scanning Mobility Particle Sizer (SMPS); Optical Particle Sizer (OPS); Electric Low Pressure Impactor (ELPI).
 - Characterization* Thermogravimetric Analyzer (TGA); Scanning Electron Microscopy with Energy Dispersive X-ray (SEM/EDX); X-ray Diffractometer (XRD); Flame emission spectrometry; UV-Vis and CD spectrometry; FTIR; NMR.
 - Gas analysis* Continuous emissions monitoring systems (CEMS).

PATENTS

1. Burner or boiler/furnace for pressurized oxy-combustion boiler or furnace. Filed 2017, U.S. Patent Application No.: 62/464,159.
2. Method and apparatus for capturing carbon dioxide during combustion of carbon containing fuel. Filed 2013, U.S. Patent Application No.: 61/830, 428.

SELECTED PEER-REVIEWED PUBLICATIONS

1. **Gopan, A.**, et al. Effects of inert placement (Z_{st}) on soot and radiative heat flux in turbulent diffusion flames. *Energy & Fuels* (2017).
2. **Gopan, A.**, et al. Effect of operating pressure and fuel moisture on net plant efficiency of a staged, pressurized oxy-combustion power plant. *Int'l J. of Greenhouse Gas Control* (2015).
3. **Gopan, A.**, et al. Process design & performance analysis of a staged, pressurized oxy-combustion (SPOC) power plant for carbon capture. *Applied Energy* (2014).
4. Fei, Y., **Gopan, A.**, Axelbaum, R L. Characterization of coal water slurry prepared for PRB coal. *Journal of Fuel Chemistry and Technology* (2014).
5. Fei, X., Yang, Z., Adeosun, A., **Gopan, A.**, Kumfer, BM., Axelbaum, R L. Pressurized oxy-combustion with low flue gas recycle: Computational fluid dynamic simulations of radiant boilers. *Fuel* (2016).

6. **Gopan, A.**, et al. Staged, pressurized oxy-combustion boiler with low flue gas recycle. Part I: Burner design and scaling. *Fuel*. In review.
7. **Gopan, A.**, et al. Staged, pressurized oxy-combustion boiler with low flue gas recycle. Part II: Operational flexibility. *Fuel*. In review.
8. Adeosun, A., Huang, Q., **Gopan, A.**, et al. Early-stage coal combustion processes in a two-stage Hencken burner—Design and characterization. *Combustion & Flame*. In review.

In Preparation

9. **Gopan, A.**, et al. Understanding soot inception in tri-axial burners—analytical and computational analyses. *In preparation*.
10. **Gopan, A.**, et al. Effects of pressure and combustion environment on the ultra-fine mineral matter transformation in solid-fuel combustion. *In preparation*.
11. **Gopan, A.**, et al. A time-scales analysis on the effect of fuel properties on the volatile flame length during co-firing two solid fuels. *In preparation*.
12. Yang, Z., **Gopan, A.**, Axelbaum, R.L. Predicting particle deposition from non-isothermal, turbulent parallel flows. *In preparation*.

TECHNICAL CONFERENCES

1. **Gopan, A.**, et al. Burner and boiler design concepts for a low-recycle, Staged, Pressurized Oxy-Combustion power plant. *The 42nd Int'l Technical Conference on Clean Energy*. 2017. Clearwater, FL.
2. Yang, Z., **Gopan, A.**, Axelbaum, R.L. Predicting ash deposition from non-isothermal, turbulent parallel flows: Application to Staged, Pressurized Oxy-Combustion. *The 42nd Int'l Technical Conference on Clean Energy*. 2017. Clearwater, FL
3. Yang, Z., **Gopan, A.**, et al. Design and commissioning of Staged, Pressurized Oxy-Combustion system. *The 42nd Int'l Technical Conference on Clean Energy*. 2017. Clearwater, FL.
4. Wang, X., Adeosun, A. Yablonsky, G., Yang, Z., **Gopan, A.**, et al. The synergistic promotion of SO₃ and NO₂ formation in the post-flame region of pressurized oxy-combustion. *The 42nd Int'l Technical Conference on Clean Energy*. 2017. Clearwater, FL.
5. **Gopan, A.**, et al. Effects of Stoichiometric Mixture Fraction (Zst) on Soot and Radiative Heat Flux in a Turbulent Diffusion Flame. *10th U.S. National Combustion Meeting*. 2017. College Park, MD.
6. **Gopan, A.**, et al. Scaling and burner design concepts of a staged, pressurized, oxy-combustion boiler. *10th U.S. National Combustion Meeting*. 2017. College Park, MD.
7. Yang, Z., **Gopan, A.**, Axelbaum, R.L. Predicting ash deposition from non-isothermal, turbulent parallel flows. *10th U.S. National Combustion Meeting*. 2017. College Park, MD.
8. Adeosun, A., Huang, Q., Li, T., Wang, X., **Gopan, A.**, et al. Ignition of a dispersed coal particle stream and measurement of ultra-fine particle size distributions. *10th U.S. National Combustion Meeting*. 2017. College Park, MD.
9. **Gopan, A.**, et al. Development of staged, pressurized oxy-combustion. *5th IEAGHG Oxyfuel Combustion Research Network Meeting*. 2015. Wuhan, China.
10. **Gopan, A.**, et al. Fuel-staged, oxy-combustion: reducing recycle to near zero. *9th US Nat'l Combustion Meeting*. 2015. Cincinnati, OH.
11. Adeosun, A., Xia, F., Yang, Z., **Gopan, A.**, et al. Design & numerical study of staged, pressurized oxy-combustion with near-zero flue gas recirculation. *9th US Nat'l Combustion Meeting*. 2015. Cincinnati, OH.

12. **Gopan, A.**, et al. Cost of electricity of a fuel-staged, pressurized oxy-combustion power plant. *AICHE Annual Meeting*. 2014. Atlanta, GA.
13. Pollard, MM., Holtmeyer, ML., **Gopan, A.**, et al. Effects of biomass particle size and moisture content on flame length during co-firing with coal. *4th IEA CCC Workshop on Co-firing Biomass with Coal*. 2014. PA.
14. **Gopan, A.**, et al. Cost and performance of fuel-staged, pressurized oxy-combustion power plant. *Int'l Conference on Greenhouse Gas Control Technologies (GHGT-12)*. 2014. Austin, TX.
15. Adeosun, A., **Gopan, A.**, et al. An experimental investigation of heat transfer behavior in oxygen-enriched coal combustion. *Int'l Pittsburgh Coal Conference*. 2014. Pittsburgh, PA.
16. **Gopan, A.**, et al. Process design and performance analysis of a staged, pressurized, oxy-combustion power plant. *Int'l Pittsburgh Coal Conference*. 2014. Pittsburgh, PA.
17. **Gopan, A.**, et al. Techno-economic study of fuel-staged, pressurized oxy-combustion power plant. *The 39th Int'l Technical Conference on Clean Coal & Fuel Systems*. 2014. Clearwater, FL.
18. Kumfer, B, Dhungel, B, **Gopan, A.**, et al., A Staged, Pressurized Oxy-Combustion System for Carbon Capture. *3rd Oxyfuel Combustion Conference*. 2013, IEA: Leon, Spain.
19. **Gopan, A.**, et al. Performance analysis of a staged, pressurized oxy-combustion power plant with minimal flue gas recycle. *AICHE Annual Meeting*. 2013. San Francisco, CA

LINKS TO ONLINE PROFILES

- Google scholar profile: https://scholar.google.com/citations?user=aT9_vJgAAAAJ&hl=en
- LinkedIn profile: <https://www.linkedin.com/in/akshaygopan>